Performance Analysis of an Annular Diffuser Under the Influence of a Gas Turbine Stage Exit Flow

By

Rafael Rodriguez Blanco

2013

Submitted to the graduate degree program in Aerospace Engineering
and the Graduate Faculty of the University of Kansas in partial fulfillment of the
requirements of the degree of Master of Science

____

Chairperson Prof. Saeed Farokhi

____

Prof. Ray Taghavi

____

Prof. Zhongquan Charlie Zheng

Date Defended: November 6th 2013

The Thesis Committee for Rafael Rodriguez Blanco
certifies that this is the approved version of the following thesis:

Performance Analysis of an Annular Diffuser Under the Influence of a Gas Turbine Stage Exit Flow

____
Chairperson Prof. Saeed Farokhi

Date approved: November 6th 2013

ABSTRACT

In this investigation the performance of a gas turbine exhaust diffuser subject to the outlet flow conditions of a turbine stage is evaluated. Towards that goal, a fully three-dimensional computational analysis has been performed where several turbine stage-exhaust diffuser configurations have been studied: a turbine stage with a shrouded rotor coupled to a diffuser with increasing divergence angle in the diffuser, and a turbine stage with an unshrouded rotor was also considered for the exhaust diffuser performance analysis. The large load of this investigation was evaluated using a steady state numerical analysis utilizing the "mixing plane" algorithm between the rotating rotor and stationary stator and diffuser rows. Finally, an unsteady analysis is performed on a turbine stage with an unsrhouded rotor coupled to an annular exhaust diffuser with an outer wall opening angle of 18°. It has been found that the over the tip leakage flow in the unshrouded rotor emerges as a swirling wall jet at the upper wall of the diffuser. When using the turbine with the shrouded rotor no wall jet was observed, making the flow at the entrance to the diffuser "quasi-uniform". The maximum opening angle of the diffuser upper wall achieved before the diffuser stalls was 12° with a static pressure recovery coefficient of Cp = 0.293. When the wall jet was observed, diffuser opening angles of 18° were possible with a static pressure recovery of Cp = 0.365. Consequently the wall jet energizes the diffuser upper wall boundary layer flow, allows for higher static pressure recovery levels and postpones diffuser stall.

By altering the speed of the rotor the effect of the swirl in the turbine exit plane on the performance of the diffuser was explored. In the case where the wall jet was absent the diffuser recovers more pressure when the inlet is swirl-free. In this case the performance of the diffuser is independent on whether the turbine exit flow has co or counter swirl. In the presence of the wall jet, higher static pressure recovery was achieved when the wall jet was in co-swirl and the core flow at a slightly counter-swirl direction. This observation was more pronounced when larger diffuser upper wall opening angles were considered.

In the unsteady analysis it was found that the wall jet axial velocity and swirl intensities pulsate with the relative position of the rotor to the stator. The wall jet is always co-swirling while the core flow is counter-swirling. Moreover, the wall jet does not penetrate the diffuser boundary layer as deeply as was observed in the steady state case and flow separation occurs at the upper endwall corner of the diffuser. Furthermore the performance of the diffuser shows a periodic variation that seems to depend on the relative position of the rotor to the stator. The averaged pressure recovery coefficient is Cp = 0.321 which is 11.0 % less than predicted in the steady state case.

AKNOWLEGMENTS

This thesis is the result of a combined research work at the Department of Aerospace Engineering of the University of Kansas in Lawrence and at the Laboratory for Energy Conversion (LEC) at the Swiss Federal Institute of Technology (ETH) in Zurich. First of all I would like express my gratitude to my advisor, Prof. Saeed Farokhi for his guidance and support, encouragement during the hard times, and important lessons at all times. Thank you a lot for sending me to the ETH in Zurich.

Many thanks also go to Prof. Reza S. Abhari for giving me the opportunity to continue this research work at his laboratory at the ETH, for his guidance and insightful comments, and for allowing me to use LEC's experimental turbine results for validation. In that sense I am also very grateful to Dr. Ndaona Chokani.

I would like to thank the other members of the committee, Profs. Ray Taghavi and Zhongquan Charlie Zheng, for taking the time in reading this research work, for their comments and corrections.

Last but not least I would like to express my gratitude to my family and friends for their support and encouragement throughout all these years.

TABLE OF CONTENTS

LIST OF FIGURES

LIST OF TABLES

NOMENCLATURE

$\dot{m}$	Mass flow rate
ρ	Gas density
v_x, v_r, v_θ	Velocity components: axial, radial, circumferential
α	Absolute angle of the flow with respect to the axial flow direction (positive sign in direction of turbine rotation)
p	Static pressure
p_t	Total pressure
Cp	Static pressure rise coefficient
Cp_t	Total pressure loss coefficient
B	Aerodynamic blockage
δ^*	Boundary layer displacement thickness
Re_	Reynolds number
γ	Ratio of specific heats
μ_T, μ	Turbulent viscosity, viscosity of the fluid
$P_{t,in} / P_{t,out}$	Total pressure ratio in a turbine
φ	Flow coefficient
u_{ref}	Reference velocity. It corresponds to the mid-span circumferential velocity of the rotor blade.
η_{tt}, $\eta_{tt,pol}$	Total to total isentropic and polytropic efficiencies
$c_{p,gas}$	Gas specific heat capacity at constant pressure
Δh, Δh_{is}, Δh_p	Head, isentropic head , polytropic head
μ_0, μ_{is}, μ_{pol}	Work coefficient, isentropic and polytropic work coefficients

1 INTRODUCTION

Even though the gas turbine itself bears the same operational principles whether it is used as aircraft propulsion engine, power generation, and mechanical drive, the purpose of the gas turbine determines its design to maximize the system's efficiency. The shaft power produced by the turbine is utilized to drive electric generators in the power generation industry, industrial compressors in the petrochemical industry or a fan in the aerospace industry. Most of the power produced by the gas turbine engine/power plant supports the drive of the shaft. However, the exhaust gas contains kinetic and thermal power as well. The principles of propulsion require the kinetic power of the exhaust jet to be higher than the kinetic power of the captured stream. The turbine exhaust gases with high temperature could be used in a boiler heat exchanger to generate steam that feeds a steam turbine.

In Figure 1.1, a single shaft industrial gas turbine with its compressor and turbine sections is depicted, and in Figure 1.2 the shaft of the gas turbine is shown along with a detail view of the turbine section where one observes the zigzag rod connection at the blade tip to dampen the vibration.

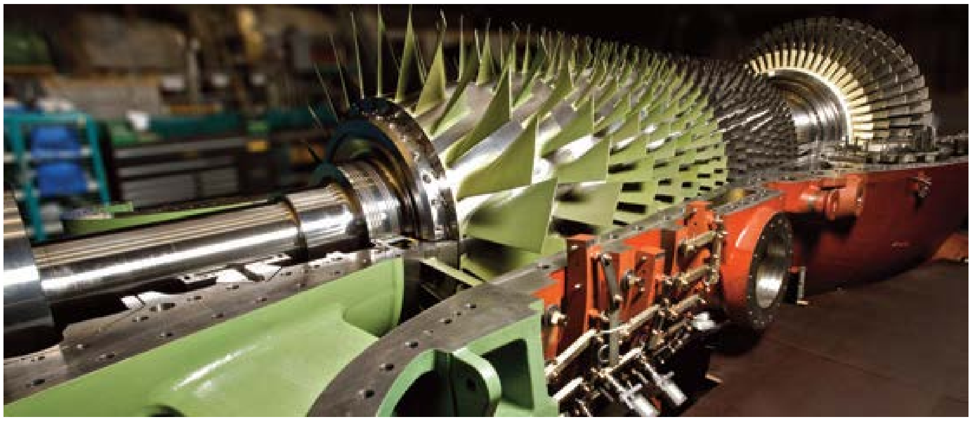

Figure 1.1: Single shaft industrial gas turbine [1]

In industrial gas turbines it is very important to optimize the work of the shaft. It is then crucial that the turbine extracts as much as possible energy from the fluid. The exhaust gases of the gas turbine are dumped to the atmosphere, but it would be beneficial to expand the gas in the turbine below the atmospheric pressure, thus more shaft work is achieved. Recovery of the static pressure from turbine exit sub-atmospheric to atmospheric conditions is accomplished by an exhaust diffuser of annular geometrical shape attached at the exit of the turbine stages. Therefore optimizing the design of the diffuser so that it can recover as much static pressure as possible will enhance the power production capability of the gas turbine.

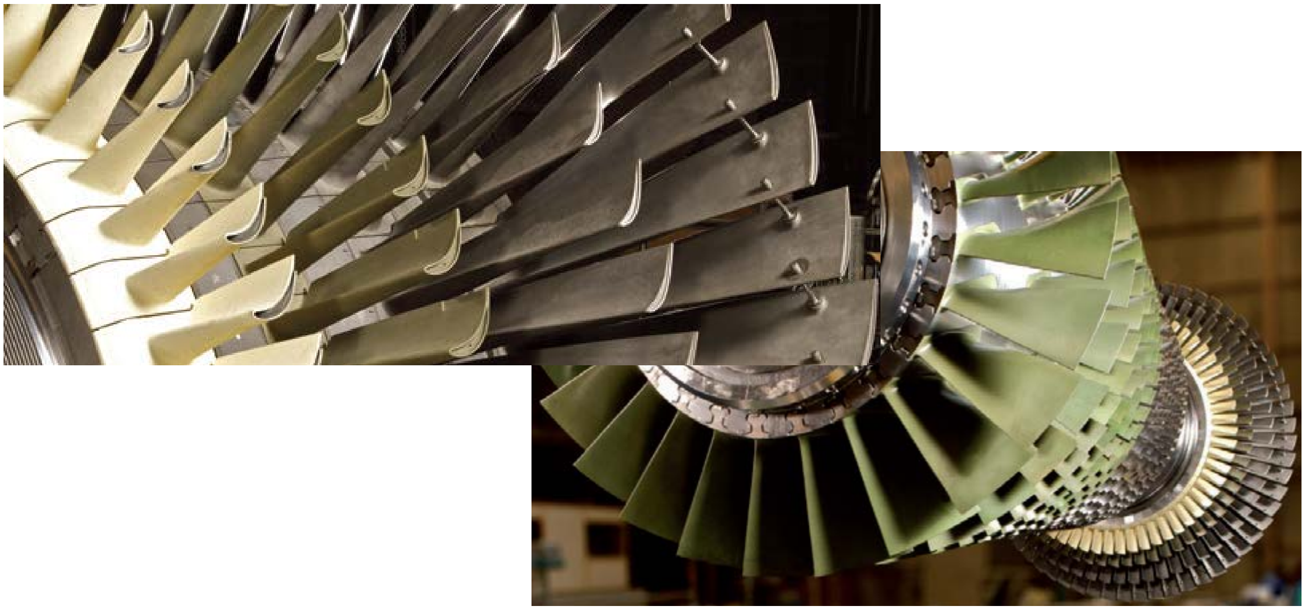

Figure 1.2: Turbine section (left) and shaft with compressor and turbine sections (right) [1]

2 LITERATURE REVIEW

Flow structure in turbomachinery passages is extremely complex. Curved passages, end wall and blade row boundary layers give rise to non-uniform velocity profiles, pressure gradients and temperature gradients. The combination of all these non-uniformities promotes secondary flows and vorticity generation. Clearances between the blades and the end walls generate leakage flows. The relative motion of the rotating parts provides another key ingredient of complexity, namely unsteadiness, which is inherent in any rotating machine. The combination of all these effects decreases the efficiency of the engine. Diminishing the aerothermal losses generated in the passages is possible but other aspect of the system may be compromised, such as rotor-dynamics. It is also common to incorporate ducts in gas turbine engines to cause flow deceleration or acceleration to adjust pressure and flow uniformity.

2.1 Secondary flows in turbine passages

A simple definition of secondary flows could be any flow structure that does not follow the intended (primary) flow direction inside a channel. Very often, it is the end wall boundary layer at the inlet of the passage that is responsible for the secondary flows. One of the earliest pioneers that reported the existence of secondary flows in curved passages is due to Hawthorne [2 & 3]. He found that the deflection of vortex filaments/tubes in a flow with an initial normal vorticity distribution results in a streamwise component of vorticity at the exit of the passage. This phenomenon is caused by the curvature of the passage, i.e., transverse pressure gradient to the flow direction, as shown in Figure 2.1.

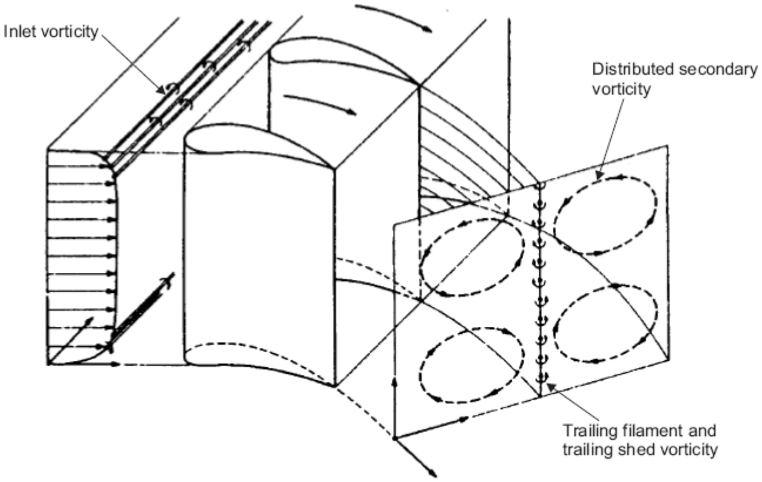

Figure 2.1: Sketch of the vorticity across a turbine blade row [3]

As the flow in the blade passage rotates about its ideal (potential) flow direction, a transverse pressure gradient in the passage is generated to balance the centripetal acceleration of the fluid, according to the following relation:

$$\frac{\partial p}{\partial n} \approx \frac{\rho u^2}{R} \tag{2.1}$$

The static pressure remains practically unchanged if no regions of flow separation are present. Also, since the velocity of the fluid is lower near the end walls, the radius of curvature of the boundary layer streamlines has to be smaller. Therefore the low momentum fluid within the boundary layer develops a component of velocity normal to that of the main stream as seen in Figure 2.2.

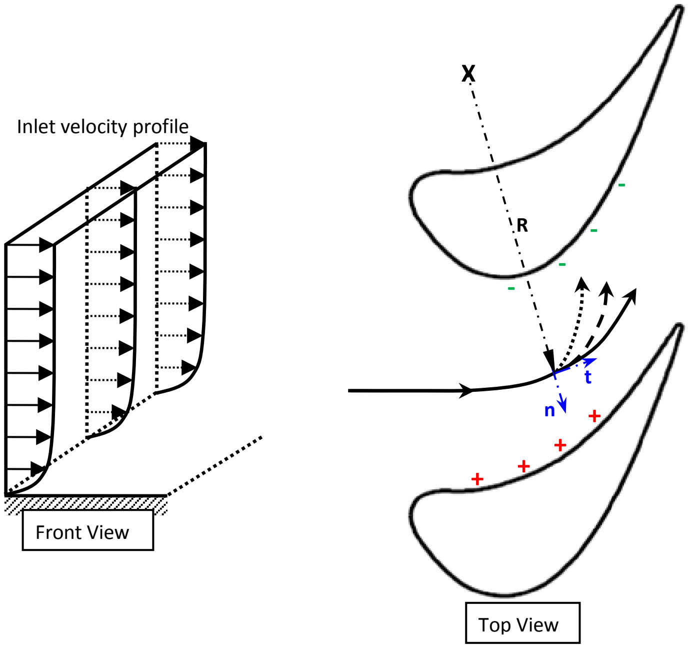

Figure 2.2: Sketch of the cross flow production within a turbine passage

Hence, it is the redistribution of low momentum fluid that migrates from the concave (pressure) side of a duct to the convex surface that is responsible for the generation of secondary flows in a blade (or curved) passage. The process of streamwise vorticity generation is inviscid by nature, i.e., pressure-driven, even though the inlet boundary layer vorticity is stretched in the streamwise direction in the passage. For a particular design of blade profiles, there are secondary flow variances in magnitude and extent, but the prominent features that are typically observed are depicted in Figure 2.3 and Figure 2.4.

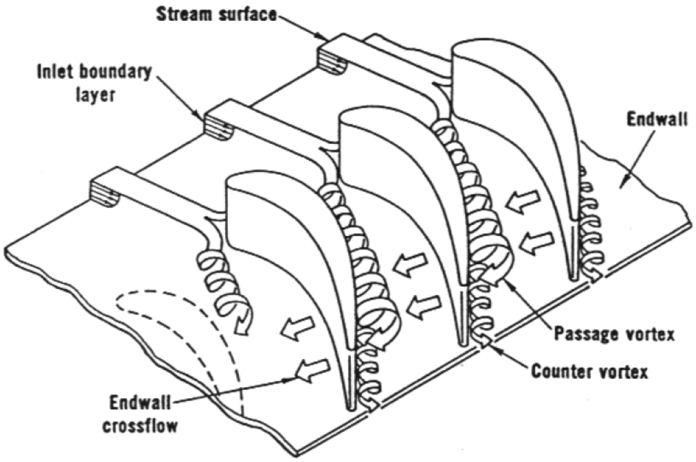

Figure 2.3: Secondary flow model of Langston [4]

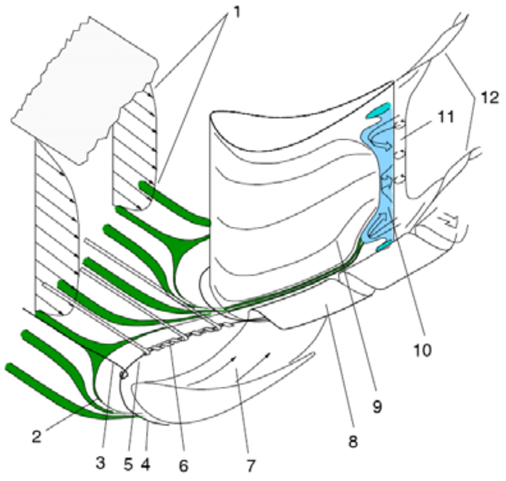

1 – Inlet boundary layer
2 – Separation line of the inlet boundary layer
3 – Horseshoe vortex, inlet flow
4 – Horseshoe vortex (suction side leg)
5 – Horseshoe vortex (pressure side leg)
6 – Rolling up of the inlet boundary layer
7 – Passage cross flow
8 – Passage vortex
9 – Suction side boundary layer shift
10 – Hub-corner stall
11 – Trailing edge flow shedding
12 – Trailing vortices

Figure 2.4: Secondary flow model of Vogt and Zippel [5]

- *Horseshoe vortices*: Due to the presence of the blade, the endwall boundary layer of the incoming flow, which is basically a layer of tangential vorticity, rolls up at the leading edge of the blade and splits into a system of two counter-rotating vortices. These two vortices convect through the passage at each side of the blade, namely the pressure and suction sides.

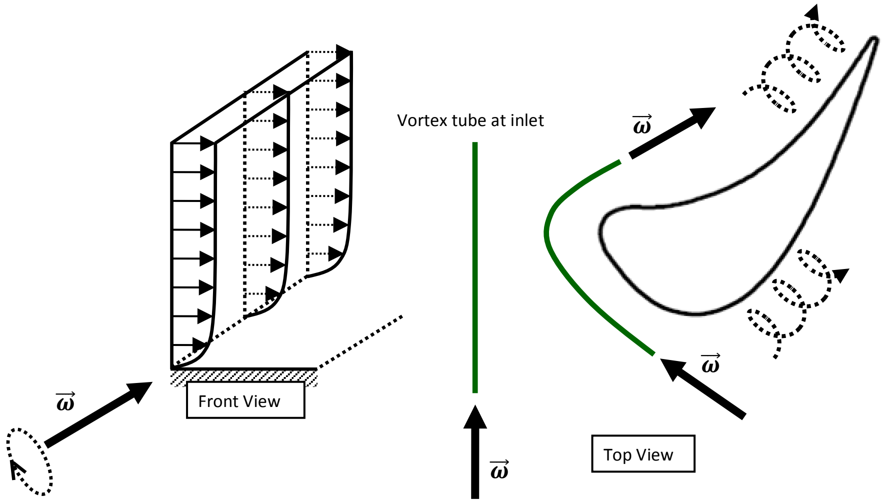

Figure 2.5: Sketch of the formation of a horseshoe vortex around a blade

- *Passage Vortices*: Due to the pressure gradient that exists between the pressure and suction sides of the blade profile within the passage, the low momentum fluid “trapped “ in the endwall boundary layers shifts from the blade pressure side to the blade suction side. This “pressure induced” cross-passage flow rolls up as it approaches the suction side of the blade and forms the passage vortex. Moreover, the passage vortex has the same sense of rotation as the pressure side leg of the horseshoe vortex. As both types of vortices convect in the streamwise direction, they merge and appear as one at the exit of the blade passage.

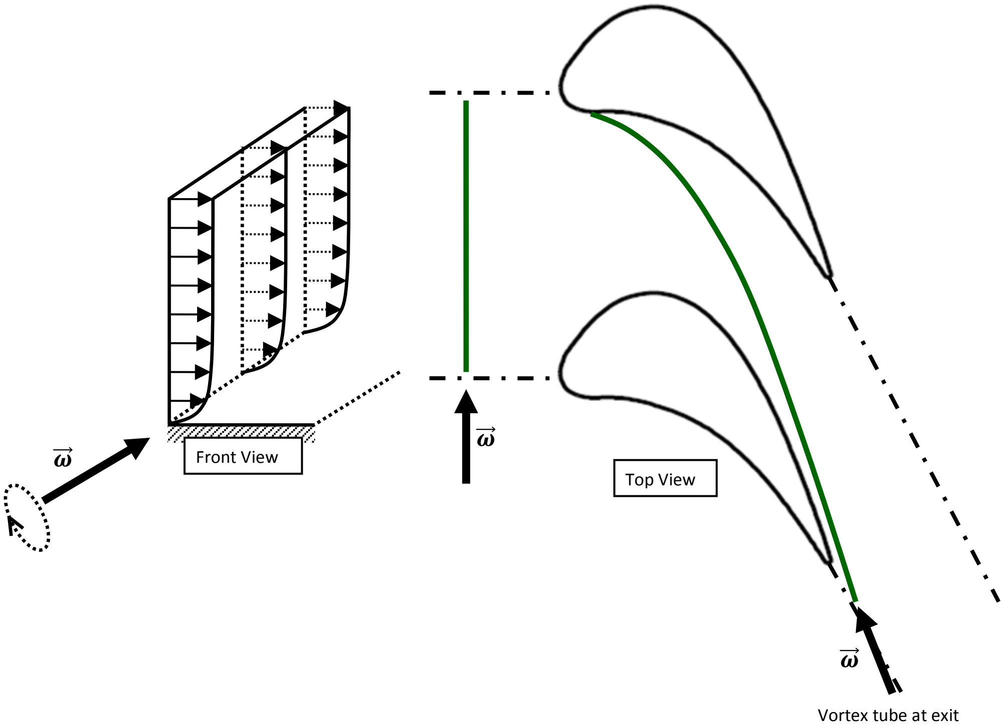

Figure 2.6: Sketch of the generation of vorticity in a turbine passage

- *Corner vortices*: The occurrence of these vortices depends on the strength of the passage vortex, and when present, they are very difficult to capture experimentally in turbomachinery passages as stated by Laksminarayana [6]. As the passage vortex migrates from the pressure to the suction blade side of the passage, fluid is gathered in between the passage vortex front and the corner formed by the suction side of the blade and the end wall. The rotation of this passage vortex induces a circulation of opposite sense to the collected fluid. This gives rise to the corner vortex. An easy way to picture the corner vortex is by referring to the flow structures in a 2D back step case. Depending on the size and strength of the main vortex, a corner vortex will appear or not, as sketched in Figure 2.7.

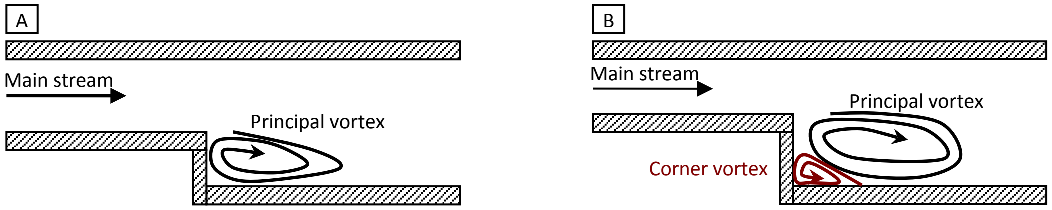

Figure 2.7: Sketch of the occurrence of an induced corner vortex in a 2D back step flow

Blade turning, pitch to chord ratio, aspect ratio and inlet vorticity are such factors that affect the strength and dimension of the secondary flows. The most important fact about secondary flows is that they affect negatively the performance of a turbomachine. Lastly, the strength and nature of secondary losses are different from one machine to another, as in a compressor and in a turbine. In a turbine, the leading edge is blunter, therefore the horseshoe vortices are more pronounced. The flow turning in a turbine is larger so the passage vortices are stronger.

2.2 Turbine rotor over the tip leakage flow

In order to optimize the thermal efficiency of a turbine stage it is important to minimize the aerodynamic losses that occur within it. One of the most important sources of losses is due to over the tip leakage (OTL) flow in rotor blades since it accounts for over one third (> 1/3) of the overall turbine stage losses [7].

The over the tip leakage (OTL) flow has its origins on the static pressure difference that occurs at each side of the rotor airfoil at the tip. In this gap the fluid is not deflected by the blade and hence does not contribute to the work output of the stage. The fluid enters the gap on the pressure side of the rotor blade and continues to the other side where it mixes with the core flow and rolls up into a vortex. An additional vortex due to the endwall boundary layer of the casing (outer passage vortex) interacts with the over the tip leakage vortex. These sequences can be observed from the sketch of Figure 2.8.

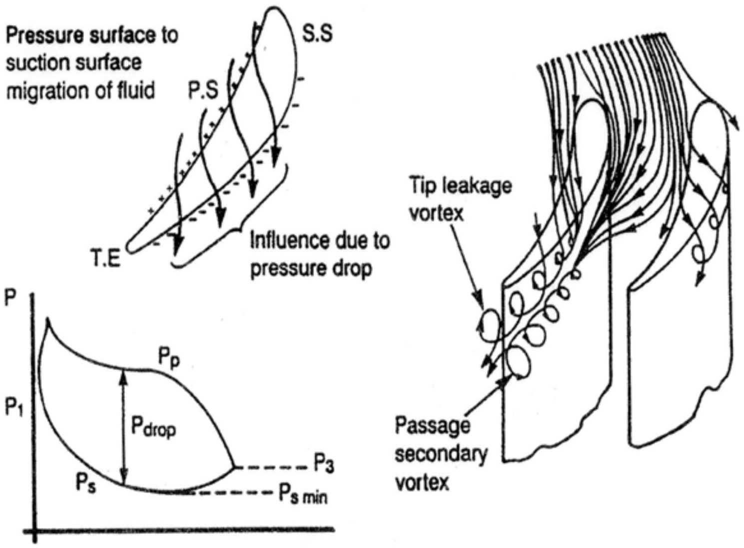

Figure 2.8: Outline of the flow in the region of an unshrouded turbine rotor blade [8]

Depending on the local thickness of the blade, relative to the gap height, two over the tip leakage flow regimes can be distinguished [9]. These are depicted in Figure 2.9. In this figure one can observe that, in both cases, the flow stream entering the gap from the pressure side of the blade separates at the tip, due to the sharp corner, and contracts into a jet. Wear and tear of the sharp corners of the blade is inevitable with time, and as the tip corners get eroded the flow contraction is reduced and in some cases completely eliminated. The separated flow region, and the vena contracta formed, at the blade tip limits the over the tip leakage flow. However the subsequent mixing of this stream generates considerable amounts of losses.

The reattachment of the separated flow region (separation bubble formation) depends on the blade tip thickness and on the local Reynolds number of the flow in the gap. Thus, for low Reynolds number ($Re < 100$) the flow is fully developed and laminar and does not separate. At $100 < Re < 1,000$ the flow separates at the tip corner and reattaches after a distance of two tip gaps. The flow is not totally mixed as it surfaces on the other side of the gap. At $Re > 10,000$, typical values in a gas turbine, the flow separates and reattaches after a distance of two to three tip gaps and emerges totally mixed, [8].

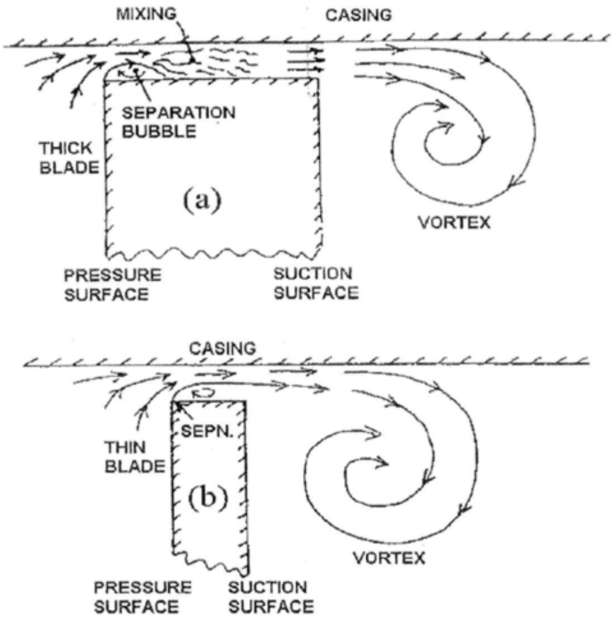

Figure 2.9: Sketch of the tip leakage flow patterns at two blade locations (near LE and TE) [9]

Hence, considering the case “a” of Figure 2.9, which represents a turbine blade cut, perpendicular to the camber line, and near the leading edge, turbulent mixing of the flow takes place after the reattachment of the separated region. This not only increases the flow entropy (losses) but is also accompanied by an increase of the static pressure due to the expansion region that exists above the rotor blade. If the static pressure and the OTL flow discharge coefficient (C_d), after mixing, are known, then through a 2D orifice flow similarity calculation, one could roughly determine the OTL flow rate and the associated entropy generated [10].

Case “b” of Figure 2.9 represents a region near the trailing edge of a turbine blade. Here one can see that, due to the small thickness of the blade, the leakage jet does not reattach the surface of the blade tip. Therefore the pressure difference across the gap is smaller since no pressure recovery within the gap takes place. In this case all the losses arise when the leakage jet that emerges from the tip gap as it breaks into a vortex that mixes with the passage main stream flow.

In Figure 2.10, one can see the OTL model proposed by Bindon [11], where he recognizes a chord-wise flow in the separated region on the blade pressure side tip. Moreover, he suggests a massive over the tip flow injection into the mainstream at the location of the highest static pressure gradient on the blade tip surface. Nonetheless, Denton [9] recognizes that the OTL flow emerges from the blade tip clearance over a longer chord distance, reducing the amount of losses generated with respect to Bindon's model. And in fact, no other researcher has identified Bindon loss generation model to be accurate [8].

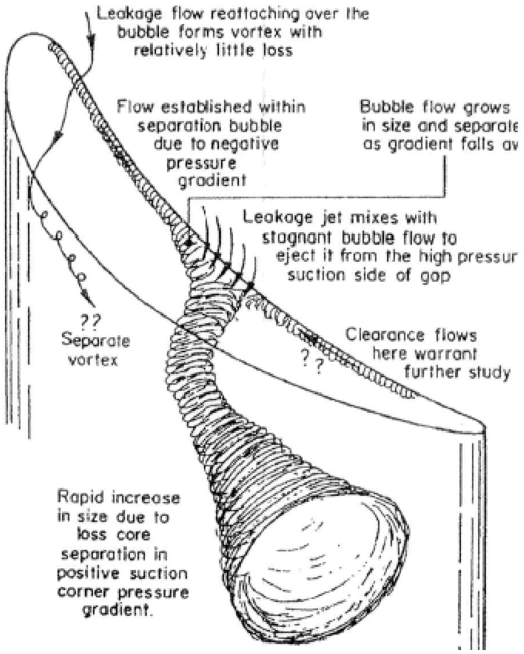

Figure 2.10: Bindon's over the tip leakage flow model [11]

When the over the tip leakage flow of a free-tip turbine rotor interacts with the secondary flows (as discussed in the previous subsection), the flow field within the turbine stage passage becomes extremely complex. So that, even today, researchers do not fully agree upon the full details of it. One such matter is related to whether or not the relative wall motion of the casing inhibits the leakage flow. Yaras and Sojlander [12] claimed that viscous forces between the blade tip surface and the casing were unimportant as compared to the pressure forces, and therefore the relative motion of the end wall did not affect the gap flow significantly, as illustrated in Figure 2.11. However Graham's [13] experimental results did not agree with Yaras and Sojlander's model.

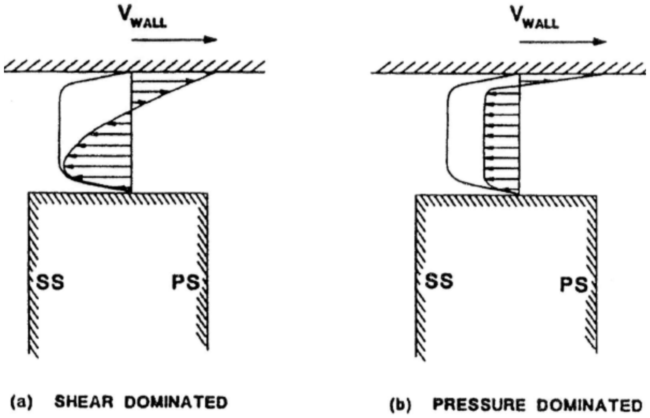

Figure 2.11: Sketch of the possible velocity distributions in the tip clearance [12]

One of the most interesting discrepancies comes from the fact that Bindon & Morphis [14] uniquely found, in their one and a half low speed annular rig, that rather than rolling totally into a vortex, the over the tip leakage flow remained mostly as a flat high energy wall jet. A sketch of their findings is depicted in Figure 2.12.

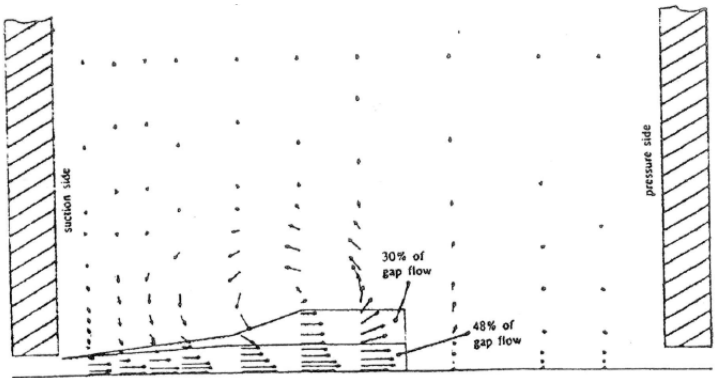

Figure 2.12: Sketch of velocity vectors normal to the mainstream emerging from the clearance [11]

Whereas it is most probable that the benefits of having a high energy wall jet in subsequent turbine blade rows would be lost, due to the non-matching incidence angle of the jet flow field with the downstream stator vane, its advantages could be realized when an exhaust diffuser is coupled to the gas turbine power plant. Indeed the over the tip leakage wall jet would energize the diffuser boundary layer and thus postpone stall. Hence, higher static pressure recoveries within the diffuser will be possible.

2.3 Shrouded versus free-tip turbine rotors

Since the aerodynamic losses of the turbine stage increase with the increasing of the gap between the turbine rotor and the casing, it is important to keep this gap to the minimum that is mechanically achievable (around 1% of the blade height). Additionally, the tip gap varies over the turbine operating cycle because of thermal expansions and mechanical displacements. Plus, over the engine life span the gap increases due to the metal wear and tear.

One practiced method of mitigating the over the tip leakage flow is achieved by introducing a shroud to the rotor blade. In Figure 2.13, two high pressure turbine rotor blades are depicted: one shrouded and the other free-tip. Both rotor blades present orifices from which fluid (air bled-off of the HP compressor) is ejected to create a boundary layer of cooled air (~700 K) that protects the metal (through film cooling) from burning and from the combustion products.

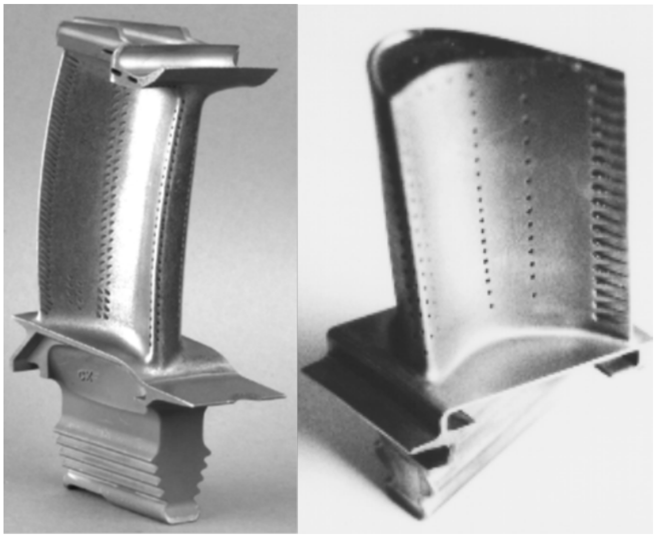

Figure 2.13: High pressure shrouded (left) and unsrhouded (right) turbine rotor blades [15]

Even though the shroud over the rotor increases the aerodynamic efficiency of the turbine stage, the added weight at the tip of the blade creates considerable mechanical (mainly centrifugal) stresses at the root of the blade and to the disc itself. Therefore, the rotational speed of a shrouded blade will have a lower limit compared to an unshrouded one. Since the work output is proportional to square of the blade rotational speed (via Euler turbine equation), an advantage of using unshrouded blades becomes apparent. Nonetheless, the shroud damps out the blade vibrations which is an advantage as compared to unshrouded rotor.

Another disadvantage of the shrouded rotor, if a high pressure turbine stage is considered, is that the flow stream temperature entering this stage is about 1,750 K, well above the metal melting point (~1,400 K), and consequently the shroud requires to be cooled as well as the blade itself. The additional use of cooling air for the shrouds results in an increase of the overall engine efficiency loss. Plus, efficient cooling of shrouds is still an “art” rather than “science”.

To maintain good efficiency while keeping compactness of the gas turbine it is common in aero-engines to split the turbine into two to three sections (i.e., multi-spools) with different rotational speeds. Figure 2.14 shows a three-spooled turbine section of an aero-engine while a two-spooled configuration is shown in Figure 2.15.

One advantage of multi-spool machines is in their adaptability to the development of engine derivatives and design architecture. As an example a Rolls-Royce three-spool engine is more flexible to application changes than a similar two-spool gas turbine engine. For this reason, we may observe that a given family of Rolls-Royce engine could cover a wider market range than its 2-spool counterparts. On the other hand, multi-spooled engines add mechanical complexity to the machine and hinder operation reliability/maintainability. For industrial applications, where weight is not an issue but reliability is, it is very common to find single shaft gas turbines.

In the turbine section, the fluid expands as mechanical energy is extracted from the fluid and consequently the annulus area increases to maintain the axial velocity of the stream nearly constant. The annulus area of the turbine not only increases but often the mean, or pitchline, radius from the inlet of the HP to the LP turbine exit increases as well, as observed from Figure 2.14 and Figure 2.15. This is because the loading factor of its stages ($\Delta h_t/U^2$) needs to be low to maintain good thermodynamic efficiency of the turbine. Then in the LP section where low rotational speeds are needed (speed limit imposed by fan tip Mach number limitation), the mean radius needs to be high in order to increase the blade velocity. The HP turbine, that drives the HP compressor, has a much higher rotational speed than the LP (≥ 3 more) and therefore needs to be at a lower radius to minimize stresses [8].

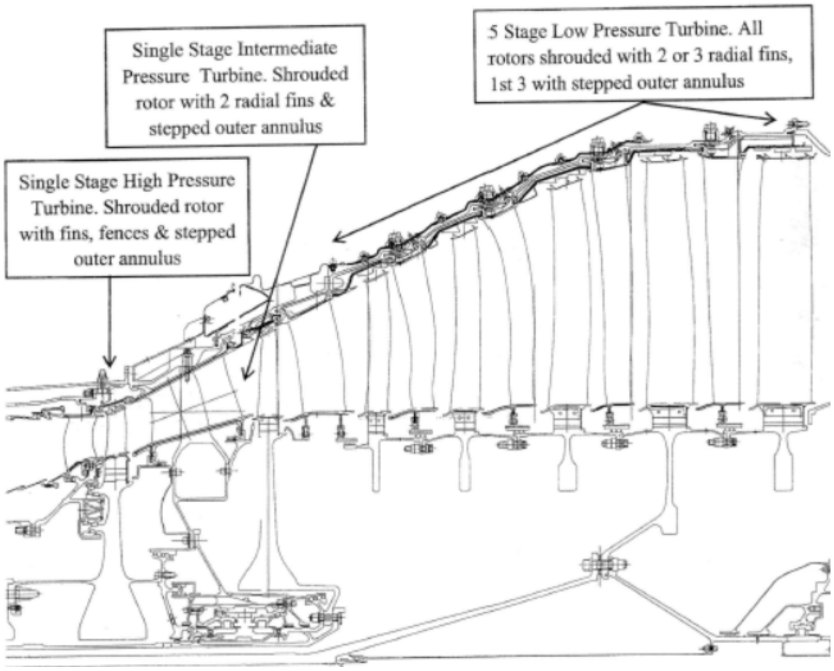

Figure 2.14: Sketch of an aeroengine turbine section with a shrouded HP rotor [8]

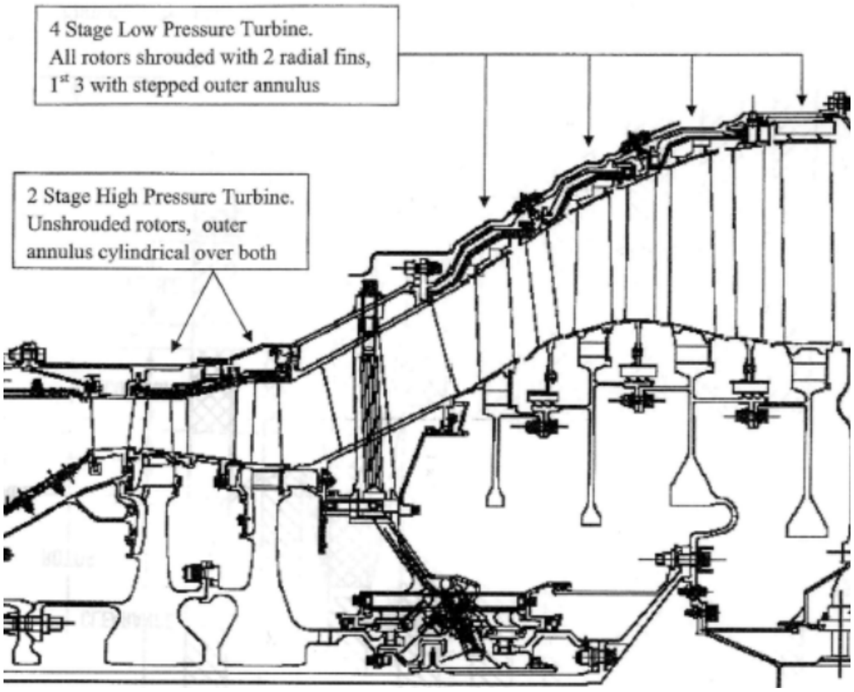

Figure 2.15: Sketch of an aeroengine turbine section with an unshrouded HP rotor [8]

Therefore, since there is a significant advantage in having a flow path increase in the turbine section, the outer annulus casing needs to flare up. And as a consequence any axial movement of the rotor shaft will increase the nominal gap between the blade tip and the outer casing in unshrouded rotors as depicted in the sketch of Figure 2.16. However, with a shrouded rotor, since there is a labyrinth seal between the rotor blade and the outer casing, the gas stream can flare up below the rotor shroud without any increase of the gap between the blade and the casing, as long as the blade shroud sealing fins stay engaged with the stepped outer wall. This can be observed in Figure 2.17.

For these reasons, the outer casing is usually not flared over the rotor if an unsrhouded blade is to be used, Figure 2.15. With this configuration, to achieve the required radius change from the inlet to the outlet of the turbine, the length of the engine has to increase (weight penalty). Moreover, to accommodate the volume of the expanded gas, the annulus area increase has to be done by lowering the inner radius at the exit of the rotor, which adds geometric complexity of the turbine sections as depicted in Figure 2.15.

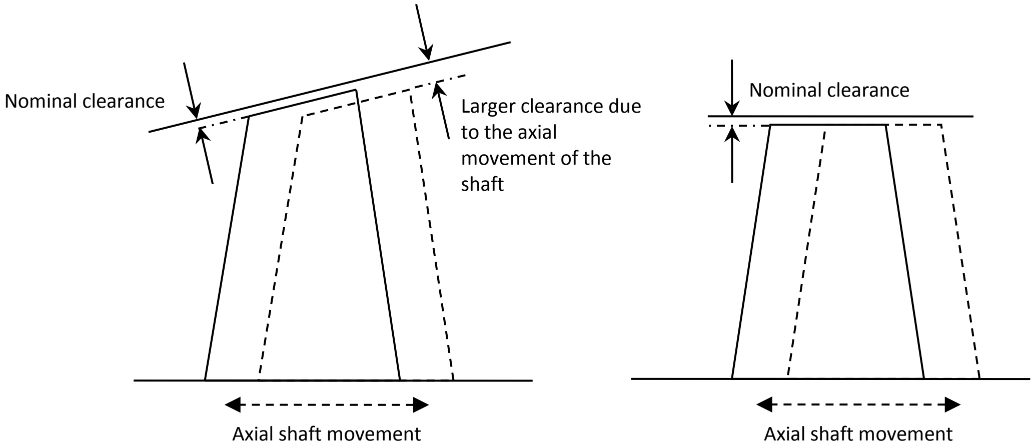

Figure 2.16: Sketch of an unshrouded rotor tip clearance variation due to the shaft axial movements with a flared (left) and a horizontal (right) shroud

As mentioned in section 2.2 , the flow emerging from over the tip of the blade is not deflected (no work extraction results from the over the tip flow) and therefore it will emerge with a different exit angle (co-swirl angle) to that of the mainstream, causing severe aerodynamic losses due to the mixing of the two streams. This is the case whether the rotor blade is shrouded or unsrhouded. In shrouded rotors, however, to diminish these mixing losses, fences are mounted at the rear of the blade, aft the labyrinths, as depicted in the sketch of Figure 2.17. This configuration deflects (and therefore extracts work) part of the fluid that passes through the sealing gap to achieve a similar swirl angle as the mainstream flow.

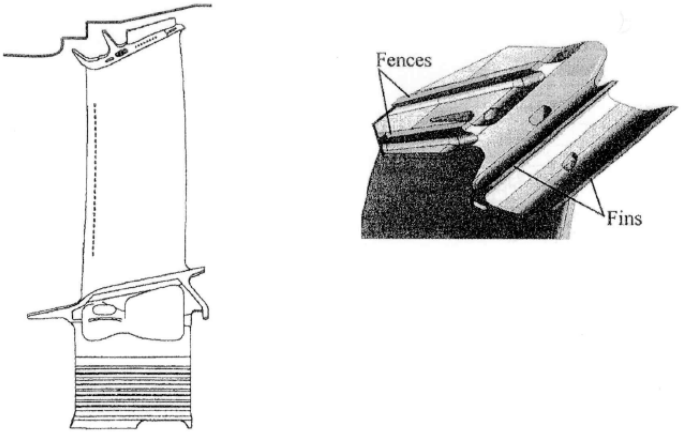

Figure 2.17: Sketch of high pressure shrouded turbine rotor seal [8]

As noted, both shrouded and unshrouded rotor blades present advantages and inconveniences. As a result both rotor blade types have been and are still in successful commercial service.

2.4 Turbomachinery unsteady flow interaction

Since the rotor changes its relative position with respect to the stator blades with time and the incoming wakes and passage vortices from the upstream blade rows causes a non-uniform flow distribution, an unsteady flow field is generated at the inlet of the downstream blade rows.

The flow field unsteadiness can be divided into two groups:

a) a random part due to turbulence
b) a periodic part related to the blade passing frequency

To determine whether a flow field can be treated as quasi-stationary or unsteady, a non-dimensional analysis based on the reduced frequency $\overline{f}$ is utilized. The reduced frequency is described as the ratio of the convective time t_{conv} over the inverse of the disturbance frequency f_{dist}.

$$\overline{f} = \frac{t_{conv}}{1/f_{dist}} \tag{2.2}$$

When values of the reduced frequency are in the order of $\overline{f}$ << 1, the problem at hand can be considered quasi-stationary. When $\overline{f} \sim 1$, unsteady and quasi-steady effects coexist, whereas if $\overline{f}$ >> 1 unsteady effects dominate. In this study $\overline{f} \sim 2$ [16].

Potential flow interaction

Turbomachinery blade rows inherently generate pressure fields in both up and downstream. A periodic pressure field is indeed generated as a consequence of the interaction between the stator and the rotating rotor blades. As stated by Hodson [17] the interaction between their potential fields influences their respective flow fields and yields loss generation, noise and blade vibration among others. Dean [18] found that this temporal pressure variation (bow waves) affects the total pressure field upstream and concluded that its effect can be modeled as a work process. The potential field decays exponentially with the distance as investigated by Parker and Watson [19].

Wake-blade interaction

At the trailing edge of each turbine blade there is a momentum deficit of the flow field called wake. Meyer [20] defined a wake as a negative jet directed at the blade profile trailing edge. These wakes move downstream to the next blade row where they are "chopped" by the rotating motion of the rotor. Because of the relative velocity difference between the blade suction and pressure sides of the rotor blades, downstream of the generated wakes, the wakes move at higher speeds on the suction side than in the pressure side. Consequently, the wakes exit the passage row concentrated along the suction side of the blade. Kerrebrock and Mikolajczak [21] investigated the transport of rotor wakes in transonic compressor stages and presented a wake transport theory that allows for the determination of losses in the stage.

Vortex interaction

In low aspect ratio turbines, the interaction of secondary flow vortices can be more important than those of the wakes, since vortices occupy a large portion of the channel span. It was found by Binder et al. [22] that vortex breakdown occurred as the passage vortices were chopped off by the rotor, in a similar manner as the trailing edge wakes, with a consequent conversion of this kinetic energy into turbulence. However, recently, Behr [16] proved that strictly speaking, upstream wakes are not "chopped" by the rotor, rather the wake vortices wrap around the blade leading edge and are bent and stretched on each side of the blade.

2.5 Losses in turbomachinery

Losses in internal turbomachinery channels have been distinctly classified according to their origin of formation. These are: profile losses, end wall losses and leakage losses. Though the loss mechanisms associated with them are rarely independent from each other. A very reliable way of quantifying the losses is in terms of the entropy generation, as the entropy is a thermodynamic quantity that describes irreversibility of a process. Once entropy is created, it cannot be destroyed. Entropy is defined according to the Gibbs' equation:

$$s - s_{ref} = c_p \cdot \ln\left(T / T_{ref} \right) - R \cdot \ln\left(P / P_{ref} \right) \tag{2.3}$$

This thermodynamic variable of state has the advantage in turbomachinery that it is independent of the frame of reference used and is also independent of whether the other variables (temperature and pressure) are either the static or total values.

Denton [9] identifies three fluid dynamic processes that create entropy:

- *Viscous friction (and turbulence)*, which comprises boundary layers and free sheer layers as in mixing processes, e.g. leakage jets such as encountered in the rotor clearance gap.
- *Heat transfer* across finite temperature differences such as encountered during blade film cooling.
- *Non-equilibrium processes* as occurring during sudden expansions or in shock waves.

Denton [9] also states that secondary flows do not introduce losses directly but because of the high velocity gradients present, viscous flow dissipation converts the kinetic energy within the secondary flow into losses.

Finally, and because this study is related to over the tip leakage flows, it is also instructive to state the origin of the losses associated with the over the tip leakage and the means that aerothermal engineers may use to mitigate them. One of the widest known relations to estimate the losses brought by the over the tip leakage flow is due to Denton [9] who considered a simple incompressible control volume analysis to derive the losses as:

$$\zeta = \frac{2C_d}{\cos\beta_2}\left(\frac{g}{h}\right)\left(\frac{c}{s}\right)\int_0^1\left(\frac{V_s}{V_2}\right)^3\left(1-\frac{V_p}{V_s}\right)\left[1-\left(\frac{V_p}{V_s}\right)^2\right]^{1/2}\frac{dz}{c} \qquad (2.4)$$

This simple relation was found to estimate the OTL losses within 20% of those obtained through measurements for a number of research turbines [8].

From Denton's equation, to reduce the OTL losses one can lower the discharge coefficient (C_d). However, most of the researchers found that it does not affect the total losses generated in the passage. Indeed, the flow separation at the blade tip pressure side corner restricts the OTL flow, reducing thus the C_d. Yet, its subsequent mixing process generates large amount of losses. On the other hand if the blade tip corners were rounded (probable service situation after wear and tear), the OTL would increase (higher C_d), but then the separation of the flow at the blade tip would disappear along with part of the mixing losses. Overall these two situations generate, on their own, about the same amount of losses and therefore trying to reduce the OTL losses by reducing the C_d is not a viable procedure.

Aerodynamically off-loading the blade tip region is another possibility of minimizing the OTL losses. That is by changing design parameters such as the blade exit flow angle (β_2), the exit velocity (V_2) or the pressure difference between the suction and pressure sides of the blade in the tip region (V_s and V_p). To achieve this, the aerothermal engineer can make use of winglets (or partial shrouds), leaning the rotor tangentially at the tip, or by reducing the reaction degree at the tip. All these methods present pros and cons.

Among these procedures, the variation of the degree of reaction seemed to present one of the best compromises [8]. Farokhi [23] showed, for his turbine, that a reduction of the tip reaction from 89% to 0% reduced the tip loss exchange rate by half. On the other hand this method increases the stator vane exit Mach number which makes the aerodynamic design of the rotor more difficult. The benefits of using rotor tip winglets were inconclusive and this area requires more research [8]. Leaning the rotor tip tangentially moves passage mass flow away from the tip region because of a redistribution of the radial forces. This method redistributes the load along the span of the blade, destroying, in other blade sections below, the efficiency gained by off-loading the tip. Plus it is, mechanically speaking, very challenging to achieve.

2.6 Static pressure recovery in diffusers

The objective of a diffuser in general is to efficiently convert the fluid dynamic pressure into static pressure rise.

Two major fluid parameters affect the performance of a diffuser: the inlet boundary layer displacement thickness (related to aerodynamic blockage) and the amount of swirl contained in the flow [24]. Also, the inlet turbulence intensity level is an important parameter that affects the diffuser performance.

The aerodynamic blockage for compressible flows in internal ducts is generally written as:

$$B = 1 - \frac{\dot{m}_{actual}}{\dot{m}_{ideal}} \tag{2.5}$$

For an annular diffuser with uniform inlet boundary layers the aerodynamic blockage can be simplified to:

$$B \approx \frac{2\delta^*}{h_{inlet}} \tag{2.6}$$

with

$$\delta^* = \int_0^\infty \left(1 - \frac{\rho u(y)}{\rho_\infty u_\infty}\right) dy \tag{2.7}$$

where h_{inlet} : diffuser inlet height

ρ_∞ : free stream density

u_∞ : free stream velocity

The shape of the external diffuser walls (straight, bell and trumpet shapes), and the rounding of the inlet corners do not influence significantly its performance. Moreover, Reynolds number effects on performance are inconsequential above a critical Reynolds number, i.e., Re_h = ~2.0 e+5. Plus, the inlet Mach number is not an important quantity either, at least in the subsonic regime [24].

The two most common diffusers used in axial turbine applications are found in the intermediate diffusers which are used in the two spool configuration of modern aero-engines to connect the high pressure and low pressure turbines and as exhaust diffusers used in ground based gas turbine power plants.

2.6.1 Intermediate turbine diffuser

In gas turbines the intermediate diffuser is mainly utilized in the aerospace industry. Indeed, today's high efficiency turbofans result from greater bypass ratios. That is a large fan at the front of the engine is used. Another issue is that this fan has to be as quiet as possible and therefore the relative tip Mach numbers are limited to ~1.3, to avoid excessive noise radiation as well as tip efficiency. Therefore the low pressure turbine that is linked to the low pressure compressor and fan has to turn at low speeds while maintaining its high efficiency and work output. A way of achieving this is by having the low pressure turbine rotate at higher diameters from the engine axis. And since the high pressure turbine has higher rotational speeds as it rotates at lower diameters from the engine axis, the connecting duct between the exit of the high pressure and inlet of the low pressure turbines forms an "s-duct" shaped diffuser.

2.6.2 Exhaust turbine diffuser

Coupling an exhaust diffuser to the last stage of a ground-based gas turbine can be very beneficial in terms of power output by generating a sub-atmospheric pressure at the discharge of the last turbine rotor row. In Figure 2.18, an illustration of a turbine and a portion of an exhaust diffuser are shown.

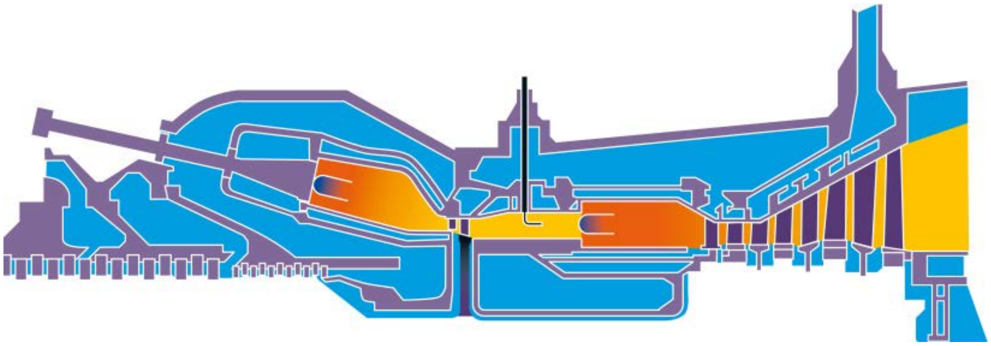

Figure 2.18: Sketch of a combustor, a turbine and an exhaust diffuser of a gas turbine [25]

Observations made by Bammert et al. [26] as well as other investigators in the field, show that the presence of the rotor over the tip leakage flow emerges as a co-swirling wall jet with an excess of axial momentum into the diffuser. This excess of momentum energizes the flow of the outer wall boundary layer postponing diffuser stall. Moreover tests confirm that some counter-swirl in the core flow optimizes the performance of the diffuser.

Based on these observations, a theoretical approach of the effect of the rotor tip clearance flow of unshrouded turbine rotors on the performance of diffusers was performed by Farokhi [27]. In Figure 2.19 a sketch used in his study is shown.

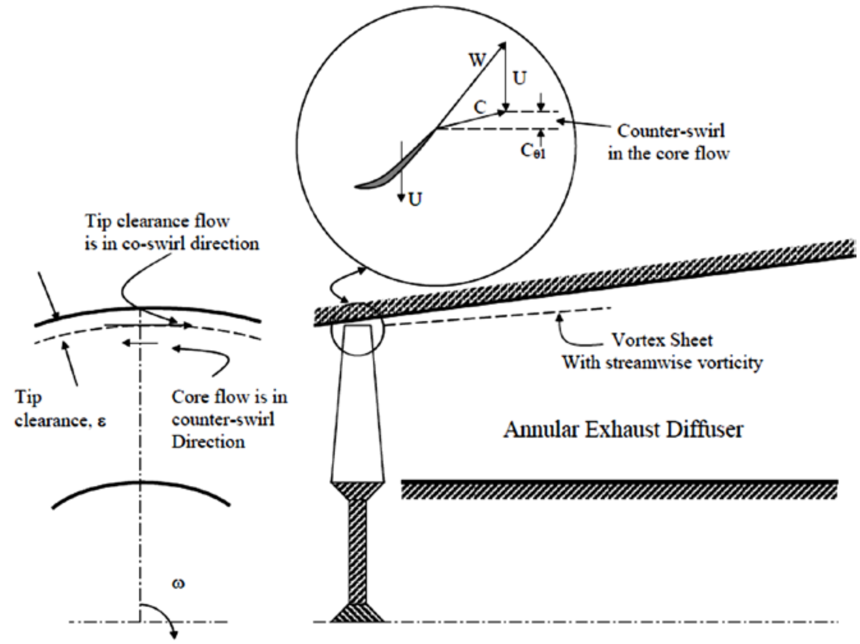

Figure 2.19: Drawing of rotor tip clearance flow discharging into an annular diffuser [27]

Taking Bammert, et. al. [26] assumptions, that is, the tip clearance flow and core flow expand to the same exit pressure ($|W_{2\varepsilon}| = |W_{2c}|$), the absolute swirl in the tip clearance exit is equal to the absolute swirl at the flow inlet, and that the axial velocity within the passage remains constant, Farokhi [27] represented the flow at the exit of a rotor through a series of velocity triangles. He distinctly discerned whether the rotor core flow was in co-swirl, counter-swirl or swirl free. In Figure 2.20 a sketch of his model with the core flow in counter-swirl is shown. He then identified that the presence of a small core counter-swirl flow generates a vortex sheet of axial direction as depicted in his sketch of Figure 2.19.

This vortex sheet enhances mixing of the outer diffuser flow and boundary layer, acting the role of a ”vortex generator”. The amount of the counter-swirl core flow, however, needs to be addressed.

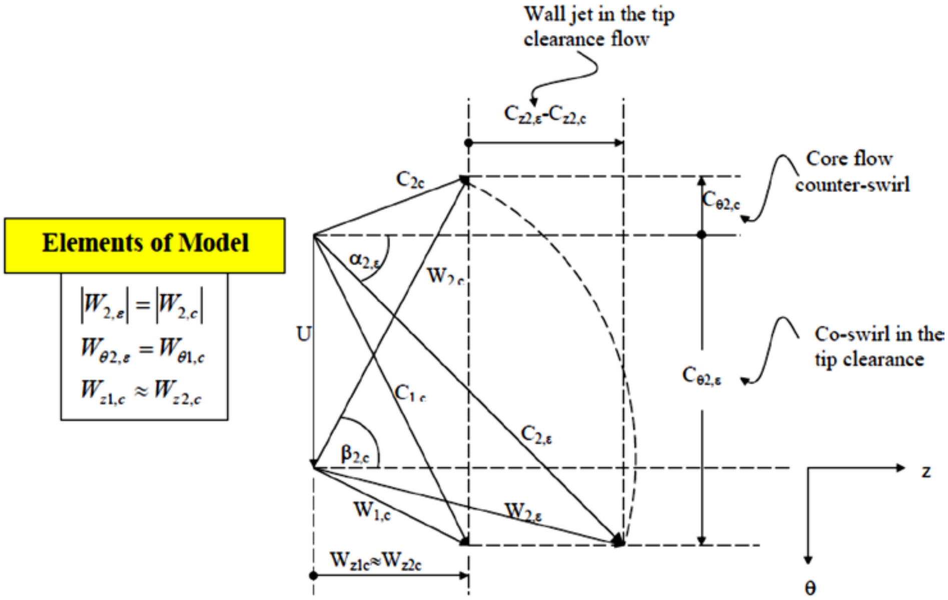

Figure 2.20: Farokhi’s rotor exit flow velocity triangles model with counter-swirl core flow [27]

3 CASE STUDY: ETH LEC AXIAL TURBINE RESEARCH FACILITY “LISA”

In order to validate the data obtained from the numerical analysis of this work, experimental data, previously acquired in an annular turbine test rig of the Laboratory for Energy Conversion (LEC) Institute of the ETH Zürich, was used. Figure 3.1 illustrates a scheme of the axial turbine research facility used at the LEC Institute and named “LISA”.

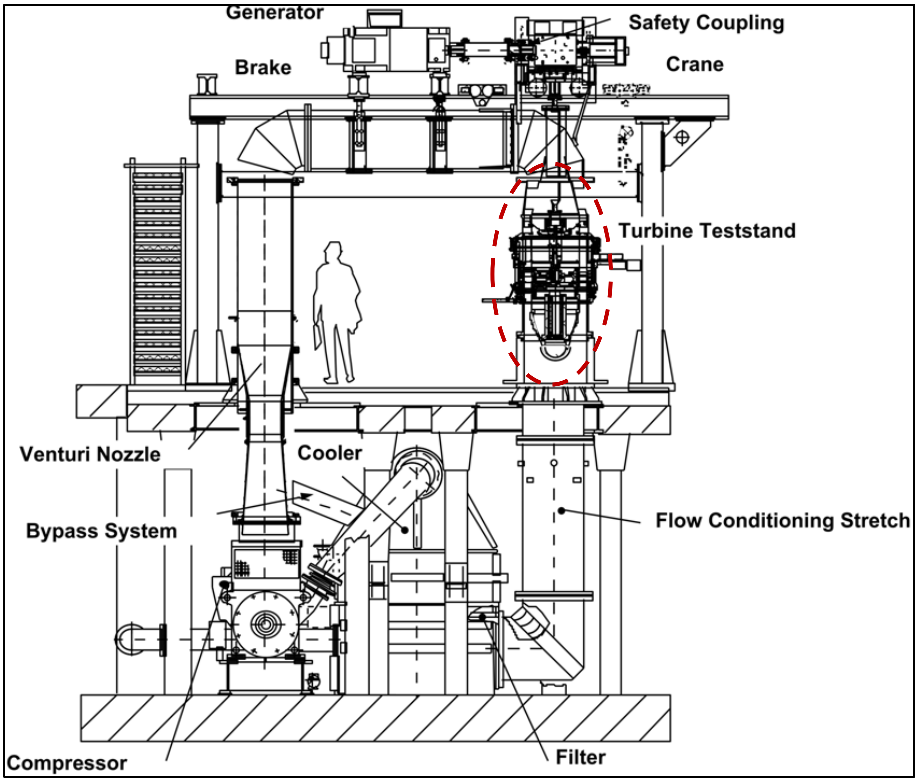

Figure 3.1: Schematic view of LEC's LISA research axial turbine [16]

To validate numerical design tools or to improve the performance of turbomachinery designs, it is essential to perform experiments. The kind of tests used depends not only on the objectives sought but also on the amount of money and time invested.

On one hand, short time duration scaled facilities exist. There, the fluid stored in tanks at high pressures is suddenly released through the turbine sections. These test rigs permit to achieve high pressure and high velocity conditions that are very similar to real engine conditions. The drawback is that only a quasi-steady condition is achieved. Plus the measurement campaign is limited to a few seconds. This fact, combined with the high transient test conditions, limits the accuracy and the spatial resolution of the measurements.

The most realistic testing conditions are achieved on real gas turbine test rigs. However this kind of test results to be very expensive and difficult to conduct, since most of the intrusive measurement techniques are not possible due to the high temperatures that are reign inside the turbine sections.

LISA is a continuously operating scaled subsonic turbine test rig where the generated power is released to a generator that ensures stable operating conditions. Thus, not only a steady state operation of the turbine is accomplished but also lower temperatures and flow velocities are achieved and therefore intrusive measurement techniques can be accurately used.

As depicted in Figure 3.1, the test rig extends across three floors. A fixed speed electrically driven radial compressor delivers the working fluid (air) to the turbine. The air circulates in a quasi-closed loop; an opening to the atmosphere exists at the exit of the turbine. The operation of the turbine is mostly limited by the operating map of the radial compressor. Resonance of the rotating parts (turbine, gear box) is another factor that limits the operating conditions of the test rig. The mass flow rate through the compressor is altered by adjustable inlet guide vanes and is measured by a calibrated venturi nozzle.

To control the turbine inlet temperature the air passes through a water-cooled heat exchanger. Plus the flow entering the turbine is kept as homogenous as possible thanks to flow straighteners and a piping dimensioning that restricts the flow velocity to values below 5 m/s in order to minimize pressure losses. The control of the turbine rotational speed is done with a DC generator to an accuracy of ±0.1 rpm. The power generated by the turbine is transmitted to the generator through a twin shaft arrangement. Therefore in a two turbine stage test configuration the torque of each independent stage is measured. In Table 3.1 important parameters of the present test facility are presented.

Table 3.1: LISA research turbine facility controlling parameters [16]

Compressor power	750 kW	**Turbine speed (max.)**	3,000 rpm
Compressor mass flow rate	6 to 13 kg/s	**Turbine torque (max.)**	1,500 Nm
Compressor pressure ratio	1.1 to 1.5	**Turbine inlet temperature**	35 to 55 °C
Generator power (max.)	400 kW	**Turbine exit pressure**	Atmospheric
Working fluid	Air	**Turbine tip diameter**	800 mm

In Figure 3.2 one can see a closer view of the turbine test stand. In the main flow path view of the turbine the blade rows are represented along with the plane position were an intrusive measurement campaign was realized.

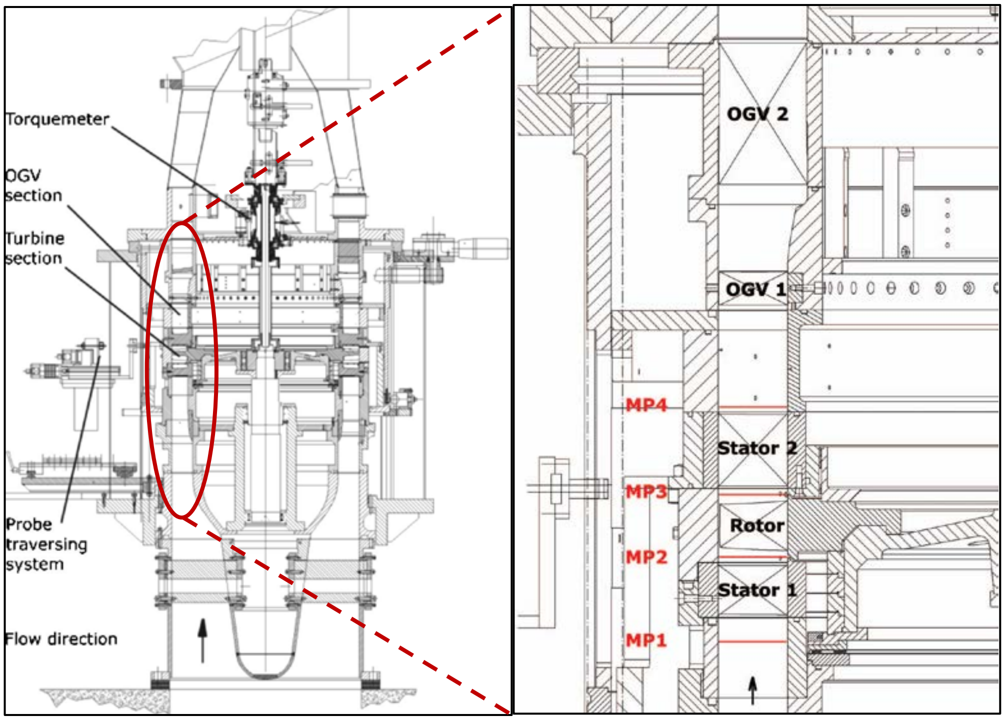

Figure 3.2: Amplified view of the axial turbine (left) and the turbine main flow path (right) [16]

With this test stand several blading configurations are possible as to model high pressure and low pressure steam and gas turbines. In this particular test a high pressure gas turbine, high loaded and low aspect ratio with an unshrouded rotor and one and a half stages was considered.

The measurement planes are located at a distance of 50% of the stator 1 axial chord at the inlet (MP1), from its leading edge, and at a distance of 15% of the respective rows axial chords form their trailing edge (MP2, MP3 and MP4). This can be observed from the sketch of Figure 3.3 where only the first stage of the turbine is represented.

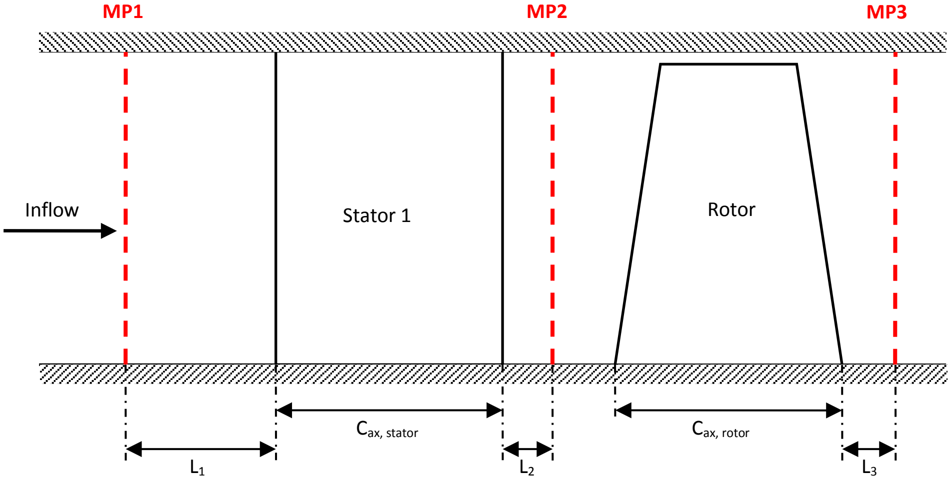

Figure 3.3: Sketch of the turbine first stage with the relevant dimensions

Therefore the measurement planes positions are defined as follows:

$$\frac{L_1}{C_{ax,stator}} = 0.50 \qquad ; \qquad \frac{L_2}{C_{ax,stator}} = 0.15 \qquad ; \qquad \frac{L_3}{C_{ax,rotor}} = 0.15$$

Where C_{ax} is the axial chord distance of the respective blade rows.

In Figure 3.4 one can see two pictures of the first stage rows: the unsrhouded rotor bladed disk (blisk) and a stator segment respectively.

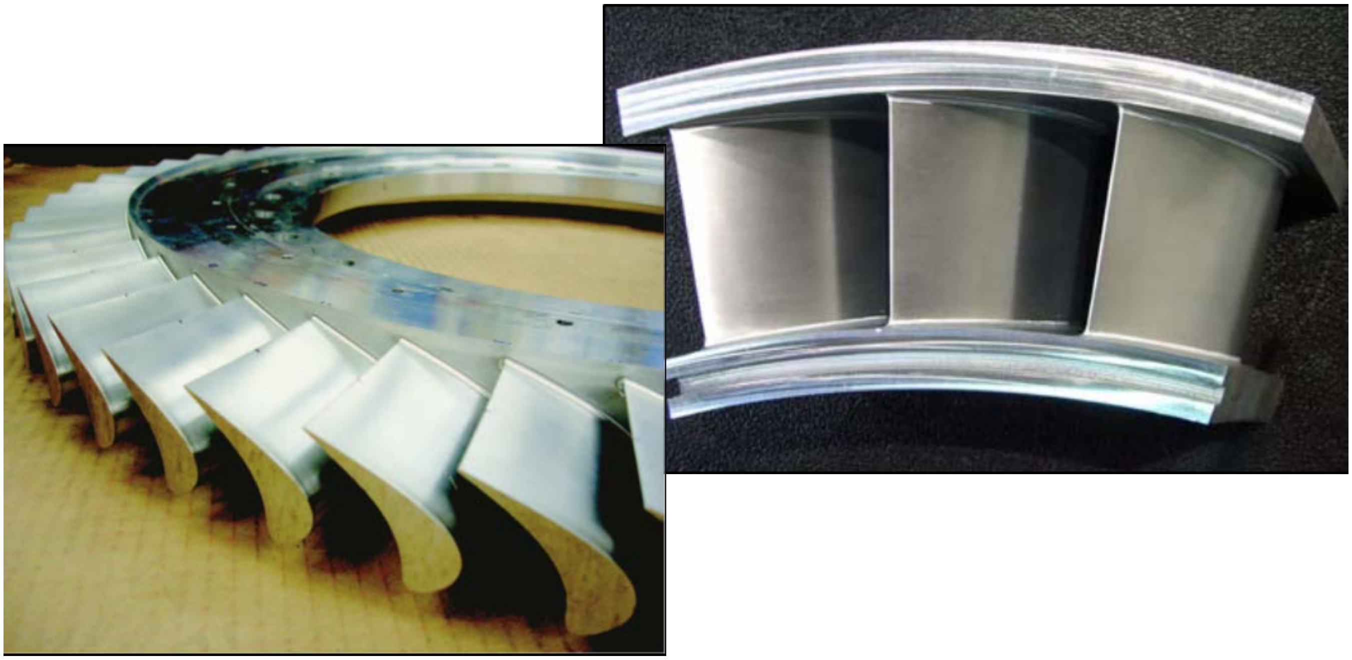

Figure 3.4: Unshrouded rotor blisk (left), and a stator segment (right) [16]

The stator 1 and rotor profiles at three span sections are depicted in Figure 3.5 and Figure 3.6 respectively, along with their pressure distribution at designed operation. Relevant design parameters of both blades are given in Table 3.2.

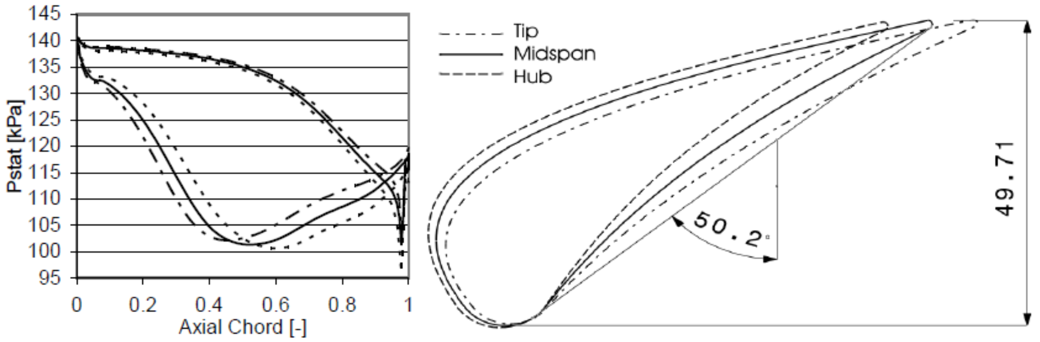

Figure 3.5: Stator 1 blade geometric parameters and profile pressure distribution [16]

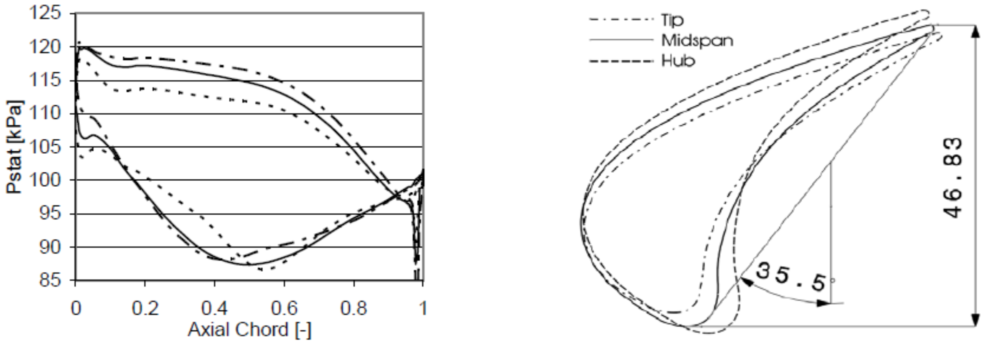

Figure 3.6: Rotor blade geometric parameters and profile pressure distribution [16]

Table 3.2: Design parameters of the first stage blades [16]

		Stator 1			Rotor		
		Tip	**Midspan**	**Hub**	**Tip**	**Midspan**	**Hub**
Radius	**[m]**	0.400	0.365	0.330	0.400	0.365	0.330
Number of blades	**[-]**	36			54		
Profile inlet angle	**[°]**	0.0	0.0	0.0	40.7	52.4	60.9
Profile exit angle	**[°]**	72.0	72.0	72.0	-67.4	-66.6	-65.8
Turning angle	**[°]**	72.0	72.0	72.0	-108.1	-119.0	-126.7
Stagger angle	**[°]**	52.9	50.2	46.8	40.2	35.5	30.3
Axial chord length	**[mm]**	49.61	49.71	49.82	43.41	46.83	50.08
Chord length	**[mm]**	85.37	80.88	76.40	59.68	59.72	60.46
Pitch	**[mm]**	69.81	63.70	57.60	46.54	42.47	38.40
Leading edge radius	**[mm]**	6.20	7.00	8.00	3.24	4.00	4.30
Trailing edge thickness	**[mm]**	1.21	1.30	1.38	0.98	1.10	1.28
Throat diameter	**[mm]**	20.01	18.53	17.07	16.08	14.42	13.25
Throat area	**[mm^2]**	46,582.8			54,780.5		
Fillet radius	**[mm]**	2.00	X	2.00	X	X	3.00
Aspect ratio	**[-]**	0.82	0.87	0.92	1.17	1.17	1.16
Chord / pitch ratio	**[-]**	1.22	1.27	1.33	1.28	1.41	1.57
Zweifel number	**[-]**	0.75			1.01		

The stator and rotor model the shape of an internally cooled high pressure gas turbine stage as one can observe from the profile geometry and parameters of the blades with large leading edge radii and profile thicknesses. Because of the large thickness design at the leading edge of the blades, an acceleration and deceleration occurs in the front suction side as depicted in the profile pressure distribution of Figure 3.5 and Figure 3.6. The Stator and rotor profiles are both stacked along radial lines that intersect the axis of rotation. The stator along its leading edge and the rotor along its center of gravity to avoid bending stresses caused by the centrifugal forces originated during rotation.

Operating conditions at the turbine design point are given in Table 3.3. These values will be used as boundary conditions in the CFD analysis and the results will be compared to those measured.

Table 3.3: Measured operating condition at turbine design [16]

Rotor speed [rpm]		2,700
Pressure ratio (1.5 stages, total to static0 [-]		1.60
Turbine inlet temperature [°C]		55
Total inlet pressure [bar abs Norm]		1.40
Mass flow rate [kg/s]		11.70
Shaft Power [kW]		292
Hub/Tip diameter [mm]		660/800
Rotor tip clearance / blade span ratio [%]		1.0
1st Stage		
Pressure ratio (total to total) [-]		1.35
Degree of reaction [-]		0.39
Loading coefficient [-]		2.26
Flow coefficient [-]		0.56
Blade row relative exit Mach number (average) [-]	**Stator 1**	0.54
	Rotor	0.50
Reynolds Number based on true chord and blade row relative exit velocity [-]	**Stator 1**	$7.1*10^5$
	Rotor	$3.8*10^5$

Due to time and money restrictions the annular diffuser was not tested, and consequently no experimental measurements of its performance are available with this configuration. In the CFD analysis the stator 2, of this one and a half turbine configuration, was replaced by an annular diffuser. However, the first stage of this turbine provides with very realistic boundary and operating conditions for which the performance of the diffuser will be assessed numerically.

4 NUMERICAL METHOD

All the computations in this investigation were done with the commercial CFD software ANSYS CFX v13.0. This software is one of the most worldwide renown when dealing with turbomachines. This is not only due to the efficiency and large number of algorithm choices available when dealing with interfaces such as encountered in stationary and rotating parts, blade tips,…, but also partly due to the vast choice of turbulent models developed in house.

4.1 Governing differential equations and computing models

ANSYS CFX is a commercial numerical solver based on the finite volume implicit method to solve for the partial differential equations of the full 3D Navier-Stokes equations, the energy equation and in the case of the turbulent model chosen (k-ω based) the equation for the kinetic energy and the eddy frequency. The fluxes are discretized at each grid node where they are updated and from where the flow variables (velocity, temperature, pressures, etc.) are retrieved. A high resolution scheme is used to solve for the advection terms [29]. The high resolution scheme uses a central Difference scheme when the solution is stable and a 1st order upwind difference scheme when numerical instability occurs. This is made to ensure that a solution is reached. In this study some grid nodes are solved using the 1st order upwind scheme such as the wake regions in the vicinity of the trailing edges of the blades. The time stepping is done through a second order backward Euler scheme.

The turbulent model is solved exclusively using the 1st order upwind scheme. The turbulent model utilized in this study is the k-ω based Shear-Stress-Transport (SST) with automatic near wall treatment. This model was developed by ANSYS Germany [29]. It is said that this model predicts better regions of flow separation especially under adverse pressure gradient conditions. Moreover the use of automatic near wall treatment ensures that the boundary layers are accurately resolved. In function of the mesh refinement the near wall treatment switches automatically from wall functions to low Reynolds near wall formulations.

To stack the grids together (Stator + rotor + diffuser) the use of a general grid interface (GGI) connection was used. GGI gives the end user freedom to vary the grid topology across interfaces. That is the number of grid nodes on one side of the interface does not have to match the number or position of the nodes on the other side of the interfaces [29]. Therefore the fluxes are linearly interpolated across the interface grid nodes. This interpolating method is also used during transient rotor/stator computations, as the rotor mesh slides circumferentially with respect to the stator and diffuser.

In the analysis of rotating machinery where flows are solved in a rotating frame of reference, additional sources of momentum need to be computed to account for the effects of the Coriolis and centrifugal forces. The analysis of rotating machinery is done with the help of the available rotor/stator interface algorithms: *mixing plane*, *frozen rotor* and *transient rotor/stator*.

With the mixing plane algorithm the fluxes are averaged in the direction of rotation before they are passed to the next frame of reference. The Frozen rotor considers that the relative position of the rotor with respect to the stator is fixed and therefore fluxes are passed to the next row. In the case of the transient rotor/stator interface the fluxes are updated, passed to the next row and then the rotor grid is rotated to a new position where the fluxes will be updated again [28].

4.2 Geometry and meshing

In order to compare the performance of the exhaust diffuser after the turbine stage at different opening angles, it is important, not only, to capture the physics using the same mathematical models, but also to use similar computational domain constraints.

The whole computational domain is split into three parts, namely, a stator domain, a rotor domain, and finally an exhaust diffuser domain. Except for the exhaust diffuser domain that changes its geometry with different diverging angles, and the rotor domain that has two geometries, one shrouded and one unshrouded, the stator domain geometry remains unchanged for all cases studied.

4.2.1 Stator computational domain

The grid used is of the structured type with hexahedral cells and it was done with ANSYS TurboGrid v13.0. The turbine stator domain is depicted in Figure 4.1.

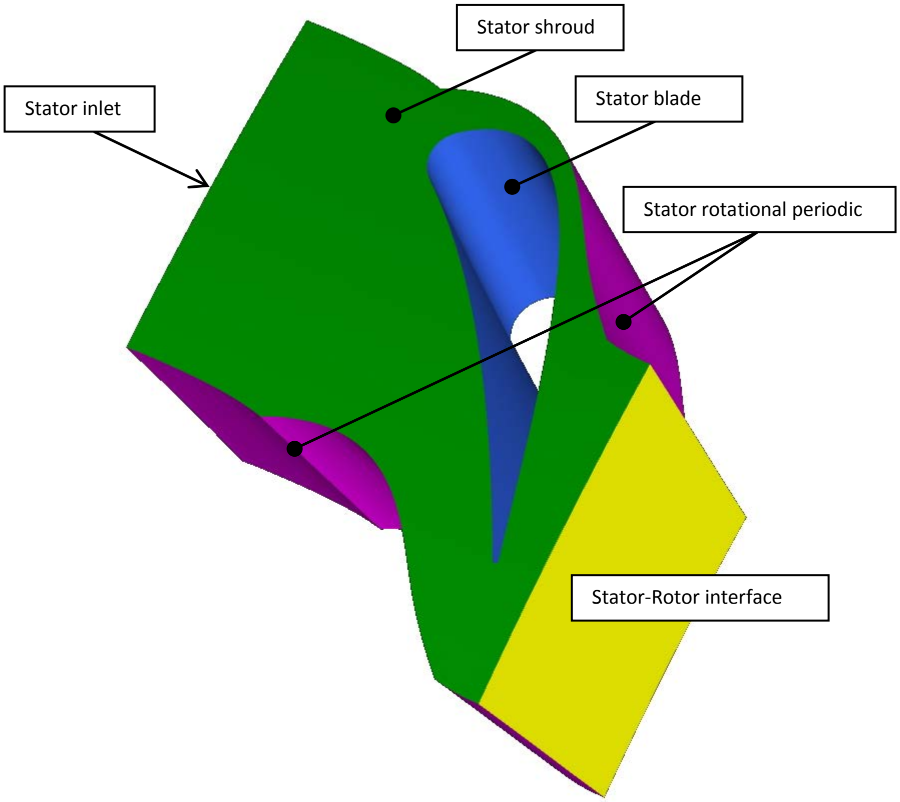

Figure 4.1: 3D mesh of the stator blade (grid lines switched off for clarity)

The turbine stator stage row is composed of 36 blades but just one blade with a pitch of 10˚ in circumference is modeled in order to speed up the convergence to a steady state solution. The stator is connected to the downstream rotor domain via an interface of the type "*Mixing plane*".

4.2.2 Rotor computational domain

As with the stator domain, the grid used to model the rotor is of the structured type with hexahedral cells, done with ANSYS TurboGrid v13.0, which can be seen in Figure 4.2.

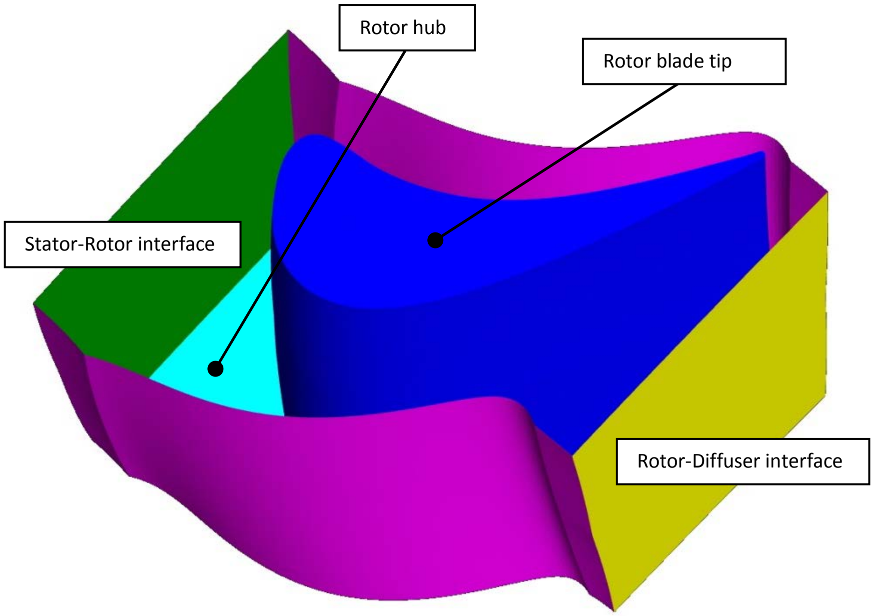

Figure 4.2: 3D mesh of the unshrouded rotor blade (grid lines switched off)

The turbine rotor stage row is composed of 54 blades, but in the same manner as done with the stator row, just one blade with a pitch of 6.67˚ in circumference is modeled in order to speed up the convergence to a steady state solution. Same as stator/rotor interface, the rotor is connected to the downstream diffuser domain via an interface of the type "*Mixing plane*".

The connection interface at the blade tip is of the type "general connection" (GGI). This type of connection simply linearly interpolates the computed variables between the adjacent nodes, as seen in Figure 4.3. This type of connection is user optional in this region. Using this method in this region helps to obtain an orthogonal grid, especially near the walls which is very important to obtain a reliable converged solution because of the high velocity gradients present. A drawback is that the solution gets a little bit diffused from side to side of the GGI. However, since this study is not directed to study each detail of the over the tip leakage flow, but rather to use it as an input boundary condition to the attached exhaust diffuser, the usage of GGI in this region is not such an inconvenient procedure.

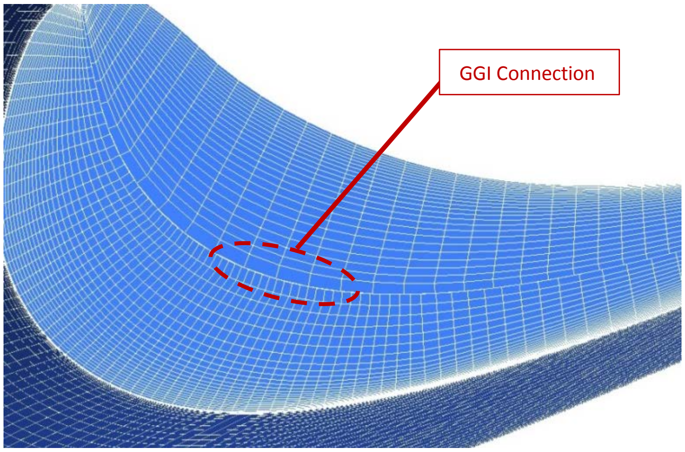

Figure 4.3: GGI mesh connection in the rotor tip region

Since the rotor is computed in the rotating frame of reference, for the case of the unshrouded rotor, the turbine shroud wall above the rotor needs to rotate in the opposite direction and at the same rotational speed as the rotor itself. The problem at hand is consequently summarized as a pressure driven leakage with a moving wall.

The shrouded rotor is meshed in a similar manner as the unshrouded one. The only difference is that there is no gap between the blade tip and the turbine rotor casing, which makes the final rotor grid to look like the stator one, as seen in Figure 4.4. This stage row is also computed in the rotating frame of reference but there is no moving wall relative to it.

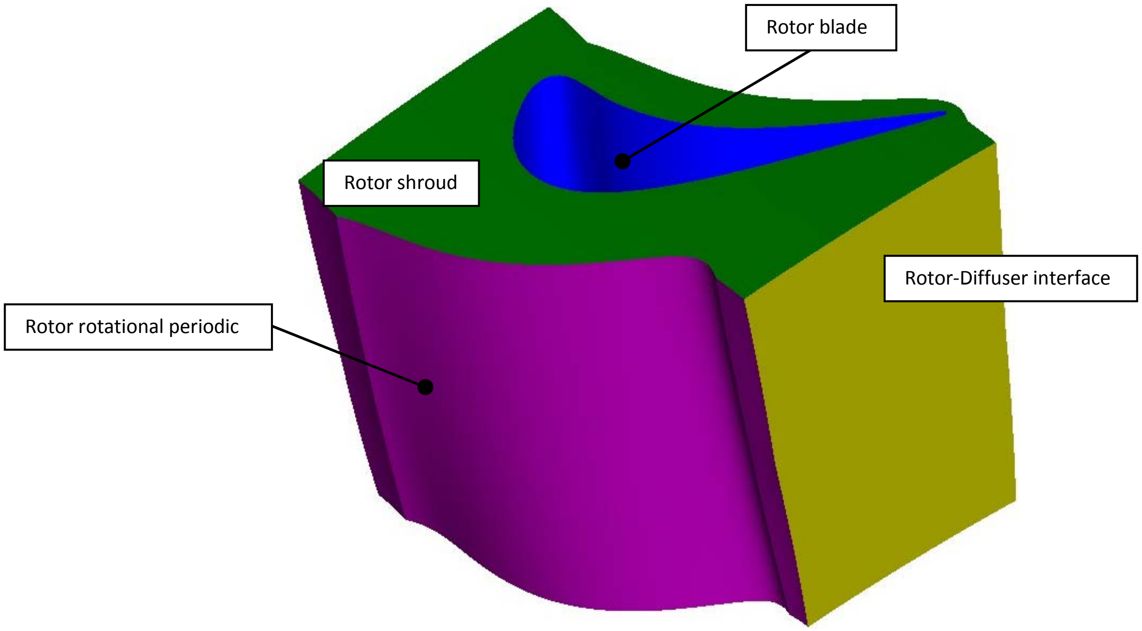

Figure 4.4: 3D mesh of the shrouded rotor blade (grid lines switched off)

4.2.3 Annular diffuser computational domain

The grid used is of structured type with hexahedral cells, it was done with the meshing program ANSYS ICEM CFD v13.0 that comes with the ANSYS CFX package. It was meshed using a 2D profile and extruded around the axis of rotation to obtain the 3D domain, as shown in Figure 4.5 and Figure 4.6.

The computational grid nodes have been clustered at the boundary layers as seen in Figure 4.5, especially near the shroud since the wall jet studied in this investigation is located in this region and therefore high velocity gradients are expected to occur there.

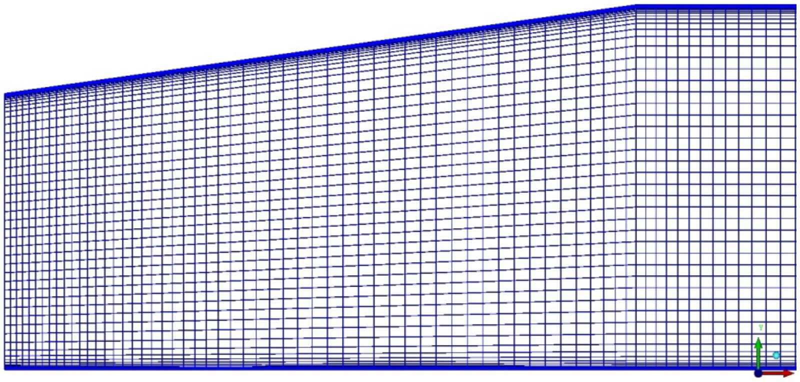

Figure 4.5: 2D mesh of the stage's annular diffuser

For practical reasons, especially when performing unsteady computations, the entire diffuser domain is split in 36 parts with a circular pitch of 10˚ in circumference, the same as the stator row domain.

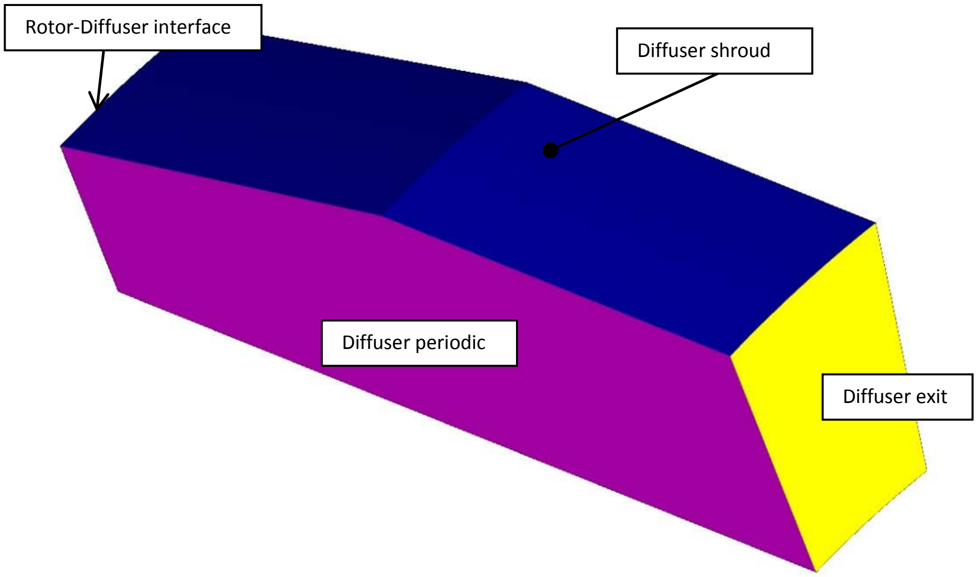

Figure 4.6: 3D mesh of the annular diffuser (grid lines switched off)

This geometry is the one that is studied in this investigation. As such, this part of the turbine is changed often (different diverging angles). However, for the sake of performance comparisons the total number of nodes will be kept as equal as possible, along with the boundary layer thicknesses.

To achieve a stable solution, above all in case of reverse flow, the diffuser has been elongated with a straight pipe of the same length as the diffuser itself. Plus the exit boundary conditions are easier to set in this manner.

4.2.4 Grid summary

Table 4.1 summarizes the mesh type and number of nodes used to model the geometry of the different parts that compose the computational domain of the turbine-diffuser stage. This grid is used during the steady state computations.

Table 4.1: Grid summary used in the steady state computations

Domain Part	Mesh Type	Nodes
Stator	3D Structured	~ 400,000
Rotor	3D Structured	~ 400,000
Diffuser	3D Structured	~ 200,000

To model the turbine-diffuser stage unsteadily, the same number of circumferential pitches is needed between rows. In this case a match is achieved with 2 stator and 3 rotor blade passages which corresponds to a circumferential pitch of 20°. The grid for this computation is summarized in Table 4.2.

Table 4.2: Grid summary used in the unsteady state computations

Domain Part	Mesh Type	Nodes
2 x Stator	3D Structured	~ 800,000
3 x Rotor	3D Structured	~ 1,200,000
2 x Diffuser	3D Structured	~ 400,000

In Figure 4.7 is depicted the entire computational domain when the grid is mirrored around the axis of rotation. Since rotating periodic conditions are used, the turbine stage-diffuser passages computed are a representation of the operation of the entire machine

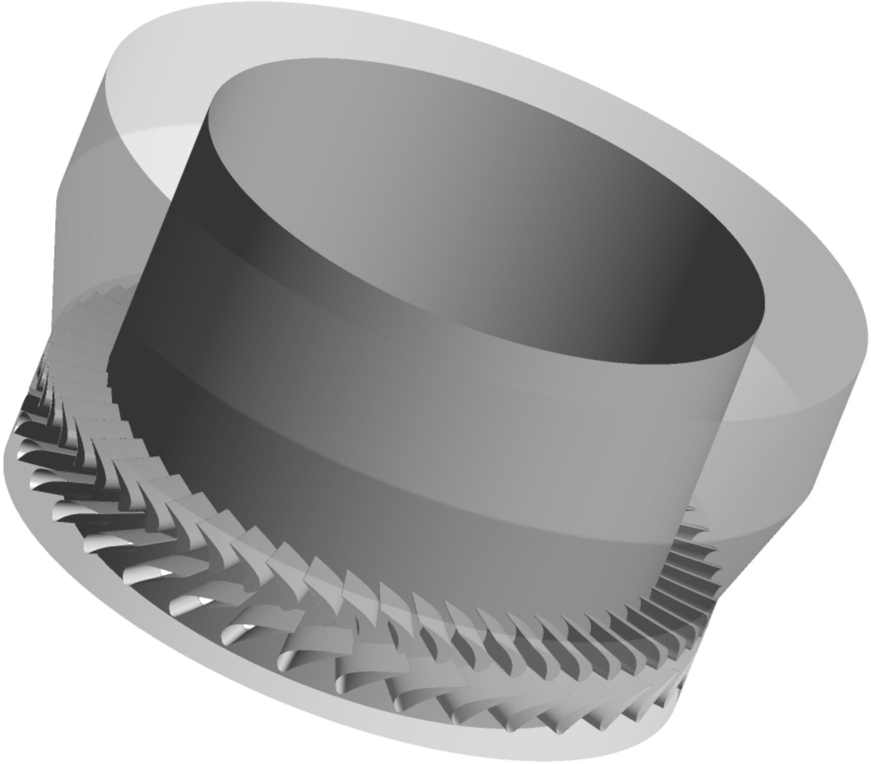

Figure 4.7: Complete computational domain when mirrored around the rotational axis

4.3 Boundary conditions

The fluid used for the calculations is 100% air which is the same gas as the one used at the LISA test stand of LEC. The gas thermodynamic properties utilized are summarized in Table 4.3

Table 4.3: Thermodynamic properties of the gas used in the CFD analysis

100 % air gas at a pressure ref. of 1.013 bar and temperature ref. of 298.15 K	
Density	1.183 kg/m^3
Heat capacity at const. pressure (Cp)	1,004.4 J/(kg.K)
Entropy ref.	0.0 J/(kg.K)
Enthalpy ref.	0.0 J /kg
Viscosity	1.831*e-5 (N.s)/m^2
Molar mass	28.96 kg/kmol
Gas constant (R_{gas})	287.1 J/(kg.K)

In addition, the boundary conditions used in this turbine-diffuser stage investigation are specified in Table 4.4.

Table 4.4: Turbine-Diffuser boundary conditions used in the computations

Inlet Conditions	Inlet total pressure	1.405 bar
	Inlet total temperature	328.0 K
	Inlet turbulence intensity	Low intensity
Outlet Conditions	Mass flow or static press.	***Variable***
Rotor rotational speed		2,700 rpm and Variable
Interface between stator & rotor		1) Mixing plane 2) Frozen 3) Unsteady
Interface between rotor & diffuser		1) Mixing plane 2) Frozen 3) Unsteady
Interface at rotor tip gap		GGI

Lastly, the setting of the inlet boundary conditions for the k-ω SST model is low turbulence intensity. This means that the turbulence intensity is set to 1% and the viscosity ratio μ_T/μ to 1.0. The turbulence intensity is used to estimate the initial turbulent kinetic energy k, and the viscosity ratio to calculate the specific dissipation ω.

5 RESULTS AND DISCUSSION

In order to accurately predict the performance of a turbine exhaust diffuser it is important to deliver the right boundary conditions to this one. Therefore as a first step it is necessary to validate the turbine stage itself against available experimental data. Coupling the diffuser to the turbine stage, a grid independence study is made next, followed by the investigation of the effect of the rotor tip clearance and swirl flow angle on the performance of the diffuser. Finally, to conclude, an unsteady turbine-diffuser investigation is performed.

5.1 CFD validation: Turbine stage specific flow features and performance map

This section has for objective to demonstrate that the numerical results obtained using this computational domain, boundary conditions, inter-stage algorithms and grid connectivity (GGI) are in line with the results measured in the laboratory in the actual turbine stage.

For this analysis, only the stator and the rotor are considered as seen in Figure 5.1. The interface between the stator and the rotor is of the mixing plane type. To avoid any numerical reflections from the outlet boundary due to the rotor blade proximity to it, an extension has been added at the rotor exit using an interface connection algorithm of the type “frozen rotor” with a one to one node connection (No GGI) to speed up computations.

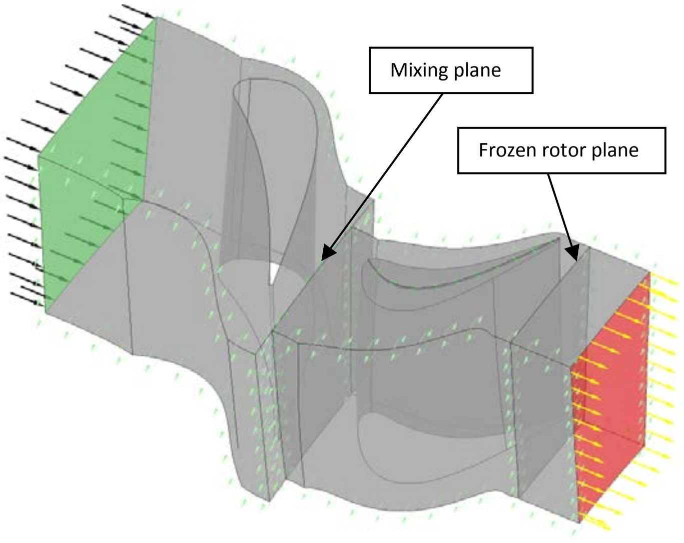

Figure 5.1: 3D model of the turbine stage with its relevant boundaries

Utilizing the same inlet and outlet measured values (total pressure, temperature and static pressure), performance parameters such as total pressure ratio, isentropic efficiency, degree of reaction, etc., of the turbine stage are evaluated and compared to the experimental campaign data obtained.

For the sake of completion the whole turbine characteristic is computed. Unfortunately the performance map could not be verified. One of the reasons is due to the power limitations of the compressor that feeds the turbine.

It is also important to mention at this stage that CFD should not be used as the exclusive tool to predict the performance of turbomachines. The prediction of the performance is determined from the extensive database and experience of each Original Equipment Manufacturer (OEMs), using simple 1D Thermodynamic/Aerodynamic formulations, interpolating between measured stages’ characteristics, and applying corrections whenever necessary, such as Reynolds number correction, Mach number correction, etc. Instead CFD should only be used as a tool to predict performance improvements through design modifications. That is the field where the power of CFD is so exclusive.

Also when doing CFD simulations on turbomachinery, it is very important to know beforehand the shape of their operational map so to apply the right boundary conditions. The inlet conditions are always provided by the total pressure and temperature. But for the outlet conditions either mass flow or static pressure are most commonly used. It is important therefore to know at which point one should use one or the other.

In Figure 5.2 one speed line of the turbine performance map is calculated. Plus one measured operating point is given for comparison [30]. As one can see, the computed total pressure ratio is in good agreement with the measured point at that flow capacity. As the turbine chokes, the relative local flow goes supersonic and the increase in pressure ratio is only possible through a series of expansion waves.

In Figure 5.3 the computed isentropic and polytropic total to total efficiencies are given in function of the flow coefficient. The measured total to total isentropic efficiency for one turbine operating point is also given [30].

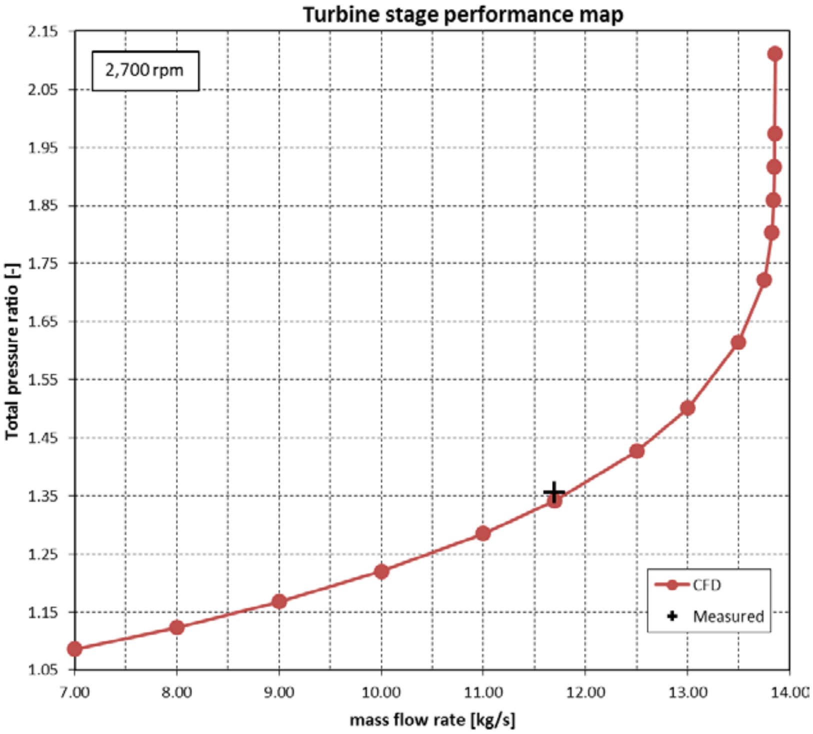

Figure 5.2: Measured point and computed performance line of the turbine stage

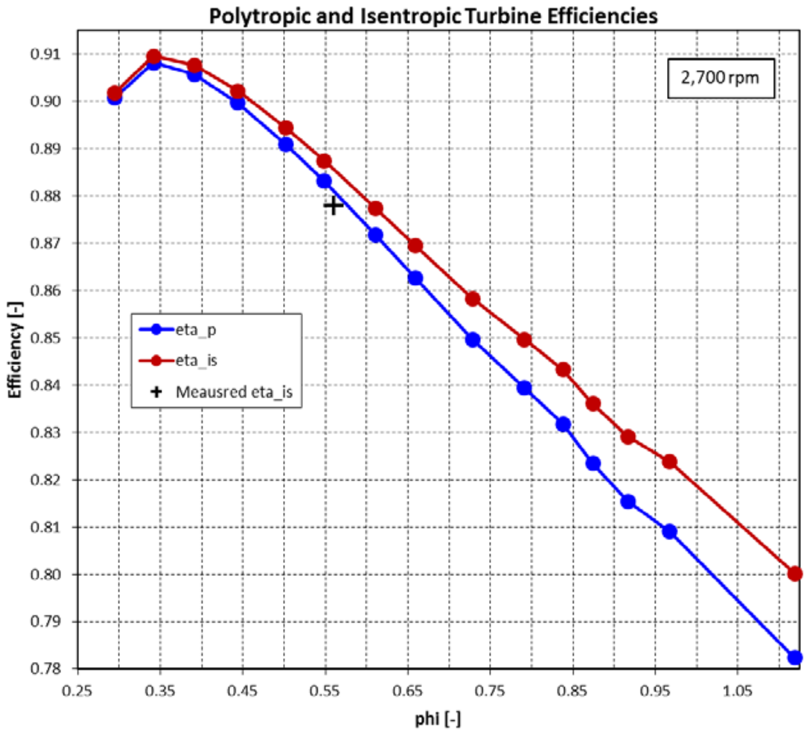

Figure 5.3: Measured point and computed turbine stage isentropic and polytropic efficiencies

Even though it is more common to express the efficiency of a turbine under its isentropic form, it is also sometimes relevant to refer the efficiency to a polytropic process (although the polytropic efficiency is more commonly used when dealing with compressors).

The total to total isentropic and polytropic efficiencies are given by equations 5.1 and 5.2 and are easily obtained from measurements of the thermodynamic variables of state of the gas.

$$\eta_{tt} = \frac{\Delta h}{\Delta h_{is}} = \frac{Power/\dot{m}}{c_{p,gas}\cdot T_{t,in}\cdot\left[1-\left(\frac{p_{t,out}}{p_{t,in}}\right)^{\frac{\gamma-1}{\gamma}}\right]} \tag{5.1}$$

$$\eta_{tt,pol} = \frac{\Delta h}{\Delta h_{p}} = \frac{\gamma-1}{\gamma}\cdot\frac{Ln\left(p_{t,out}/p_{t,in}\right)}{Ln\left(T_{t,out}/T_{t,in}\right)} \tag{5.2}$$

Since the turbine stage is manufactured out of two straight channel rings, a slight axial flow acceleration from the inlet to the outlet of the stage in unavoidable, and therefore the flow coefficient is given as:

$$\varphi = \frac{\left(u_{x,in} + u_{x,out}\right)/2}{u_{ref}} \tag{5.3}$$

From Figure 5.3 one can see that the total to total isentropic efficiency was slightly over predicted by more than 1% with respect to the measured value. This can be due to several factors such as using a steady state computation with a mixing plane algorithm, while measurements are done in the unsteady machine, or simply by modeling the turbulence among others.

A turbine set of characteristics: work coefficient, isentropic head coefficient and polytropic head coefficient in function of the flow coefficient for a rotor speed of 2,700 rpm are given in Figure 5.4. And in Figure 5.5 the variation of the degree of reaction in function of the flow coefficient is computed.

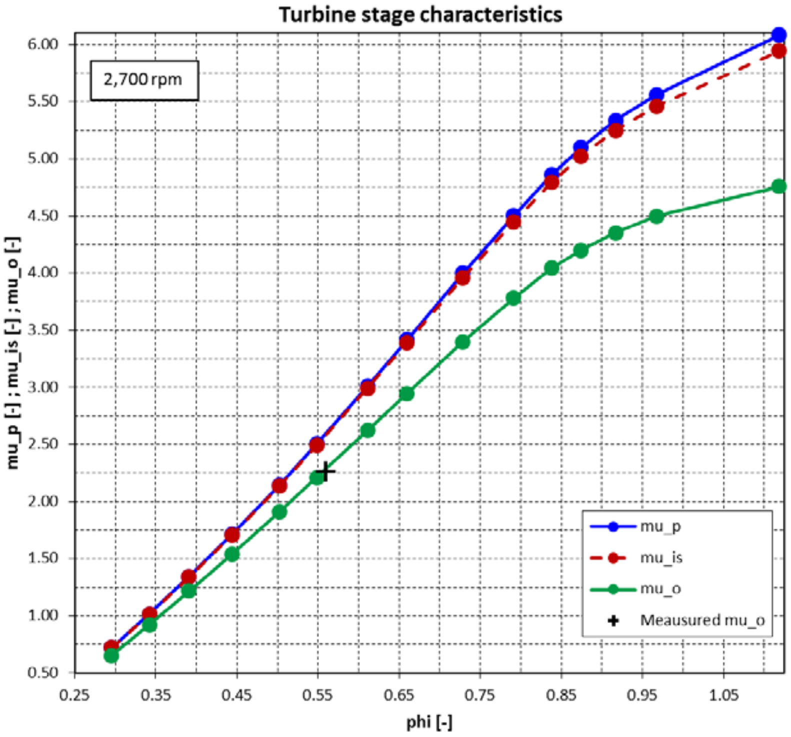

Figure 5.4: Measured point and computed turbine stage characteristics

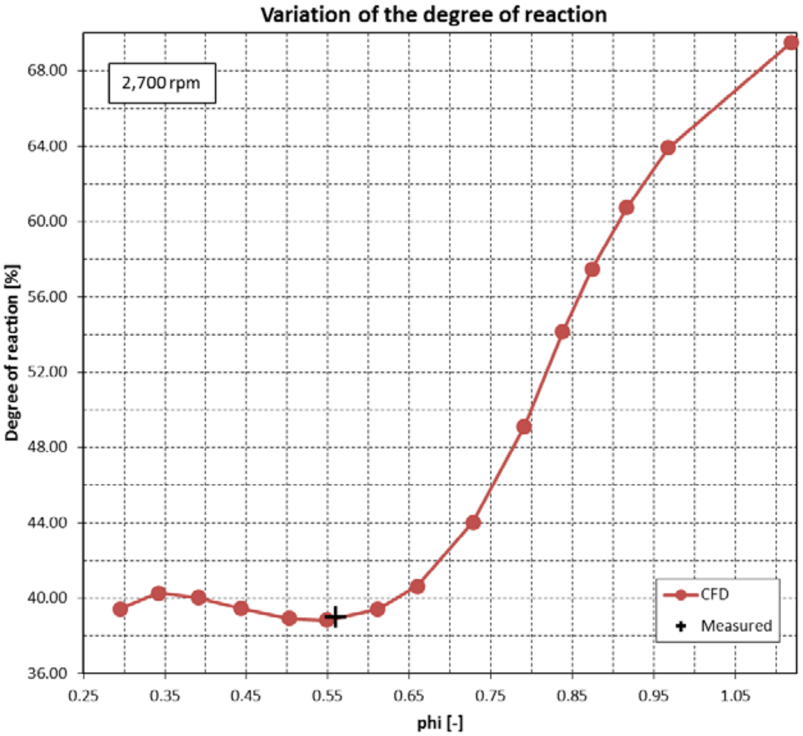

Figure 5.5: Measured point and computed degree of reaction variation of the turbine stage

The work coefficient is also obtained from measurements and is given by:

$$\mu_0 = \frac{Power / \dot{m}}{u_{ref}^2} \tag{5.4}$$

The isentropic and polytropic work coefficient are derived from the work coefficient and the total to total efficiencies as:

$$\mu_{is} = \mu_0 / \eta_{tt} \tag{5.5}$$

$$\mu_{pol} = \mu_0 / \eta_{tt,pol} \tag{5.6}$$

Lastly the degree of reaction of the turbine stage is stated as:

$$^{\circ}R = \frac{\Delta h_{rotor}}{\Delta h_{stage}} \tag{5.7}$$

From Figure 5.4 one can observe that the measured value of the work coefficient ($\mu_0 = 2.27$) is pretty accurately predicted numerically as well as the degree of reaction (°R = 39%) shown in Figure 5.5. Moreover the degree of reaction of the turbine stage remains more or less constant around °R = 40% for flow coefficients of $\varphi < 0.65$. As the stage starts to choke and because it occurs in the rotor, a sudden expansion of the gas takes place there and a large portion of the total amount of work done by the stage is shifted towards the rotor, thus an increase of the degree of reaction.

Figure 5.6 on the right represents the blade to blade contours of static pressure of the turbine stage at the mid-span plane from which the suction and pressure side of the stator and rotor blades are easily distinguished. On the left side of Figure 5.6 the entropy generation is given. Even though the entropy variable is independent of the frame of reference, discontinuous contours of the variable between the stator and rotor rows are perceived. This is because of the mixing plane interface algorithm chosen between moving and stationary parts.

Figure 5.7 illustrates the blade to blade relative Mach numbers of both rows. As expected, regions of high Mach number correspond to regions of low pressure and vice and versa. The fluid is accelerated within the passages up to the throat of their respective channel. After the passage throat, pressure is slightly recovered on the suction side of the blades due to their geometrical curvature.

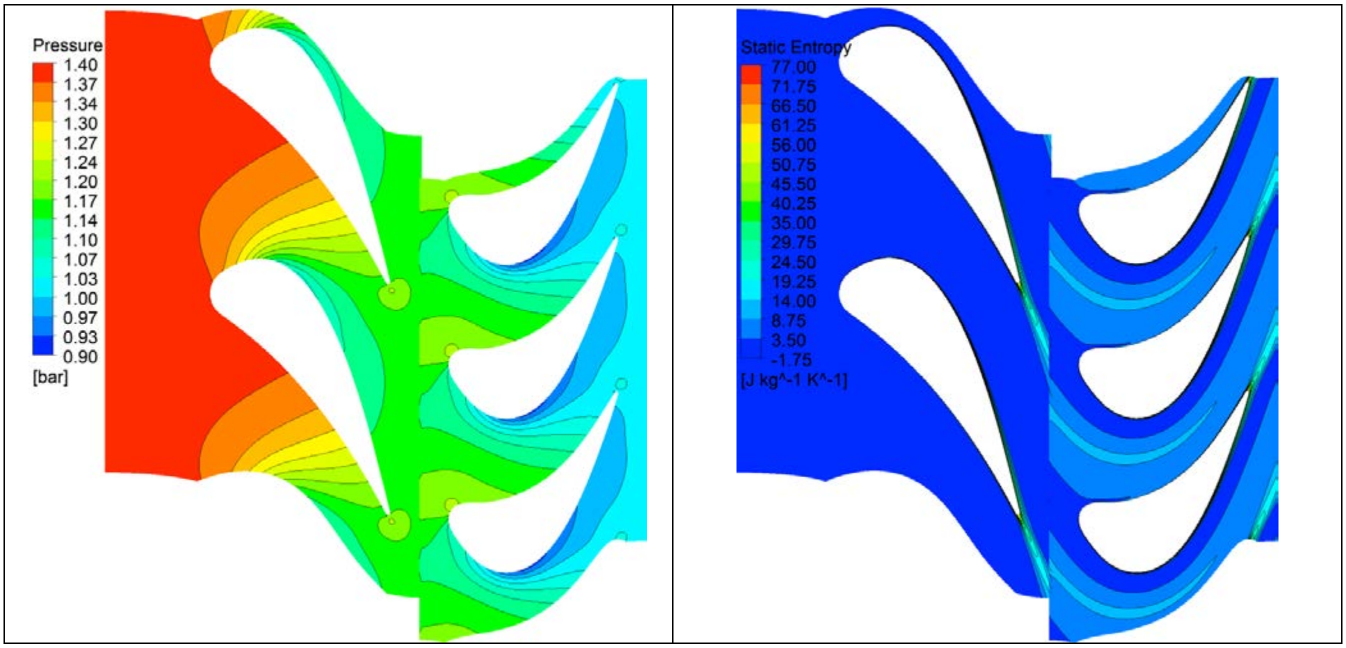

Figure 5.6: Turbine stage blade to blade contours of pressure and entropy (mixed rotor entropy)

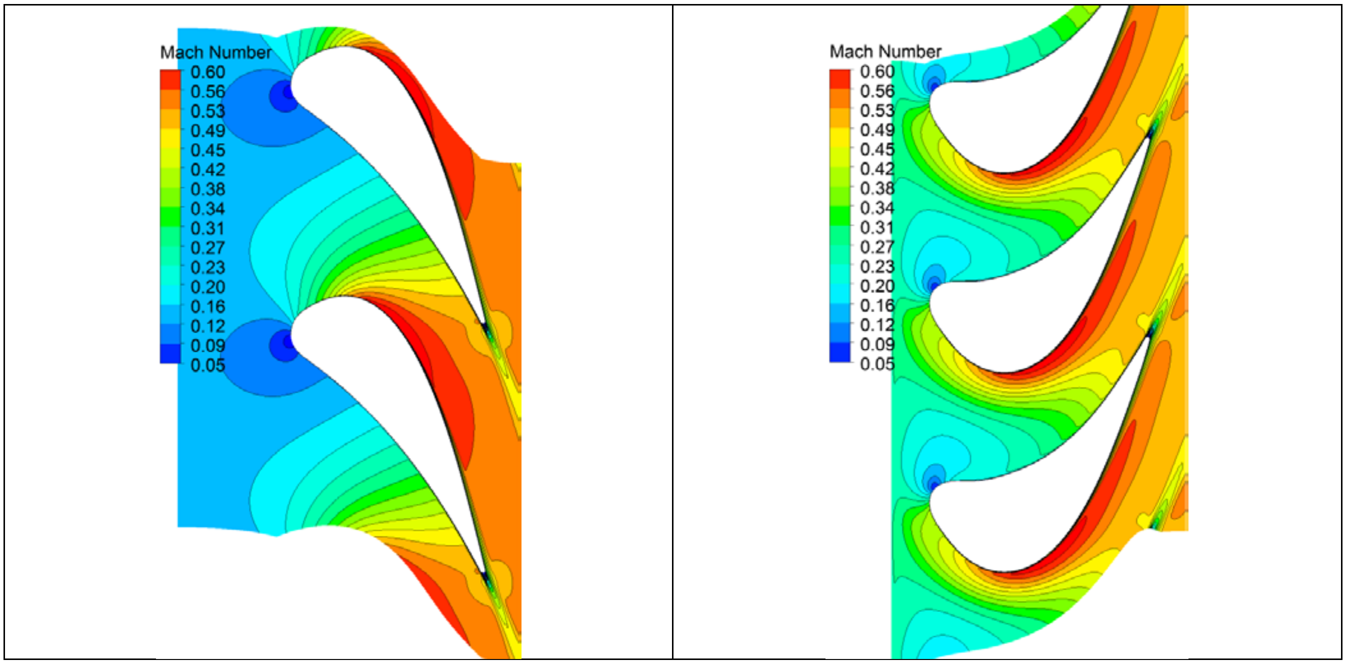

Figure 5.7: Stator and rotor contours of Mach number in their respective frame of references

In Figure 5.8 the total pressure (left) and Entropy (right) at the outlet plane of the stator are shown. At the trailing edge of the blade a deficit in total pressure and increase in entropy that spans the entire height of the channel is clearly noticed. This corresponds to the wake of the blade. Moreover, the locations of the two passage vortices near the stator hub and casing and connected to the stator wake on the suction blade side are appreciated.

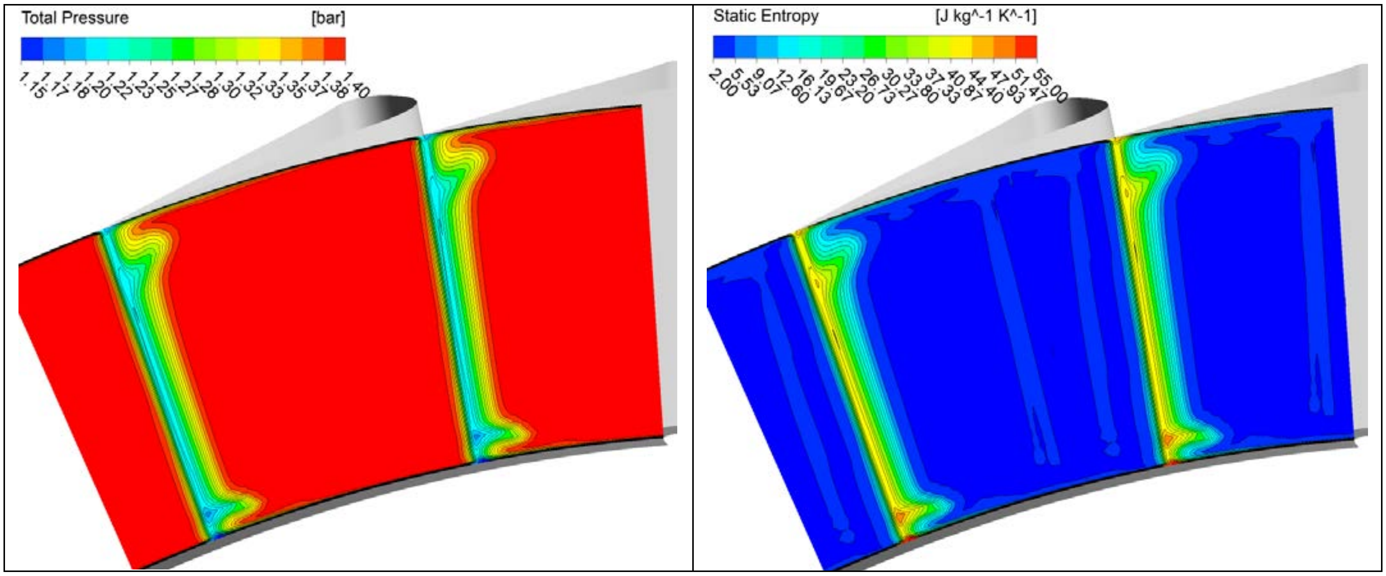

Figure 5.8: Total Pressure and entropy at the exit plane of the stator showing two passage vortices

The measured time-resolved total pressure contours at the exit plane of the stator row are displayed in Figure 5.9.

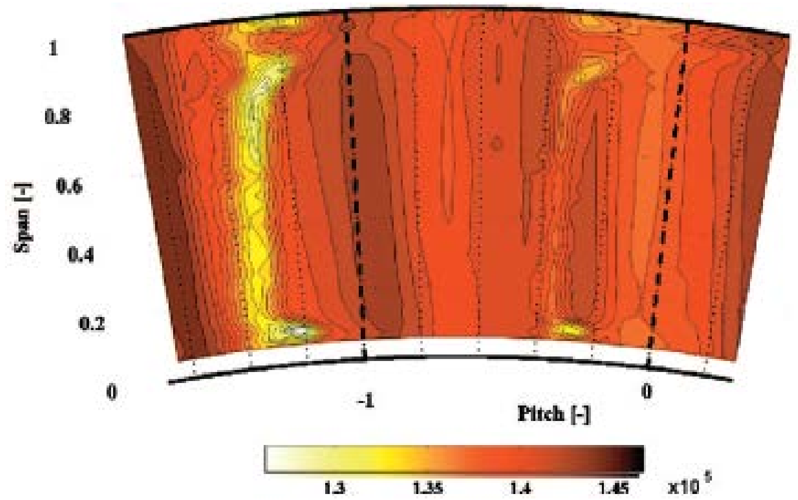

Figure 5.9: Measured time-resolved total pressure (in Pa) at the stator exit (two stator pitches) [30]

Comparing the total pressure contours provided in the two previous figures, it is evident that the two passage vortices are connected to the stator wake. At the casing endwall of Figure 5.9, one can identify the presence of an additional secondary flow feature, which is not clearly captured by the numerical simulation. This new flow feature is created within the stator passage, after the passage vortex at the casing has left the suction side [30]. This new secondary flow structure pushes downwards the tip passage vortex; hence its position is further down than the one computed.

Also, the total pressure (left) and Entropy (right) at the outlet plane of the rotor are shown in Figure 5.10. In this case three secondary flow structures can be identified, namely the two passage vortices and the over the tip leakage vortex. These structures are also connected to the rotor blade wake. It is clearly seen how the over the tip leakage vortex pushes down the tip passage vortex. Moreover the vortex from the rotor clearance generates most of the losses.

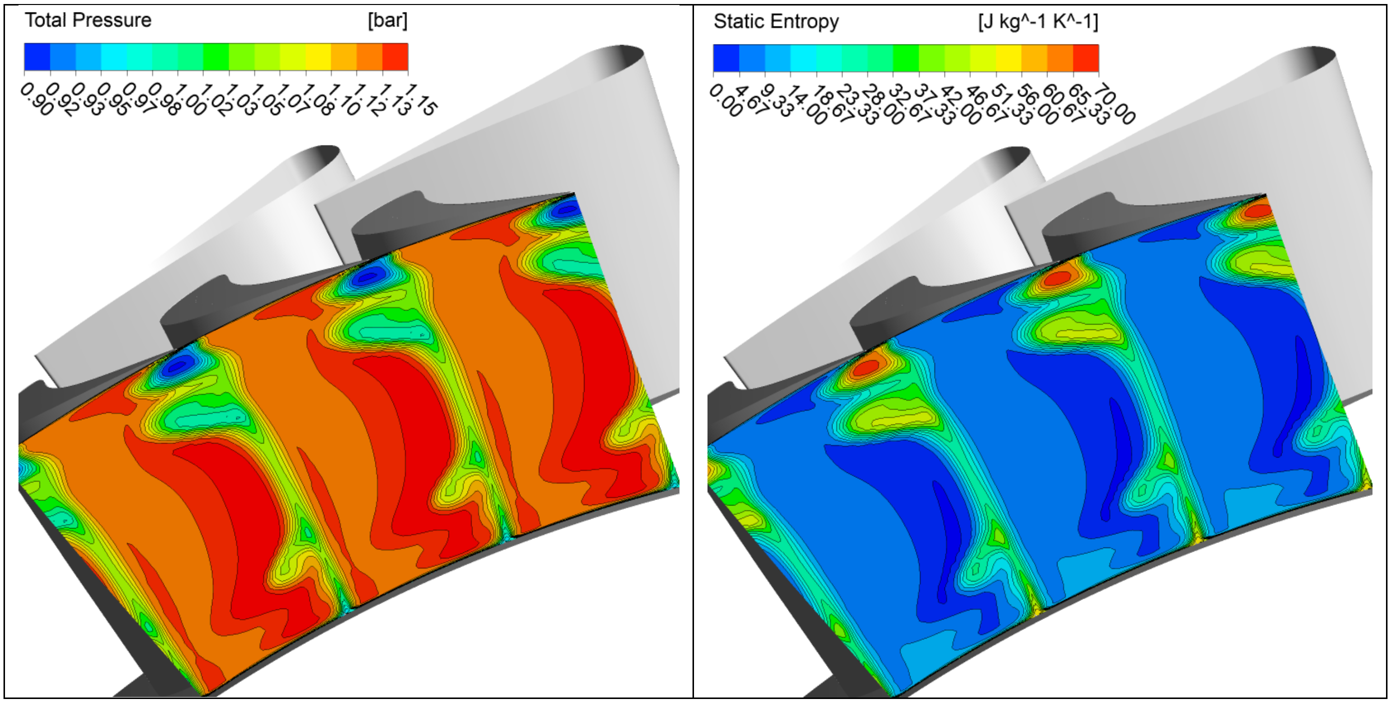

Figure 5.10: Total Pressure and entropy at the exit plane of the Rotor showing secondary flow structures

Figure 5.11 shows the measured time-resolved total pressure contours at the exit plane of the rotor row. The three vortex structures and their positions identified in the numerical simulation are also clearly appreciated. Plus measurements also show that the OTL vortex generates more losses than the other two. On the other hand, in the simulations, the size of the tip passage vortex seems to be bigger which contradicts the measured values where the OTL vortex is larger. It is evident that some discrepancies exist, but one has to bear in mind that the computations were done in a steady state basis and the measurements are time dependent.

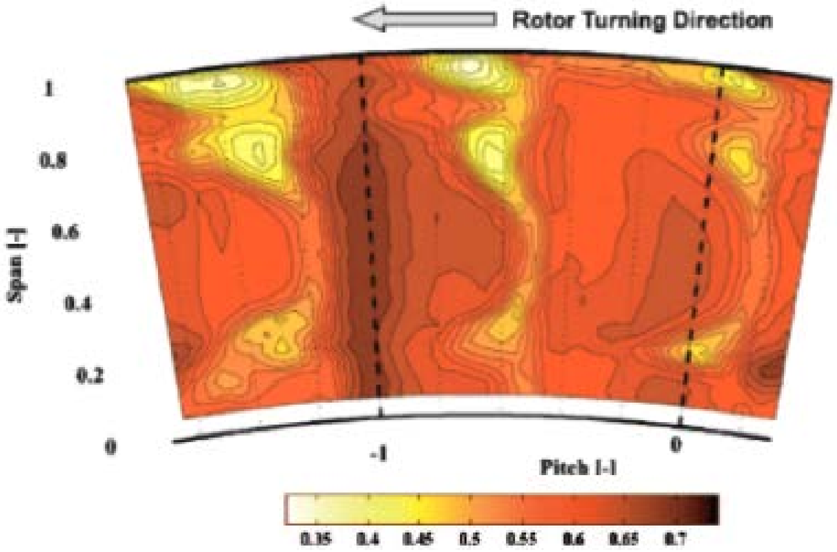

Figure 5.11: Measured time-resolved total pressure coefficient at the rotor exit (two stator pitches) [30]

In Figure 5.12 computed static temperature contours on the surface of the blades and hub are shown.

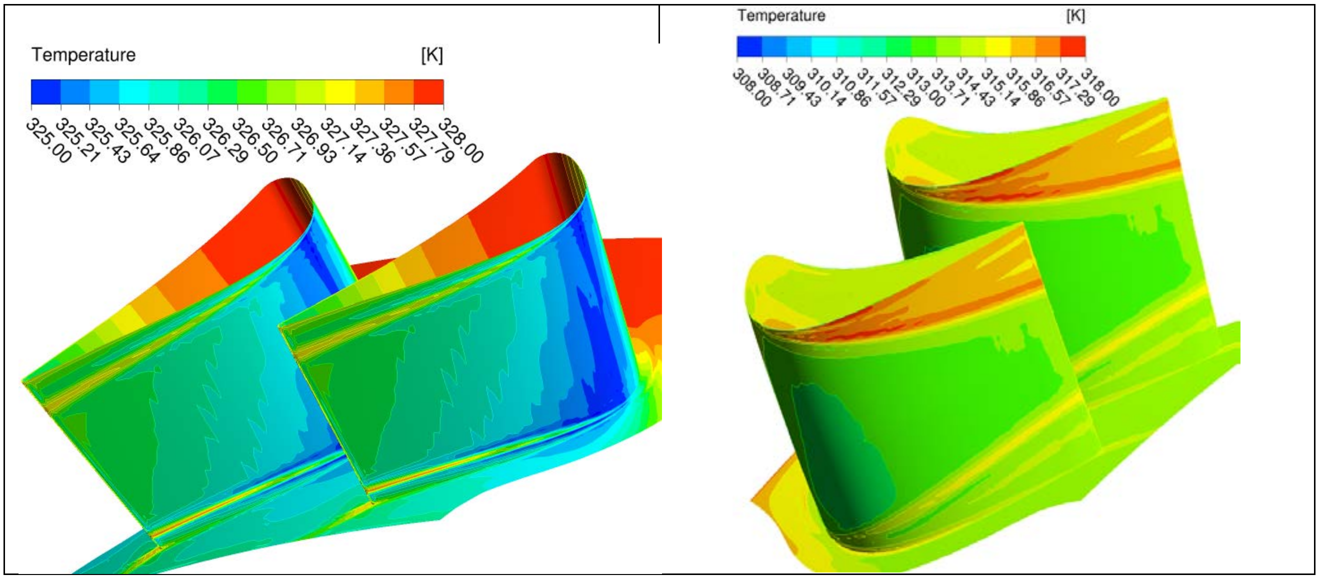

Figure 5.12: Metal temperature contours in the stator and in the rotor rows.

From the contours of static temperature of last figure, one can distinguish on the blade suction surfaces traces with higher temperature. Those are generated by the heat dissipated from the passage vortices and the OTL vortex, in the case of the rotor, to the metal. It is noticeable how the passage vortices lift off the end walls by the time they reach the trailing edge of the blades, as mentioned in section 2.1.

Contours of static pressure computed at the end wall of the rotor in Figure 5.13 show that in the clearance of the rotor blades a strong pressure gradient exists at each side of the blade, in particular close to the trailing edge. This pressure difference sets the movement of the fluid in the clearance from the pressure side of the rotor blade to the suction side. Therefore the over the tip leakage flow is a pressure driven process.

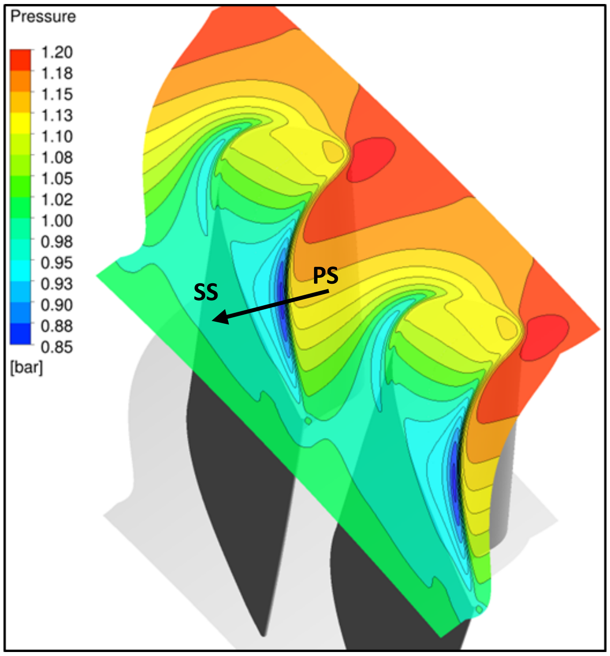

Figure 5.13: Computed static pressure contours at the rotor casing end wall

The recirculating fluid trapped in the separation bubble located at the rotor blade tip corner in the pressure side was captured in the numerical simulation as seen in Figure 5.14 (top view) and mentioned back in section 2.2 and also illustrated in Figure 2.9. This phenomenon was also captured in the turbine test stand as the visualization of oil deposits on the rotor blade tip confirm in Figure 5.14 (bottom view). With the life time of the turbine the edges of the blades round-off because of wear and tear and this occurrence disappears.

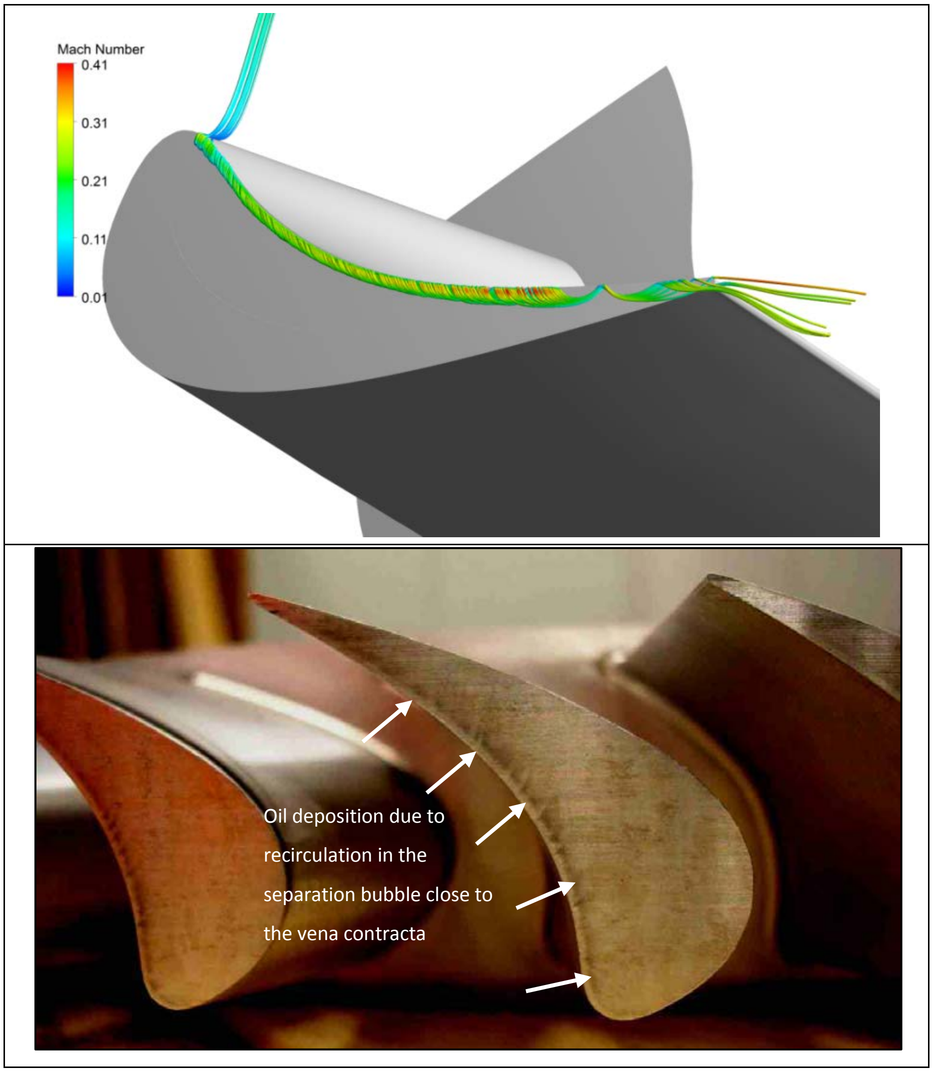

Oil deposition due to recirculation in the separation bubble close to the vena contracta

Figure 5.14: Computed streamlines (above) and flow visualization (below) [16] of the recirculation bubble over the rotor tip surface

In Figure 5.15 computed axial velocity contours at a rotor plane cut near the blade trailing edge are presented. The high velocity levels of the flow in the clearance can be appreciated. Maximum velocity is reached above the separation bubble, the location of the vena contracta. On the pressure side of the rotor there is a region near the end wall and blade tip corner with a momentum deficit which is the location where the OTL rolls up into a vortex as depicted in Figure 5.16.

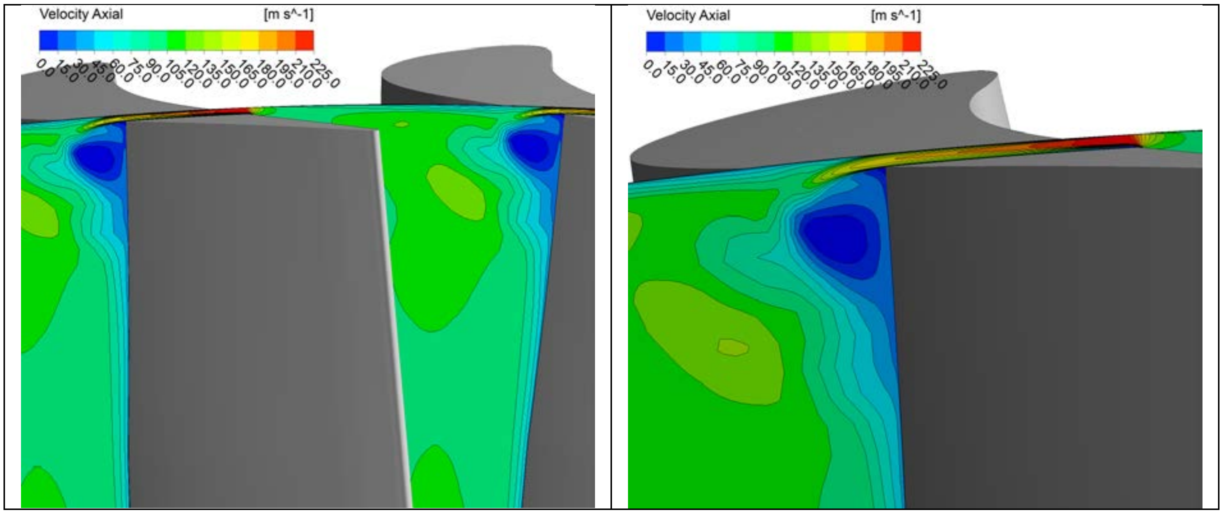

Figure 5.15: Over the tip leakage flow contours of axial velocity

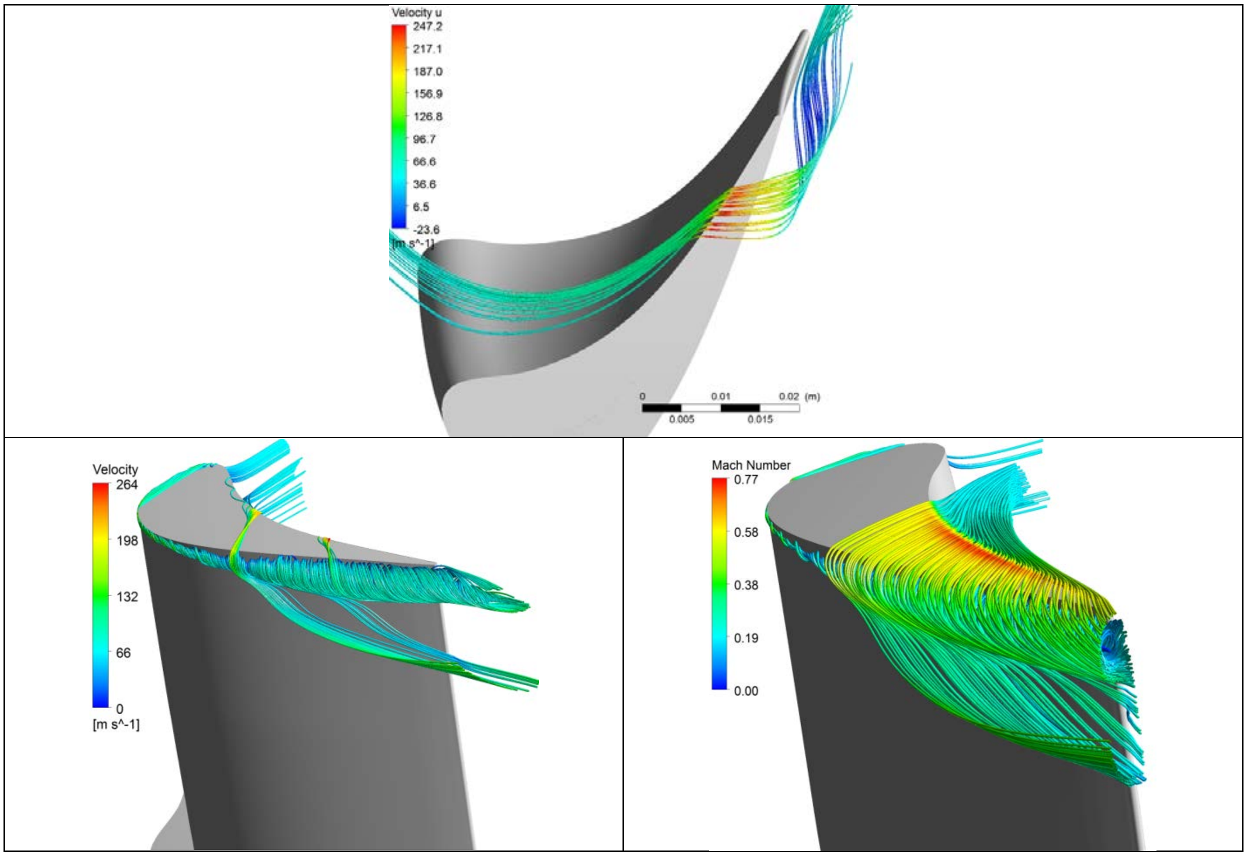

Figure 5.16: Computed streamlines of velocity showing the OTL flow roll into a vortex

Axial velocity contours at the exit of the rotor row are shown in Figure 5.17. As depicted here the fluid from the rotor clearance retains high levels of kinetic energy. This flow is passed to the downstream row (diffuser) in the form of wall jets.

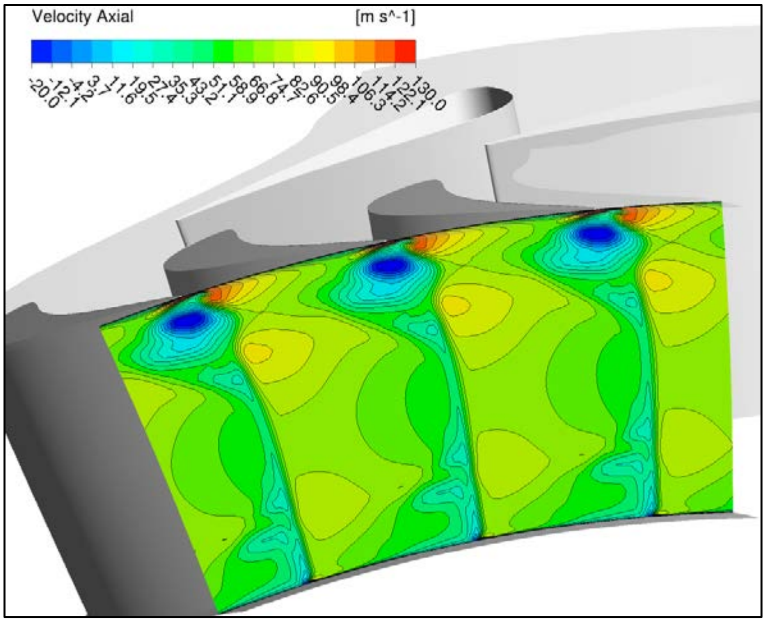

Figure 5.17: Computed axial velocity contours at the exit of the rotor

Lastly, when the turbine chokes (see performance map in Figure 5.2), the only mechanism to decrease the pressure is through a series of expansions waves. Plus oblique shocks form at the trailing edge of the blade as seen from rotor blade to blade contours of Mach number and pressure of Figure 5.18. Because of their shape these are called fish tail shocks.

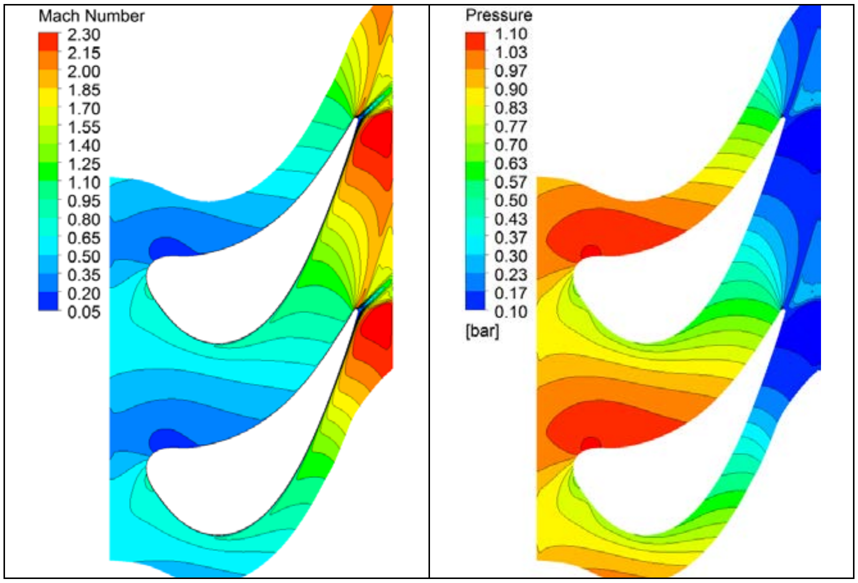

Figure 5.18: Mach number and pressure contours at mid-span plane of the rotor showing fish tail shocks

5.2 Grid independence study

It is helpful to quantify the error that one can make during numerical computations. One such means to achieve that is by refining the grid of the computational domain until one reaches a unique solution. While this method is time wise very prohibitive to be of practical economical interest in the industry, it is still very popularly used in an academic environment. Of course in the end the investigator has to make a trade-off between accuracy and time, and computing resources consumption.

Since most of the present investigation deals with the mixing plane algorithm between stage rows, as seen in Figure 5.19, only this interface method will be assessed in the grid independence study.

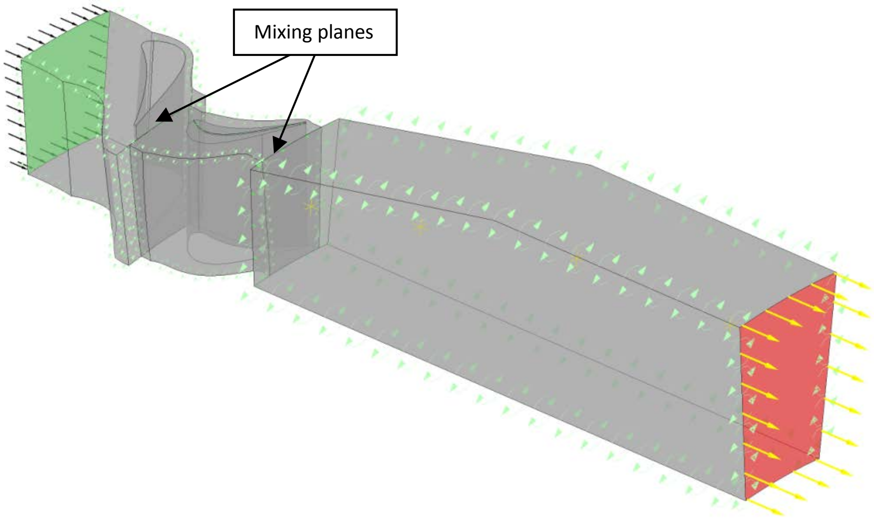

Figure 5.19: 3D model of the turbine stage with the exhaust diffuser

In Table 5.1 the number of grid nodes per row utilized for the two cases considered is shown. One can see that Grid 2 contains from two to three times as many nodes than Grid 1. However most of the grid nodes have been clustered around the boundary layers (blades, blade tips, hub, shroud) because of the high flow gradients present in those regions.

While the number of nodes from one grid to the other has more than doubled, the time required to obtain a converged solution grows almost exponentially with the increase of the number of nodes. The computing resources (disk space and memory allocated) needed, have also a significant impact from using Grid 2.

Table 5.1: Comparison of the number of grid nodes used at each turbine-diffuser row for the two grids

	Number of Computational Nodes	
	Grid 1	**Grid 2**
Stator	407,133	1,318,518
Rotor	401,825	1,823,108
Diffuser	218,940	494,190

Because this investigation's main goal is to evaluate the performance of the diffuser, it is useful to compare the pressure recovery and total pressure loss coefficients obtained with both grids. It is also important to compare those same parameters for the stator and rotor of the turbine stage separately, since the inlet conditions to the diffuser are given by the preceding turbine stage. These coefficients are calculated according to the following equations for the turbine and diffuser respectively:

1) The static pressure coefficient for a turbine is defined as:

$$Cp_{turb} = \frac{p_{in} - p_{out}}{p_{t,in} - p_{out}} \qquad (5.8)$$

2) The total pressure loss coefficient for a turbine is defined as:

$$Cp_{t,turb} = \frac{p_{t,in} - p_{t,out}}{p_{t,in} - p_{out}} \qquad (5.9)$$

3) The static pressure recovery coefficient for a diffuser is as:

$$Cp_{diff} = \frac{p_{out} - p_{in}}{p_{t,in} - p_{in}} \qquad (5.10)$$

4) The total pressure loss coefficient in diffusers follows:

$$Cp_{t,diff} = \frac{p_{t,in} - p_{t,out}}{p_{t,in} - p_{in}} \qquad (5.11)$$

In Table 5.2 the comparison of the pressure loss and the static pressure coefficients of all turbine rows using both grids is given. Plus the error of the coarser grid (Grid 1) relative the denser grid (Grid 2) is pointed out.

Table 5.2: Comparison of the turbine-diffuser rows losses and performances for two grids

	Grid 1		**Grid 2**		**Error [%]**	
	Cp	**Cp_t**	**Cp**	**Cp_t**	**Cp**	**Cp_t**
Stator	0.927	0.050	0.928	0.047	0.1	-6.7
Rotor	1.112	0.162	1.110	0.157	-0.1	-3.3
Diffuser	0.358	0.045	0.366	0.050	2.0	9.2

As one can see from the previous table, the static pressure coefficient for the stator and the rotor show similar values with a deviation of only 0.1 %. The diffuser presents a higher deviation of 2.0 %. The total pressure loss coefficient has a bigger deviation in all rows showing a maximum in the diffuser of 9.2 %.

Since in this study a fluid jet close to the wall is investigated, it is of paramount importance to have a good resolution of the boundary layers so to achieve an optimal performance of the turbulent model. One common practice to judge the quality of boundary layers is in terms of the non-dimensional wall distance y_+ that follows the *law of the wall* given by:

$$y_+ = \frac{y \cdot u_*}{\nu} \tag{5.12}$$

Where the *friction velocity* u_* is given as:

$$u_* = \sqrt{\frac{\tau_0}{\rho}} \tag{5.13}$$

τ_0 is the shear stress at the wall, ν is the kinematic viscosity of the fluid, and y_+ represents the distance to the solid walls nondimensionalized by the viscous scale u_*/ν . Following the law of the wall, different regions next to the wall are identified, as shown in Figure 5.20, according to whether or not fluid viscous effects are dominant. Therefore when $y_+ < 50$, viscous effects contributions to the shear stresses are significant and above can be neglected.

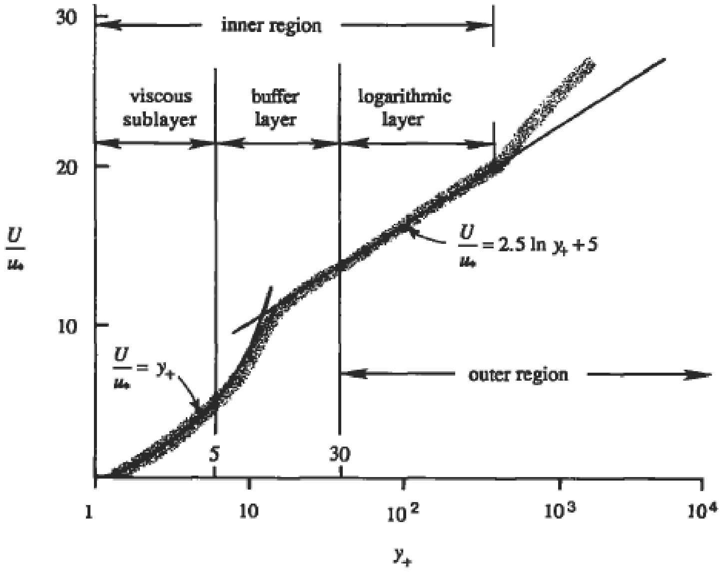

Figure 5.20: Law of the wall in turbulent flows [31]

In Table 5.3 is collected the values of y_+ obtained using both grids at the walls of the different turbine-diffuser stage rows. The y_+ values obtained with both grids are well within good accuracy of the turbulent *k-ω SST* model chosen [29].

Table 5.3: Computed Y+ values at the walls of the turbine stage-diffuser rows for the two grids

		Grid 1	**Grid 2**
Stator	**Hub**	13.881	1.194
	Casing	13.592	1.166
	Blade	10.583	12.037
Rotor	**Hub**	11.841	1.164
	Casing	8.718	1.244
	Blade	7.843	8.310
Diffuser	**Hub**	7.850	3.054
	Casing	2.511	0.568

5.3 Effect of the rotor tip clearance flow on diffuser performance

In this study, the performance of the diffuser is analyzed comparing its static pressure recovery and total pressure loss coefficients. For that, the external opening angle of the diffuser is increased in steps of 2° to 4°. The exhaust diffuser performance is then recorded and compared. Two turbine-diffuser stage configurations are utilized: one with a shrouded and one with an unshrouded rotor, so that the effect of the over the tip leakage flow on the performance of the diffuser is isolated.

The two turbine-diffuser stage configurations used in this analysis are shown in Figure 5.21 below. To the left is the computational domain with the unshrouded rotor and to the right the domain with the shrouded one.

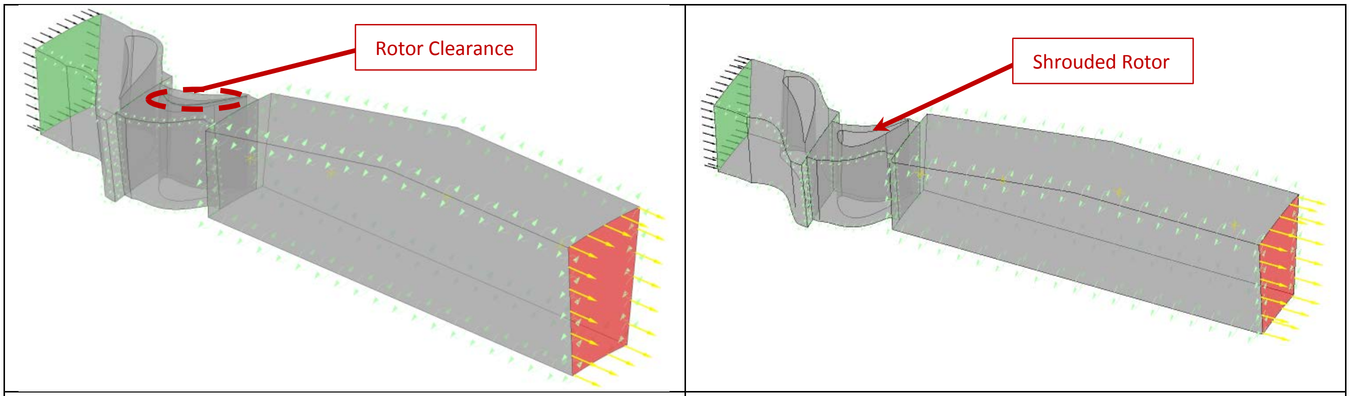

1) **Diffuser with an unshrouded Rotor Stage**

2) **Diffuser with a shrouded Rotor Stage**

Figure 5.21: Turbine-diffuser stage configurations with unshrouded and shrouded rotors

5.3.1 *Diffuser coupled to a shrouded turbine rotor stage*

Because the *mixing plane* is chosen as the interstage algorithm between the stationary and the rotating parts, the inlet conditions to the diffuser are the circumferentially averaged fluxes coming from the rotor row. In Figure 5.22 below one can see an example of how the axial velocity and entropy as they come out of the rotor are redistributed pitchwise as they are passed to the diffuser.

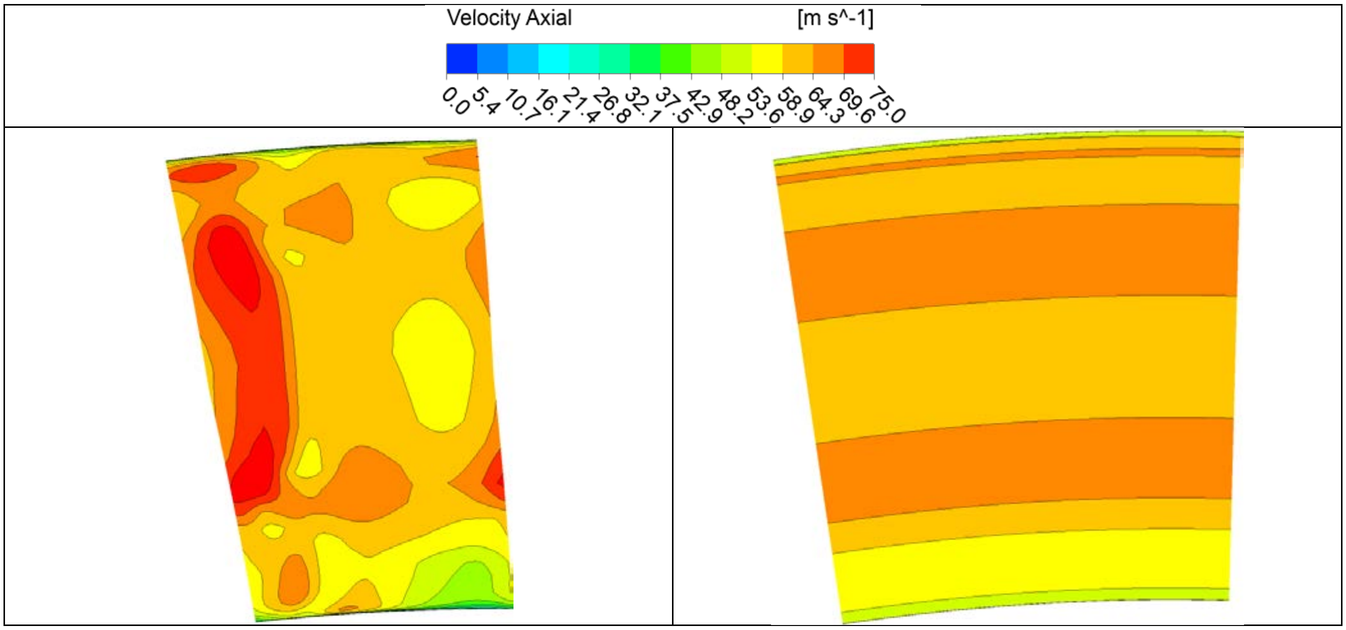

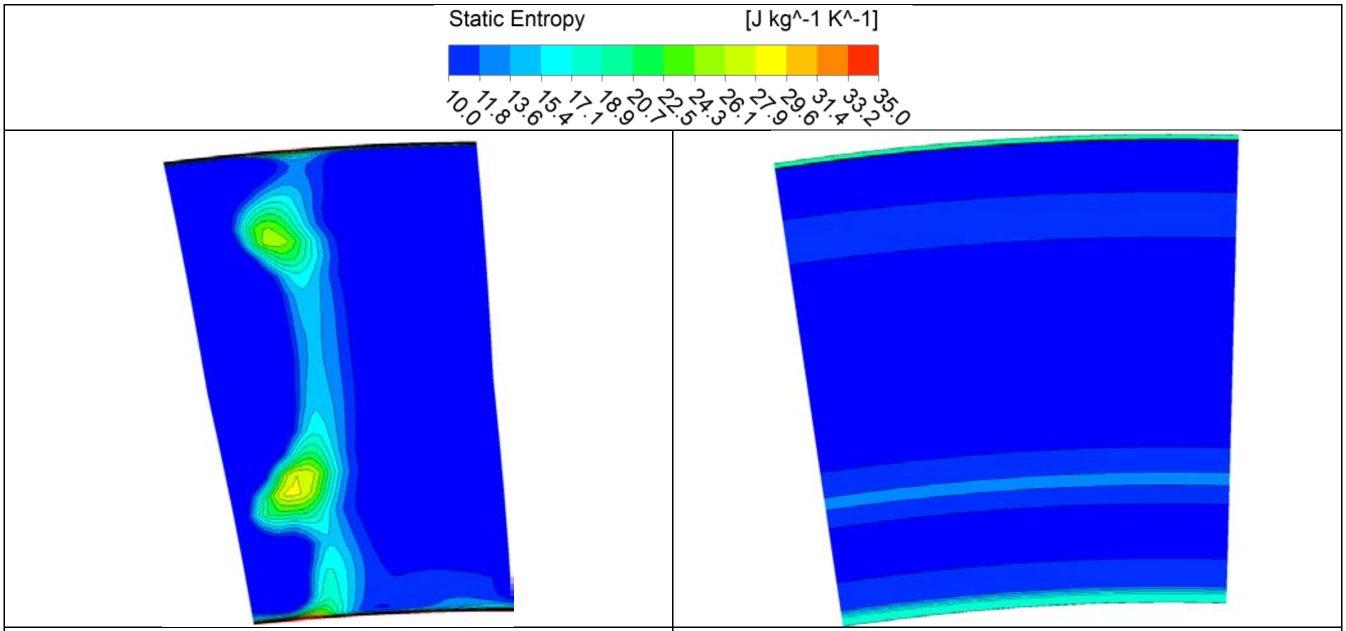

1) Contours before the mixing plane (exit rotor) | **2) Contours after the mixing plane (inlet diffuser)**

Figure 5.22: Axial velocity and entropy contours at the shrouded rotor exit plane and how they are mixed at the diffuser inlet plane

The computed contours of axial velocity at the mid-line of the diffuser, for several opening angles, are shown in Figure 5.23 below. As one can notice, the axial velocity is relatively well distributed at the inlet of the diffuser. That is, no large velocity gradients exist.

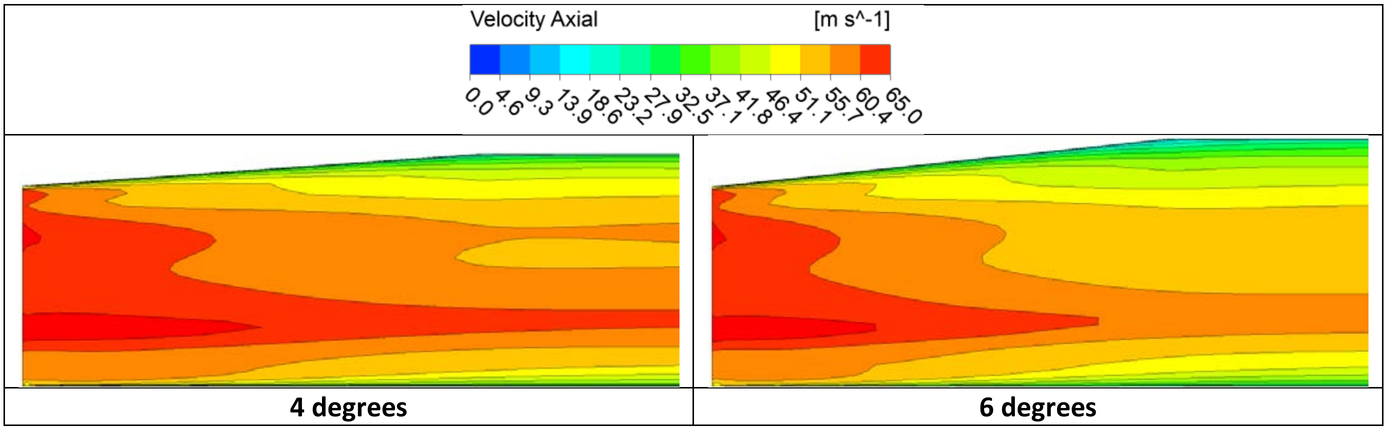

4 degrees | **6 degrees**

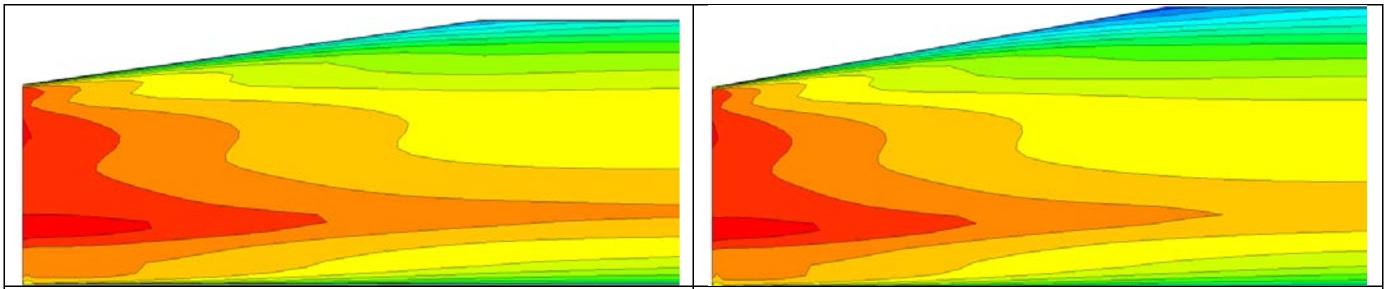

8 degrees **10 degrees**

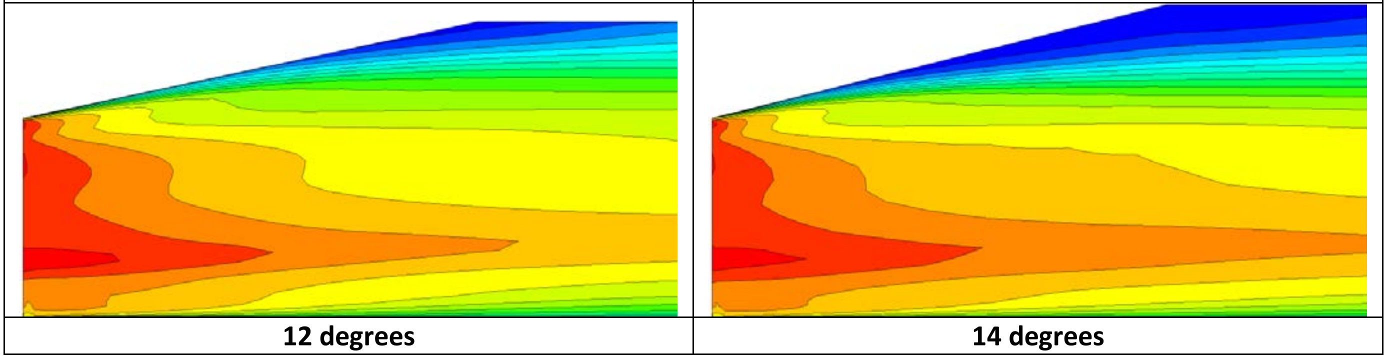

12 degrees **14 degrees**

Figure 5.23: Computed contours of axial velocity in the diffuser coupled to the shrouded turbine at several opening angles

As Figure 5.23 reveals, a deceleration of the fluid takes place from diffuser inlet to diffuser outlet, a clear sign that the static pressure is increasing. However the fluid starts to loose rapidly kinetic energy near the upper wall, particularly in the vicinity of the diffuser corner junction to the straight pipe. This trend is clearly seen as early as for an 8° opening angle. In fact, reverse flow regions develop in this section when the diffusing angle is increased to 12° and beyond. At the boundary layers the fluid has a momentum deficit due to friction with the walls. When the flow is not able to sustain the adverse pressure gradient, these boundary layers are more prone to fluid separation and detachment from the walls, reducing thus the effective area ratio of the diffuser and consequently decreasing its intended overall performance. The performance of the diffuser in terms of static pressure recovery coefficient is displayed in Figure 5.28 for several opening angles.

If one could re-energize these boundary layers, by means of fluid injection at the wall for example, so as to avoid early flow separation, then the diffuser could be able to sustain a larger adverse pressure gradient, improving its static pressure recovery and consequently enhancing its overall performance.

In Figure 5.24, one can observe that for the configurations with diffuser angles of 12° and 14°, regions of diffuser blocked volume due to reverse flow that do not contribute to pressure recovery appear. The diffuser simply stalls.

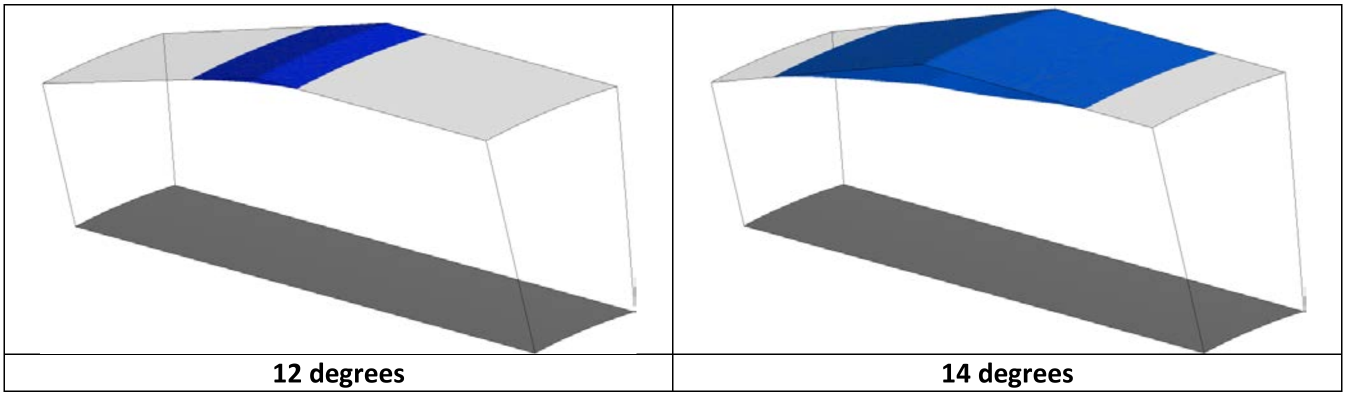

12 degrees **14 degrees**

Figure 5.24: Computed regions of reverse flow in diffuser coupled to a shrouded rotor

5.3.2 *Diffuser coupled to an unshrouded turbine rotor stage*

In a similar manner as in the precedent case, the inlet conditions to the diffuser are the circumferentially averaged fluxes from the rotor row, because of the *mixing plane* algorithm. Figure 5.25 shows an example of how the axial velocity and entropy are circumferentially mixed out at the inlet of the diffuser.

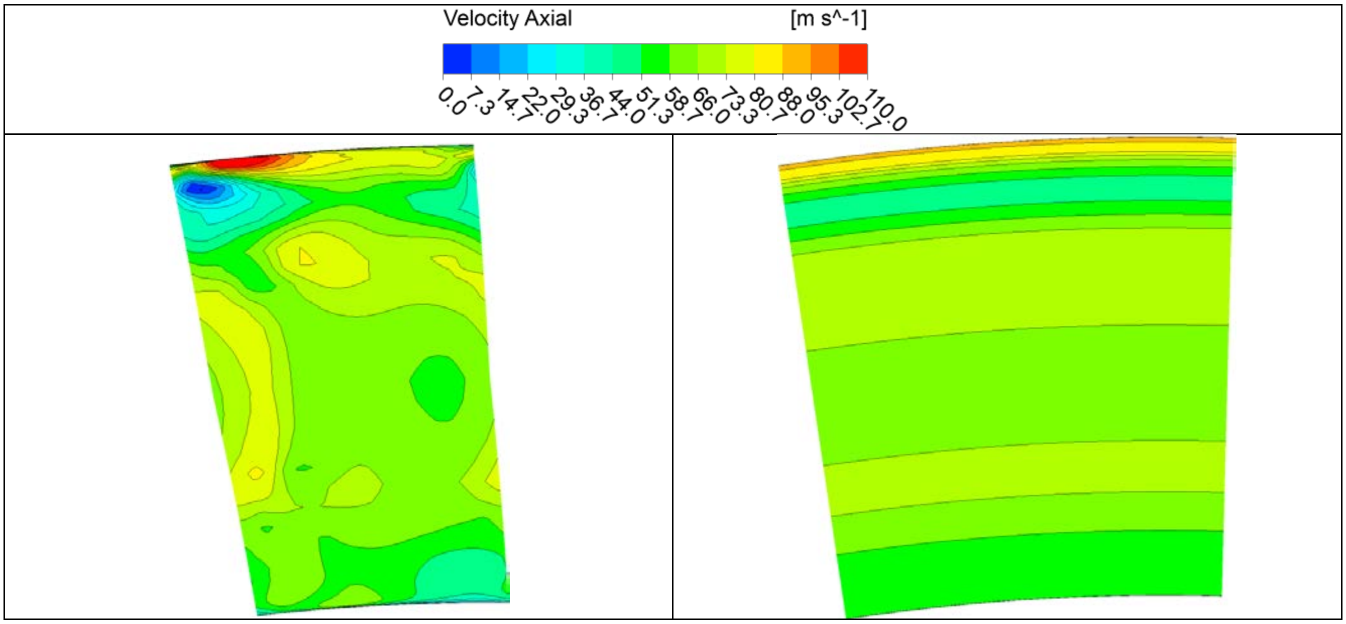

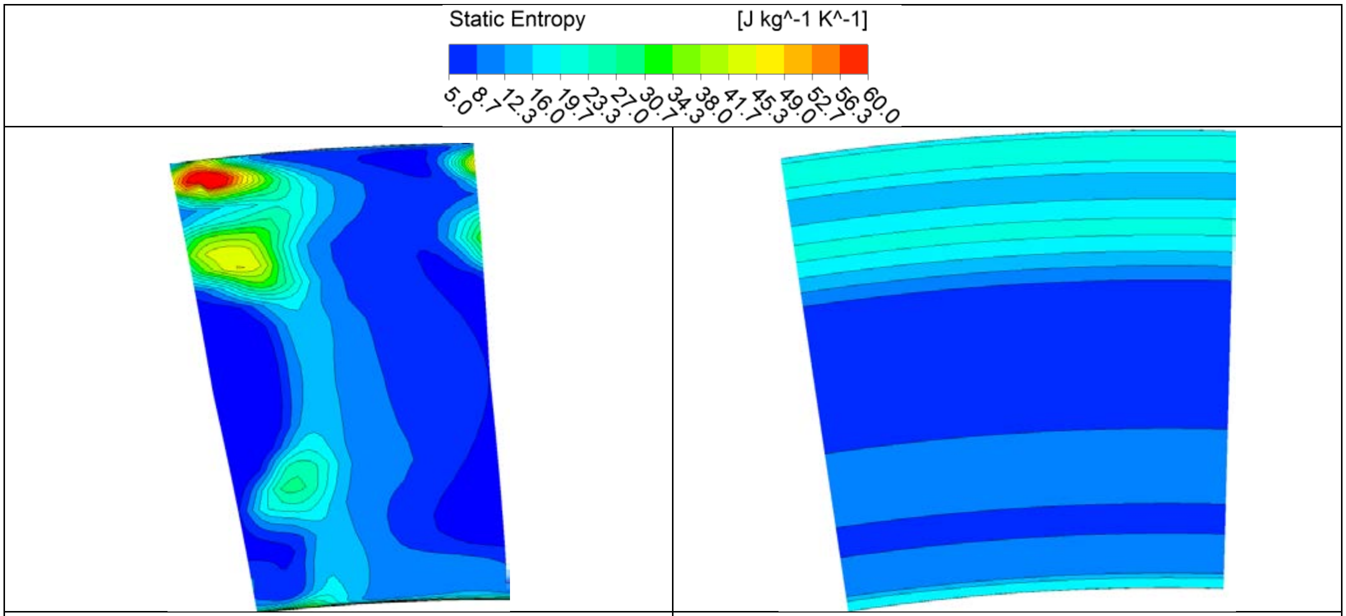

1) Contours before the mixing plane (exit rotor)

2) Contours after the mixing plane (inlet diffuser)

Figure 5.25: Axial velocity and entropy contours at the unshrouded rotor exit plane and how they are mixed at the diffuser inlet plane

A quick observation to the axial velocity flow field coming out of the unshrouded rotor (top left of Figure 5.25) evidences a small region containing high velocity flow that is found at the upper wall, between the rotor blade and the casing, and is transferred to the diffuser: a wall jet.

Computed contours of axial velocity at the mid-line of the diffuser for several opening angles are shown in Figure 5.26. The wall jet created from the turbine rotor tip leakage flow is clearly seen, located in the upper wall region of the diffuser.

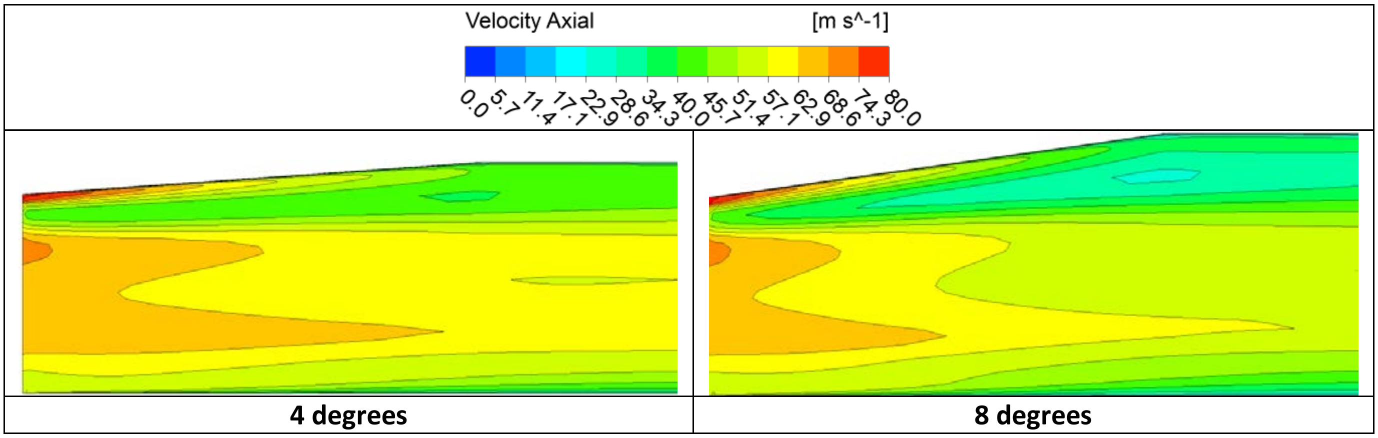

4 degrees

8 degrees

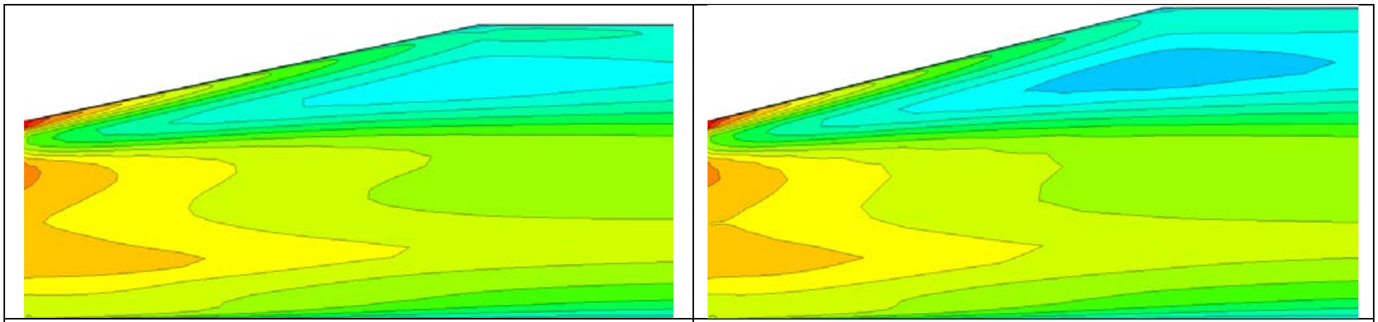

12 degrees **14 degrees**

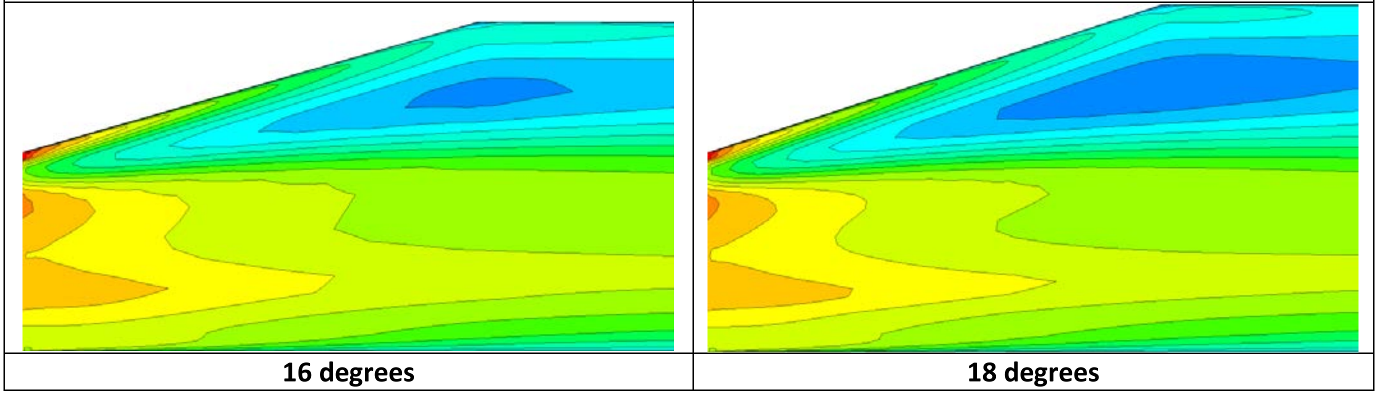

16 degrees **18 degrees**

Figure 5.26: Computed contours of axial velocity in the diffuser coupled to the unshrouded turbine at several opening angles

From Figure 5.26 one can appreciate the large velocity gradients between the jet and the main passage flow but above all between the jet and the diffuser upper wall boundary layer flow. In this occurrence, near the upper wall there is no sign of having a fluid with momentum deficit as seen in the previous case. Indeed, in this occasion the wall jet has energized the low momentum fluid at the upper boundary layer. As a consequence, the diffuser can tolerate larger diffusing angles without stalling. Truly, as the opening angles are increased, the wall jet loses intensity faster due to larger pressure gradients and a mixing process, but the fluid remains attached to the upper wall surface of the diffuser. Hence, the diffuser recovers more static pressure.

Moreover, both, the wall jet that emanates from the rotor tip clearance and the core passage flow are not swirl free. While the core of the flow from the main passage is turned by the turbine rotor in its process from work extraction, the fluid that is leaked between the rotor tip and the casing is left undisturbed. Therefore the two distinct flows emerging from the turbine rotor row will have two well defined swirling angles. This fact can be depicted in Figure 5.27, where computed contours of swirl inside the diffuser at the mid-line are shown.

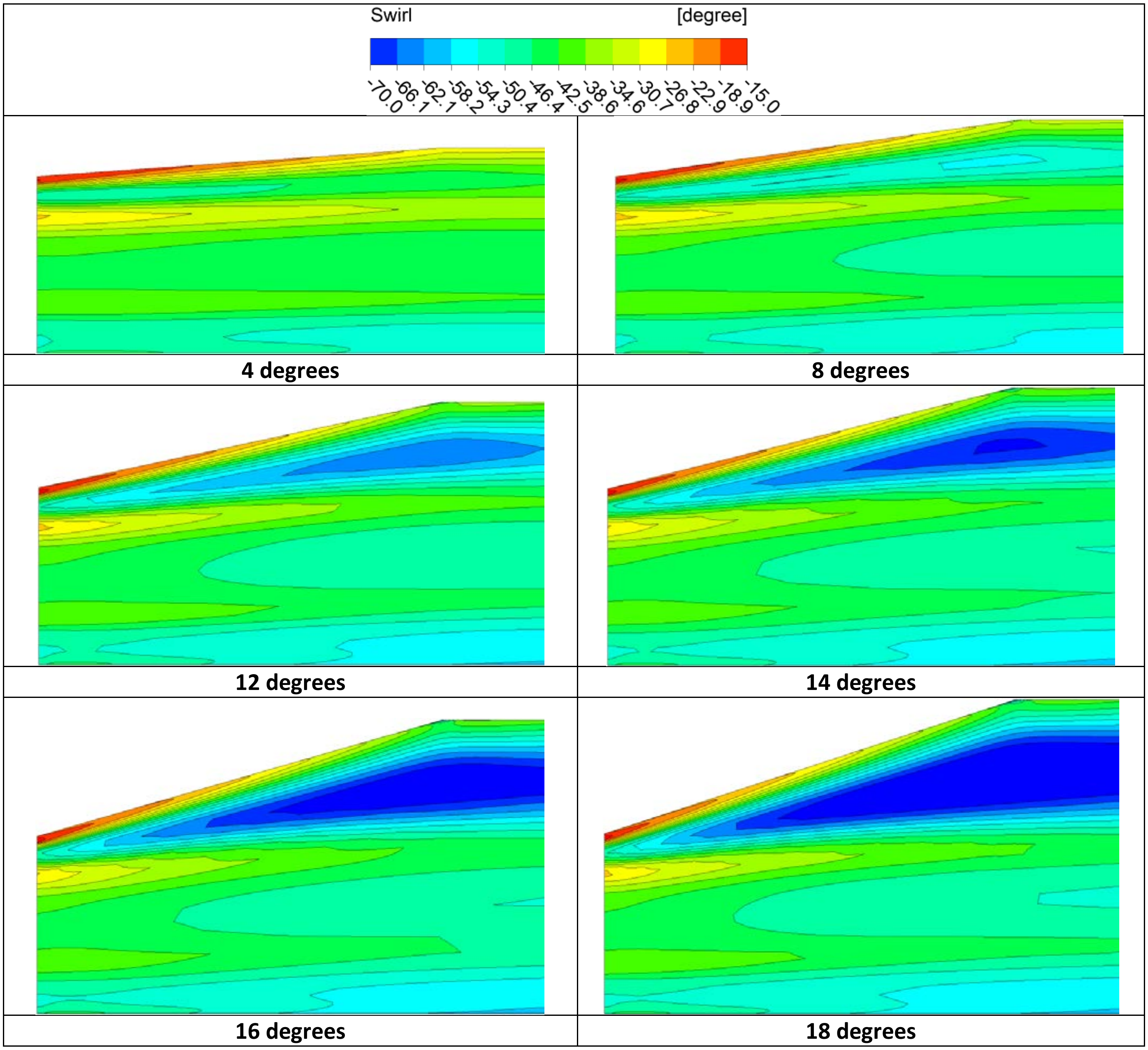

4 degrees

8 degrees

12 degrees

14 degrees

16 degrees

18 degrees

Figure 5.27: Contours of swirl in the diffuser with an unshrouded rotor at various opening angles

As observed in Figure 5.27, high gradients of swirl also exist between the wall jet and the core passage flow. For this specific turbine operation, both, the averaged core passage and the averaged over the tip leakage flows are counter-swirling, but at very different angle rates. This gives rise to a vortex sheet with streamwise vorticity that separates the core flow of the rotor passage channel and the over the tip leakage flow, as mentioned in section 2.6.2. As a mixing process within the diffuser takes place the intensity of the swirl decays.

When evaluating the static pressure recovery and the total pressure loss coefficients it is important to mention the numerical methodology utilized. These values are obtained from the static and total pressures between the diffuser inlet and outlet planes as stated in equations 5.10 and 5.11. Since the inlet and outlet diffuser planes do not have uniform flow boundary conditions as seen in Figure 5.22 and Figure 5.25, it is necessary to average these values. According to Cumpsty & Horlock [32] a way to average non-uniform flow state variables, so that they represent most closely the actual observations, is by mass flow averaging when the kinetic energy of the fluid is involved and area averaging when it is not. Therefore, the static quantities are area averaged and the total ones mass flow averaged.

In Figure 5.28 and Figure 5.29 are compared the static pressure recovery and total pressure loss coefficients respectively for both turbine-diffuser configurations. From Figure 5.28 the static pressure recovery for diffuser opening angles less than 12° is around 10% better in the diffuser with the unshrouded rotor configuration. While the diffuser with the shrouded rotor configuration stalls above angles of 12°, the presence of the wall jet in the other diffuser allows for higher opening angles without stalling.

As observed from Figure 5.29, the total pressure loss coefficient shows a “bucket” shaped curve for which an optimal diffuser angle, that is with minimum losses exist. Even though the diffuser with the wall jet recovers more static pressure, it also produces more losses. This is due to the particular flow features that enter the diffuser. Losses in the diffuser not only come from the friction of the fluid against the walls but also due to mixing mechanisms that take place between the core fluid and the jet stream which vary not only in magnitude but also in direction (swirl). Plus the jet stream has high velocity gradients near the wall which give rise to higher stresses on the wall. This element alone produces already more losses than in the case without the wall jet.

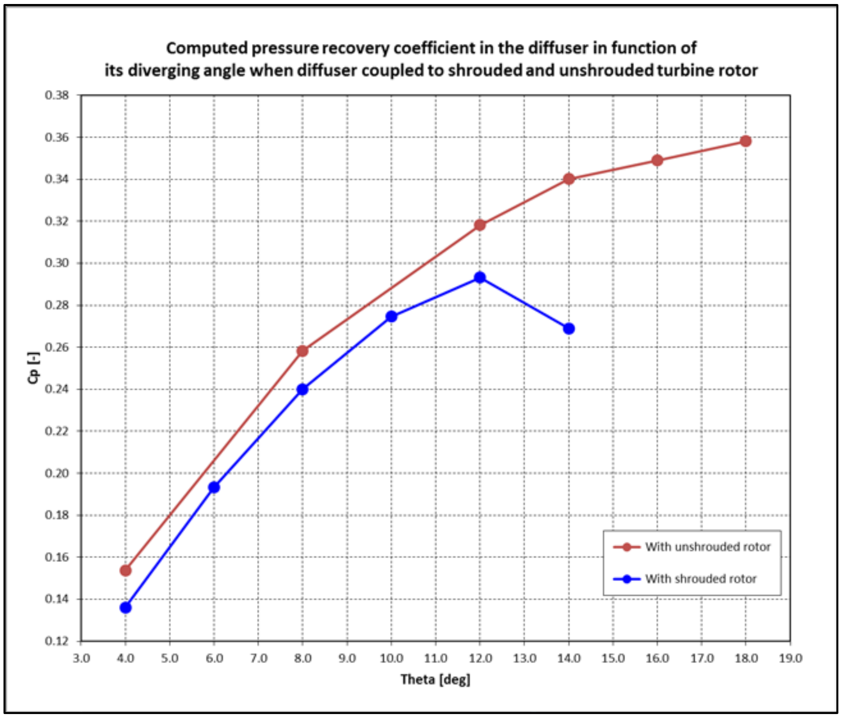

Figure 5.28: Computed diffuser static pressure recovery coefficient in function of its opening angle

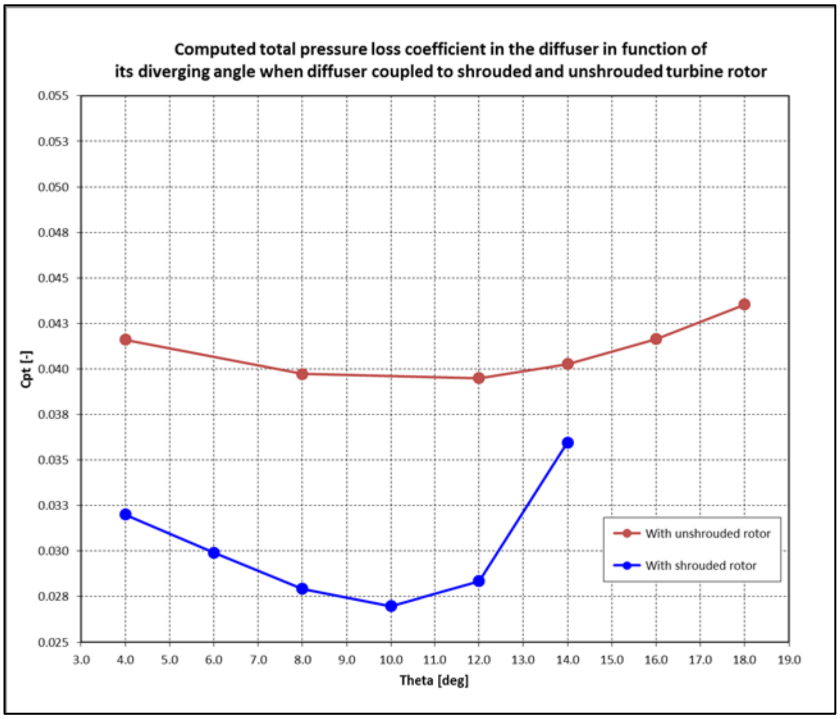

Figure 5.29: Computed diffuser total pressure coefficient loss at several diverging angles

5.4 Influence of the rotor exit flow angle on diffuser performance

The turbine stage used in this numerical simulation is a high pressure and of high load type, which is mainly utilized in the aerospace industry. This means that more work is extracted from the turbine per stage than in a conventional one. Consequently overall engine space and weight is reduced, which is very attractive when these parameters are important design goals.

Designing turbine stages with interstage counter swirl is used in order to increase the loading coefficient of reaction stages [33]. Increasing the loading of the stages increases the blade turning which increases also the blade row loss coefficient that in the end is reflected in the stage efficiency as seen in Figure 5.30.

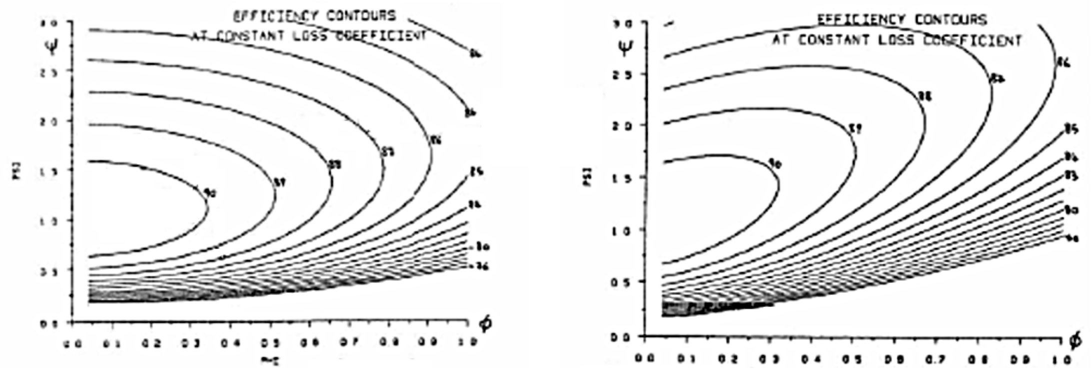

Figure 5.30: Efficiency contours for stages with a constant loss coefficient of 0.1 [33]

On left stages with 0^o interstage swirl. *On right stages with -45^o interstage swirl*

In this study, the variation of the flow exit angle α_3 is achieved by keeping the mass flow constant and by adjusting the rotational speed of the turbine rotor. In doing so, care has to be taken in not to set the speed of the turbine to an off-design operation. When this happens, regions of flow separation in the rotor will appear because of the flow incidence angle to the rotor blade is beyond the allowable limits.

The absolute swirl flow angle α_3 at the exit of the rotor (inlet diffuser) is defined as:

$$\alpha_3 = \arctan\left(\frac{v_\theta}{v_x}\right) \qquad (5.14)$$

For this analysis, as with in the previous case studied, both turbine configurations, that is with a shrouded and an unshrouded rotor, as depicted back in Figure 5.21, are used. The absolute flow swirl is mass flow averaged, following Cumpsty & Denton [32] as mentioned previously.

5.4.1 Diffuser coupled to the shrouded rotor

In Figure 5.31 is represented the static pressure recovery coefficient in the diffuser in function of the averaged inlet swirl for several opening angles of the diffuser.

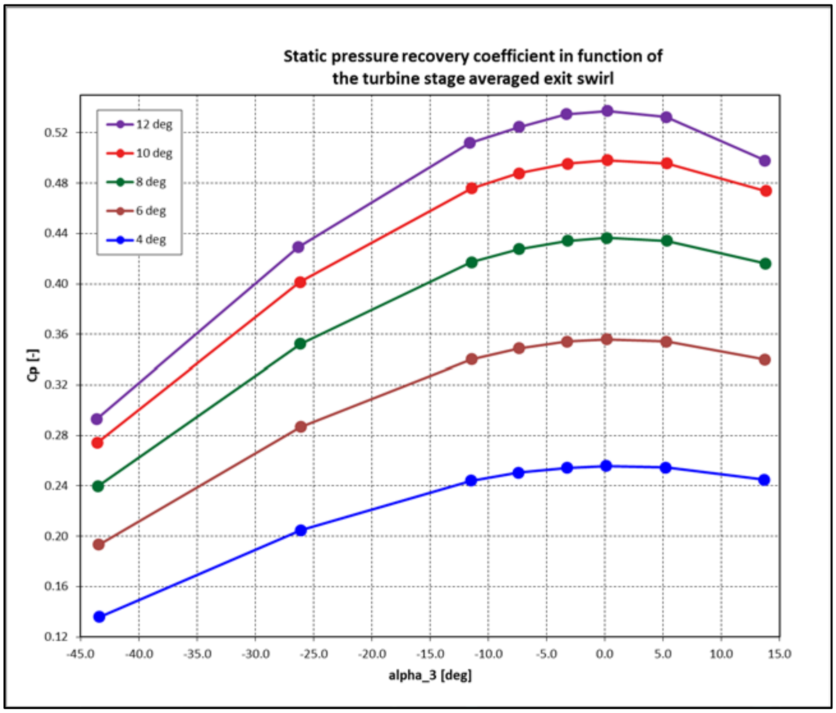

Figure 5.31: Diffuser Cp at different opening angles in function of the shrouded rotor flow exit angle

Except for the localized two rotor passage vortices generated, the swirl coming out of the shrouded rotor is pretty much uniform at the exit of the rotor stage row.

Figure 5.31 shows that by reducing the inlet swirl to the diffuser more static pressure can be recovered. The maximum static pressure gain corresponds to an inlet swirl angle of 0° (swirl-free) and that for all opening angles of the diffuser. Moreover it is shown that the Cp is independent on whether the flow is co or counter swirling since the diffuser recovers the same amount of pressure at each side of the swirl-free flow. That is the Cp curves shown in Figure 5.31 are symmetrical about the 0° inlet flow swirl angle. And that is true at all diffuser opening angles studied.

The total pressure loss coefficients in function of the inlet flow swirl are depicted in Figure 5.32. These are also "bucket" shaped curves. That is, at each diffuser opening angle there is an optimum inlet flow swirl for which the losses are minimized.

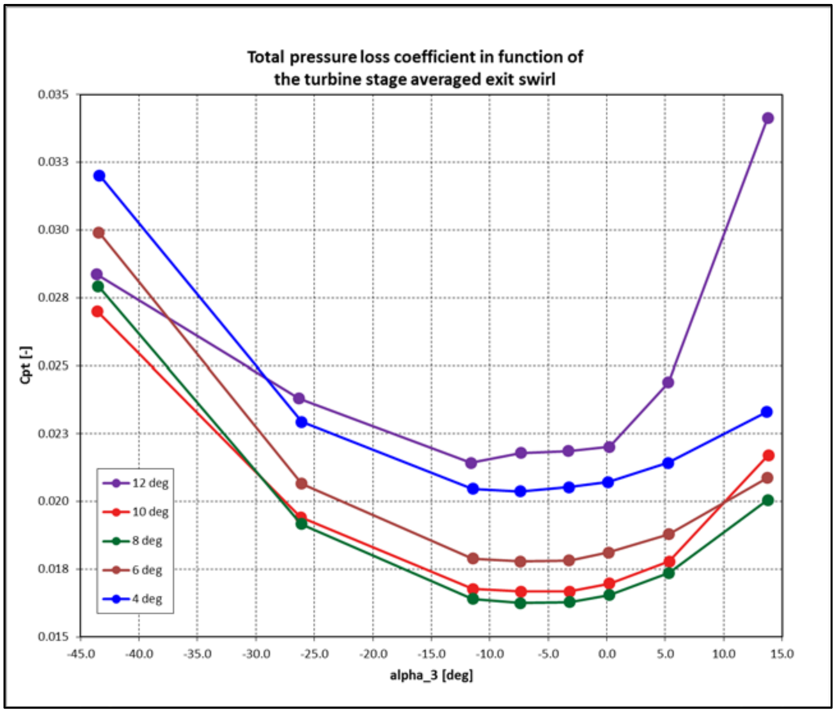

Figure 5.32: Diffuser Cp_t at different opening angles in function of the shrouded rotor flow exit angle

As one can observe in Figure 5.32, the Cp_t is not independent of the inlet swirl angle. Indeed the curves are not symmetrical around $\alpha_3 = 0.0°$.This is most probably due to the fact that the preceding turbine stage is not working at its optimum conditions, since its design is around $\alpha_3 = -40.0°$. Indeed, the losses generated in the stator and rotor blades are transferred to the diffuser. For this study, the rotor is most sensitive, in terms of loss generation, to variations in flow incidence angle.

5.4.2 *Diffuser coupled to the unshrouded rotor:*

In a similar way as in the preceding case, Figure 5.33 shows the static pressure recovery coefficient in the diffuser coupled to an unshrouded turbine rotor in function of the averaged inlet swirl for several opening angles of the diffuser.

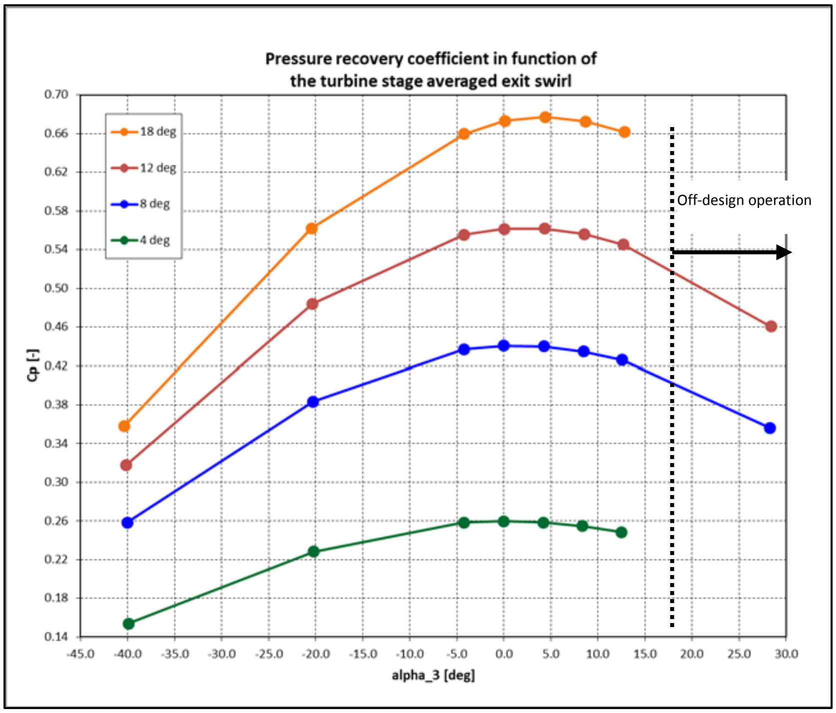

Figure 5.33: Diffuser Cp at different opening angles in function of the unshrouded rotor flow exit angle

Contrary to the preceding case, here the inlet flow field cannot be considered as uniform in terms of flow swirl due to the over the tip leakage flow. Therefore two fluid streams are differentiated: the core fluid from the rotor passage and the fluid coming from the clearance, as already mentioned in section 5.3.2 and depicted in Figure 5.26 and Figure 5.27.

Figure 5.33 evidences that the pressure recovered by the diffuser is optimized when a slight inlet averaged flow co-swirl occurs. This trend is more pronounced for higher diffuser diverging angles such as 12^{o} and 18^{o}. In this graph, a turbine off-design limit has also been drawn. This limit is based on the observation of flow separation from the surface of the turbine rotor blade.

The total pressure loss coefficients in function of the inlet flow swirl are given in Figure 5.34. Firstly, if one would compare this graph with the one shown back in Figure 5.32, one would notice that, for the same diffuser opening angle more losses are generated in this case due to higher mixing losses as discussed previously (section 5.3.2). Secondly, contrarily to the previous case where losses where optimized with a slight counter-swirl inlet flow angle (between -8^o and -3^o), here losses are at their minimum for a slight co-swirl inlet flow angle (between 0^o and $+5^o$).

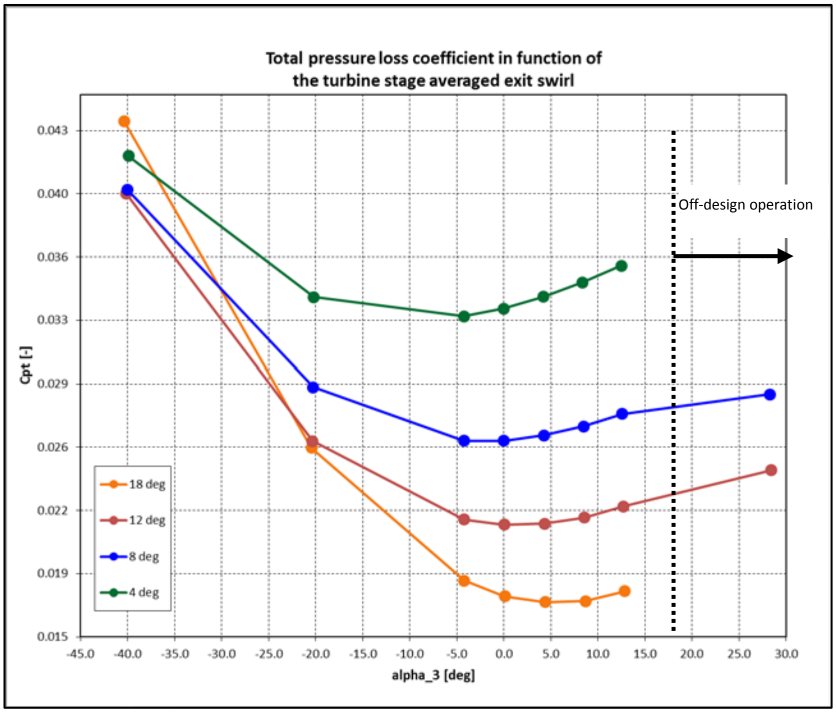

Figure 5.34: Diffuser Cp_t at different opening angles in function of the unshrouded rotor flow exit angle

As an example, in Figure 5.35 one can observe streamlines of velocity for the core passage and the over the tip leakage flows. The flow from the clearance of the rotor emerges at an angle of $\alpha_3 = 13.3^o$ (co-swirl direction) whereas the flow that contributed to the power output of the turbine, that is the core flow, emerges at an angle of $\alpha_3 = -9.2^o$ (counter-swirl direction). If one would mass flow average the entire rotor exit plane, consequently combining both, core and tip leakage, contributions, one would find that the flow angle is at $\alpha_3 = -4.2^o$ (counter-swirl direction).

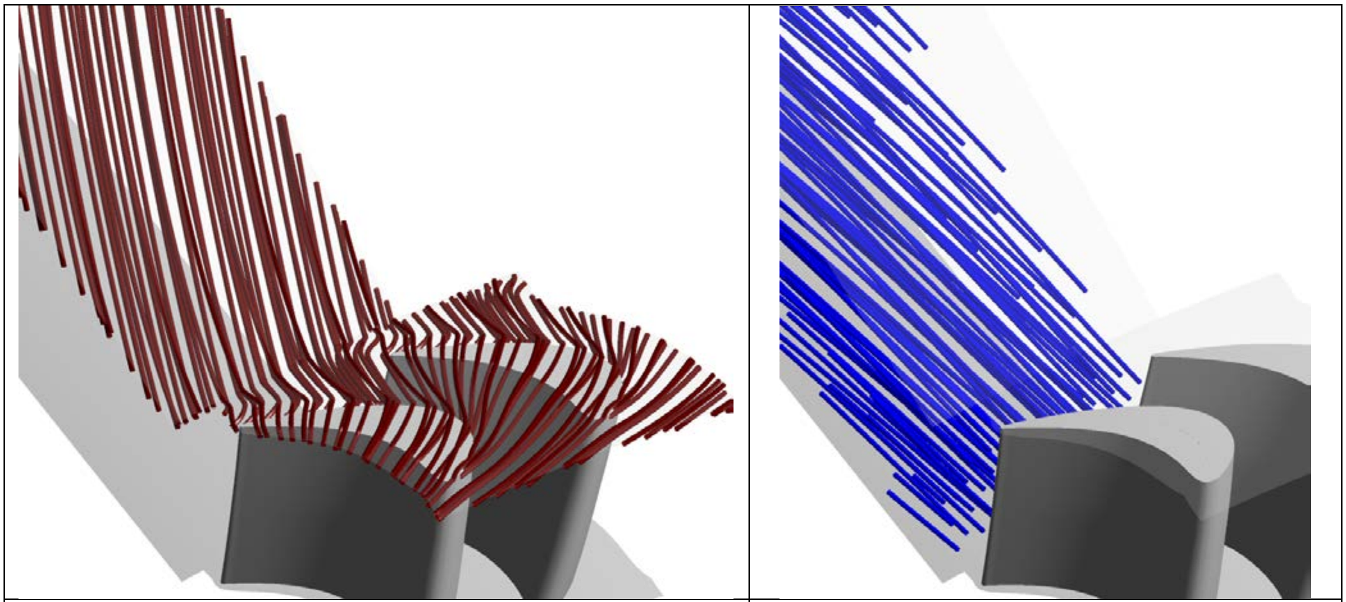

Tip clearance flow in co-swirl (α_3 = 13.3^o) | **Core passage flow as counter-swirl (α_3 = -9.2^o)**

Figure 5.35: Velocity streamlines (abs. frame of ref.) of the tip clearance and core passage flows

Table 5.4 summarizes the static pressure recovery and total pressure loss coefficients at various averaged inlet flow swirls for the case of the diffuser with an opening angle of 18°. The swirl given by the over the tip leakage and main passage core flows are also distinguished.

Table 5.4: Swirl and pressure coefficients for the 18° diffuser summarized

	Average Rotor Exit Swirl (α_3)						
	-40.4°	**-20.5°**	**-4.2°**	**0.1°**	**4.4°**	**8.7°**	**12.9°**
Cp []	0.36	0.56	0.66	0.67	0.68	0.67	0.66
Cp_t [-]	0.044	0.025	0.018	0.017	0.017	0.017	0.018
OTL Swirl [°]	-13.9	3.2	13.3	15.8	18.2	20.5	22.7
Core flow Swirl [°]	-42.3	-24.6	-9.2	-4.9	-0.6	3.9	8.3

One can point out from this table that the diffuser recovers most pressure (optimized) when the over the tip leakage flow is in co-swirl and the main passage core flow is slightly in counter-swirl. These results agree with the observations presented in section 2.6.2.

5.5 Unsteady Stator/Rotor Analysis

Since the turbine has 36 stator and 54 rotor blades, to reproduce an unsteady computation one would have to consider calculating at least 2 stator and 3 rotor blades and then apply blade to blade rotational periodic boundaries to complete the entire machine, as shown in Figure 5.36 and Figure 4.7.

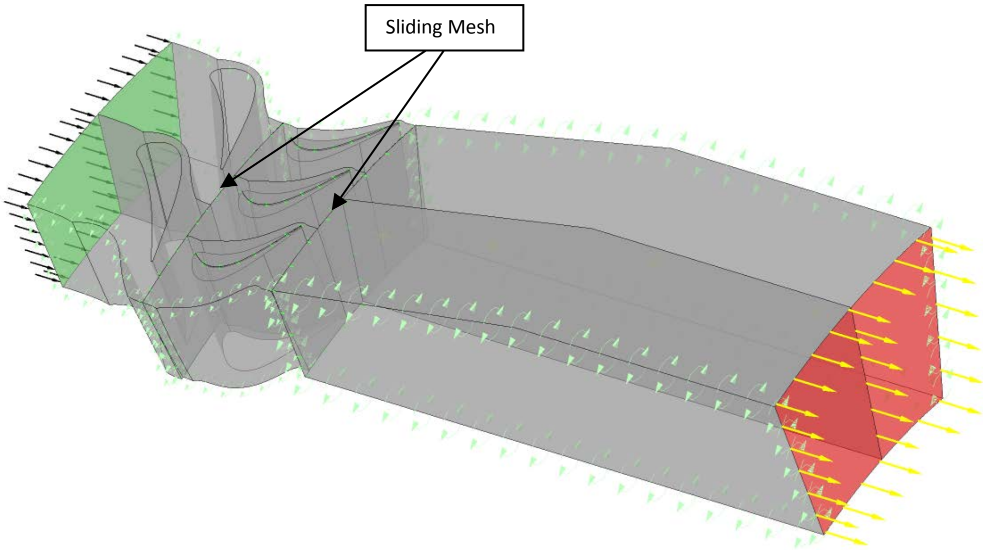

Figure 5.36: 3D model of the turbine stage with the diffuser used in the unsteady study

In this numerical case, the fluxes coming out of each row are no longer averaged circumferentially. Instead they are passed back and forth from row to row as the rotor mesh slides circumferentially with respect to the stator and diffuser to a new position. This method of computation best fits the operation of the real machine, but has the disadvantage of being very time consuming and require lots of computing power and disk storage. Because of these drawbacks, turbomachinery unsteady computations are mainly restricted to an academic research environment, being the mixing plane model most popular in the industry.

In Figure 5.37 one can see how the entropy generated in the stator row is chopped by the rotor. The entropy created by the stators is convected downstream the rotor passages as it merges with the entropy generated by the rotor itself. At this time it is interesting to contrast this figure with Figure 5.6 on the right, where the mixing plane algorithm was used.

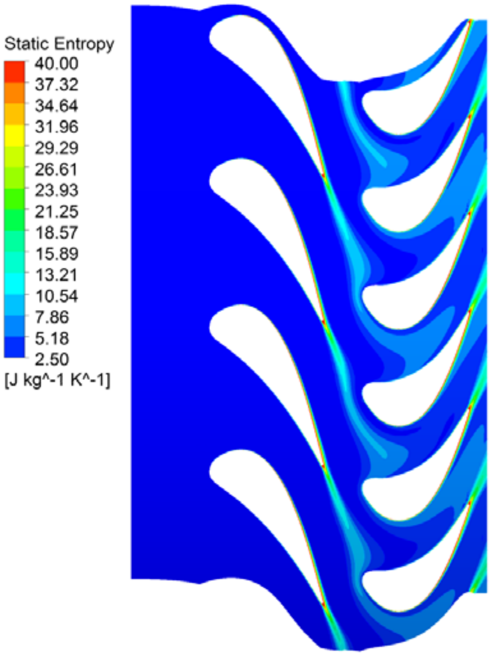

Figure 5.37: Contours of entropy generation through the turbine stage at a mid-span plane

5.5.1 Methodology used in turbomachinery unsteady computations

In order to start unsteady computations in turbomachinery, the first step is to obtain a converged steady solution using the "frozen rotor" inter-stage algorithm as seen in Figure 5.38.

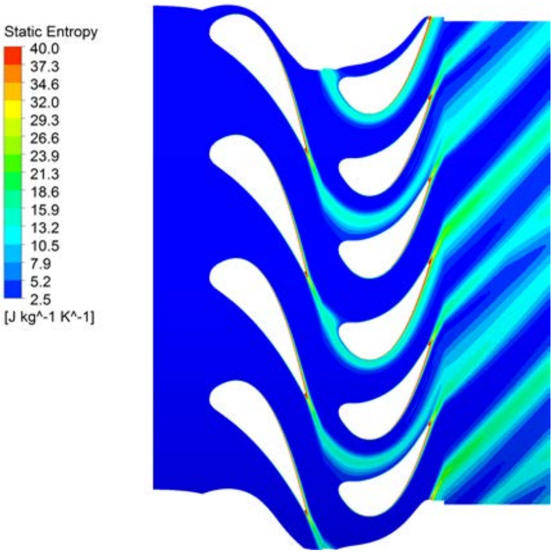

Figure 5.38: Computed entropy contours at turbine mid-span using frozen rotor inter-stage algorithm

The result from the frozen rotor is used as initial conditions for the unsteady computations. But first it is necessary to calculate the blade passing frequency of the rotor with respect to the stator and diffuser. In this case the passing frequency of 3 rotors with respect to 2 stators to make for a total rotational angle of 20°.

Since the rotational speed is 2,700 rpm, that is 282.74 rad.s^{-1}, and the model has a circumference of 20° (0.349 radians), then the period is given by:

$$T = \frac{\theta}{\omega} \tag{5.15}$$

Where θ is the circumference of the modeled domain and ω the rotational speed of the rotor.

Then the calculated period is: $T = \frac{0.349\, rad}{282.74\, rad \cdot s^{-1}} \approx 0.81\, s^{-1}$

The time step needs then to be determined. With explicit CFD solvers the Courant number (CN) is a criterion for numerical stability. Typical values of CN are around 1.0, from where the time step Δt is retrieved. Since CFX uses an implicit solver the numerical scheme is stable (in theory) no matter the value of the CN. Nonetheless, the CN is still a good indication of time resolve accuracy. The Courant number is given as:

$$CN = \frac{u \cdot \Delta t}{\Delta x} \tag{5.16}$$

With	u	flow velocity in the grid cell
	Δt	time step
	Δx	distance between grid cell nodes

In the numerical analysis of unsteady turbomachines the best indication to judge whether or not a solution can be accepted as converged, on top of the numerical residuals of the CFD solver, is to check some thermodynamic properties as the solution is updated. For that, several "numerical pressure probes" were inserted at distinct locations in the domain. The work coefficients, efficiencies, degree of reaction, etc., are also evaluated. Due to the blade passing frequency these values fluctuate according to the relative position of the rotor. Therefore, one has to look for that these calculated quantities display the same periodic change at each pass of the rotor blade.

Starting with 10 time steps per rotor pass then doubling the amount (20, 50, 100, 200, 500), the flow field solution in the unsteady turbine-diffuser domain is refined. Finally choosing 1,000 steps per pass, that is a time step of $\Delta t = 1.235 \times 10^{-6}$ s, and allowing the rotor to make several passes (5 times), the obtained root mean squared (RMS) Courant number is of 1.66, with a maximum of 44.55.

5.5.2 Diffuser with an unshrouded Rotor

In this case study only a turbine-diffuser model with a diffuser of 18° opening angle is considered.

In Figure 5.39 the axial velocity at the exit of the rotor row (3 rotors) is shown in function of the relative rotor pitch position.

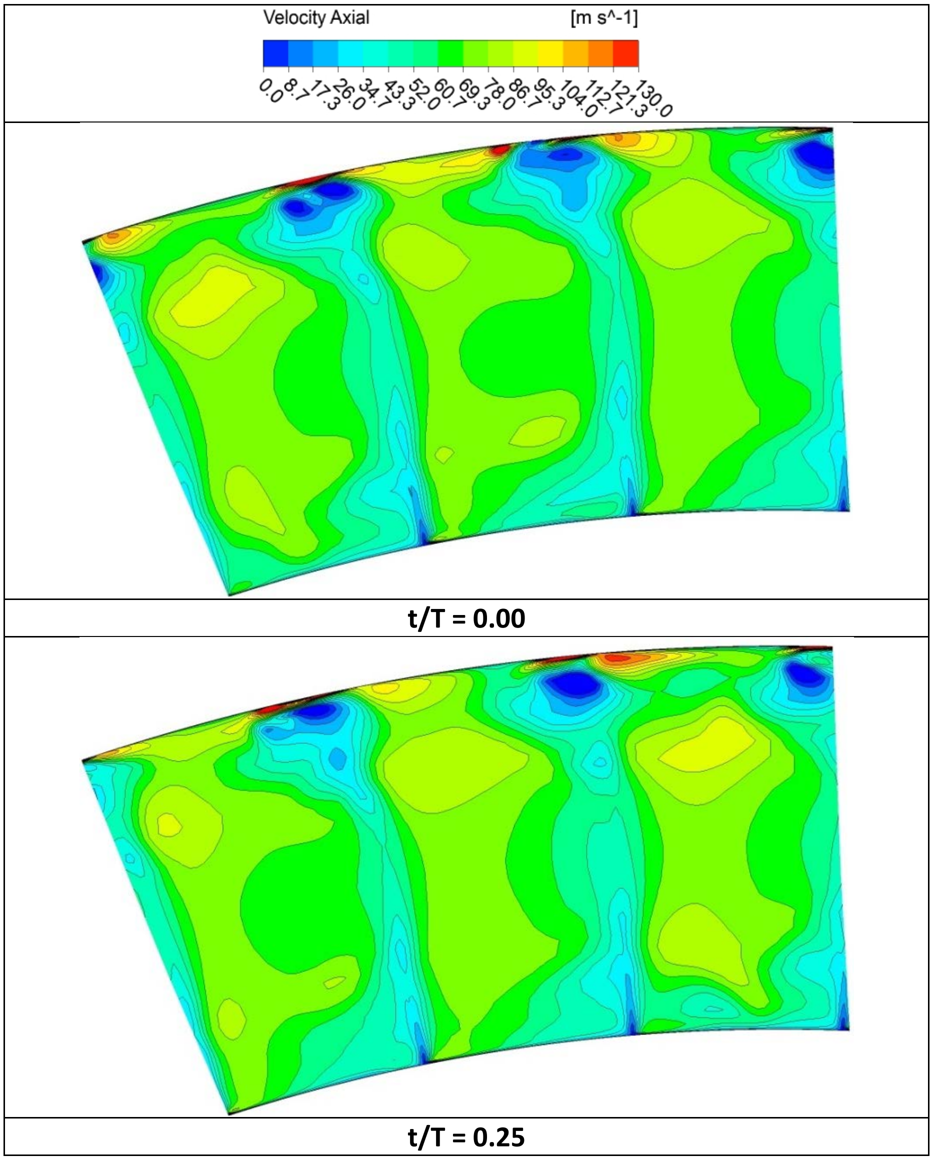

t/T = 0.00

t/T = 0.25

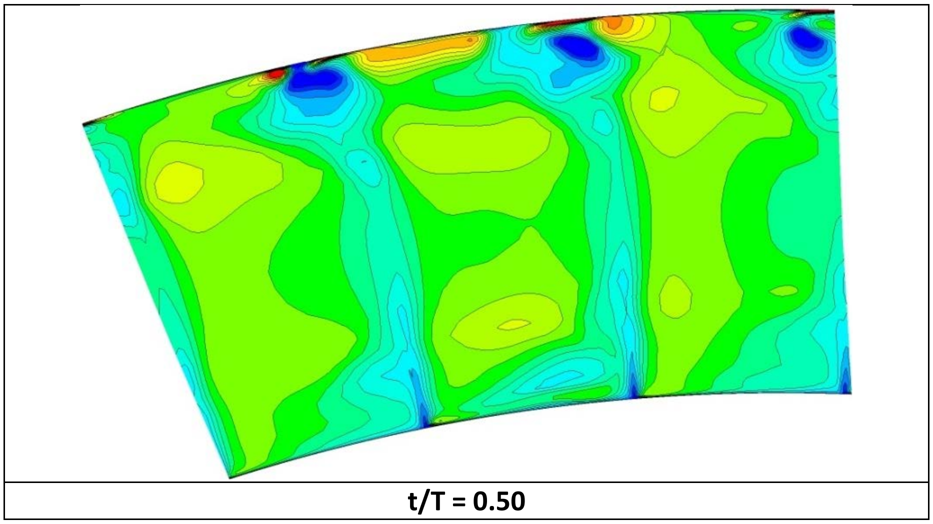

t/T = 0.50

Figure 5.39: Axial velocity contours at the exit of the rotor in function of the rotor pitch location

The first thing that one can perceive from the preceding figure is that the flow field is different at the exit of each of the three rotor passages, and that at all positions in time considered. Secondly, while the over the tip leakage flow is always there, its strength pulsates with the passing of the rotor. Although this OTL flow strength appears with the same frequency over each of the three rotor blades considered here, a phase shift is noticed from blade to blade.

Figure 5.40 illustrates the contours of axial velocity in the diffuser and how it varies with time. The OTL flow from the clearance of the rotors is perceived by the diffuser as wall jets that feed into the diffuser upper wall boundary layer. The axial velocity speed of these jets varies with time. Mixing of the flow field takes place more rapidly than when the steady state case was considered. As a consequence the extent of the wall jet is reduced and by the time the flow reaches 2/3 of the distance to the diffuser exit, the boundary layer grows rapidly.

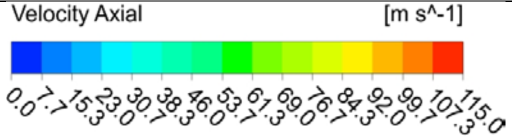

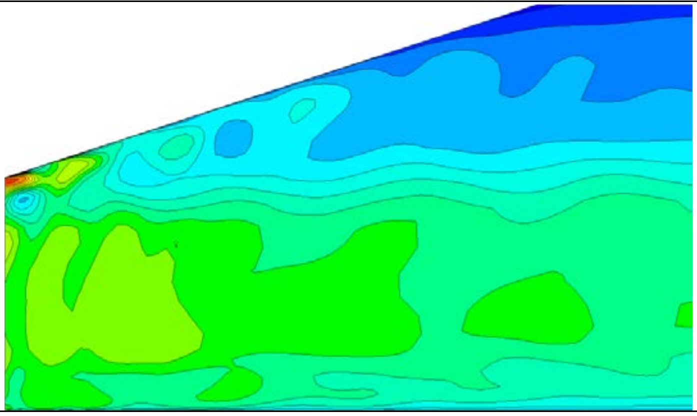

t/T = 0.00

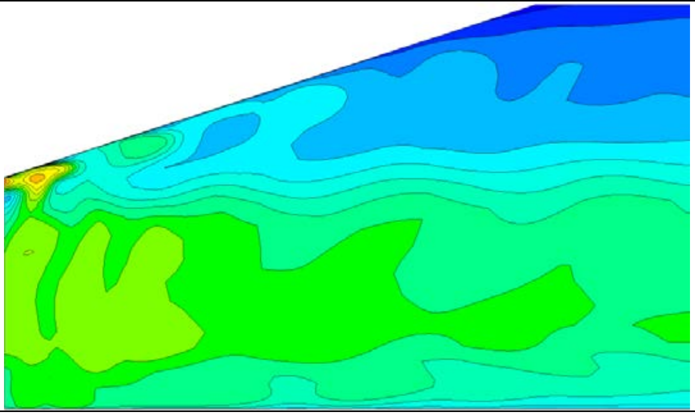

t/T = 0.25

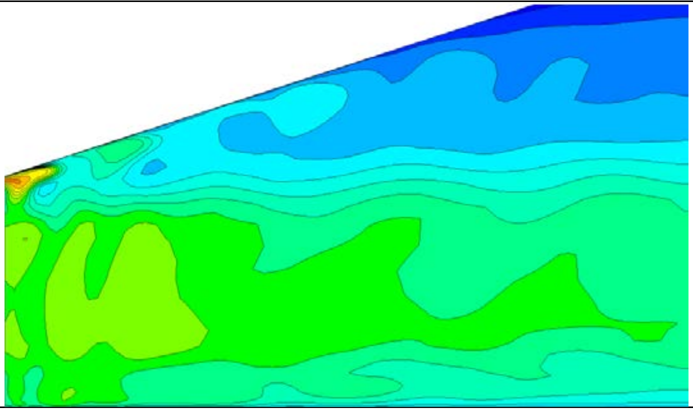

t/T = 0.50

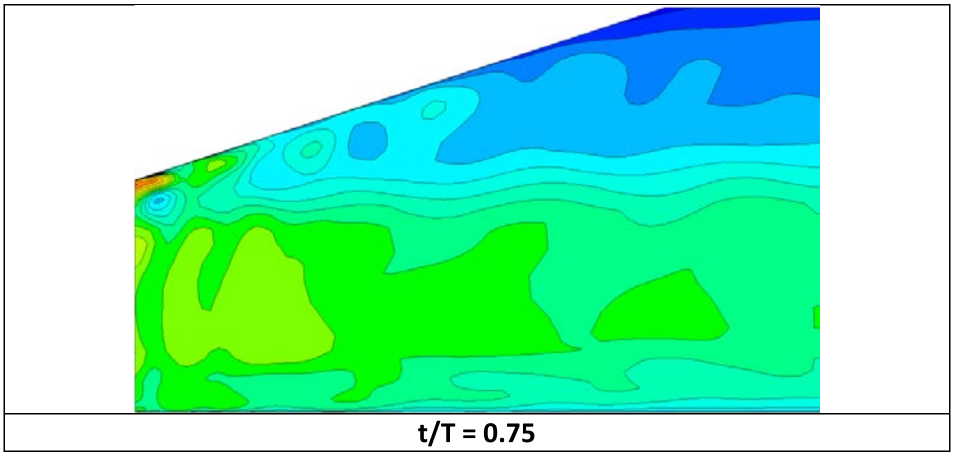

t/T = 0.75

Figure 5.40: Computed contours of axial velocity in the diffuser mid-plane in function of the rotor position

Comparing the axial velocity flow contours from the previous figure with those of the steady state solution of Figure 5.26, for a diffuser opening angle of 18°, one can see that the wall jet axial velocity reaches speeds of up to 115 m/s, whereas in the steady state case the axial speed of the jet was averaged down to 80 m/s. This represents a deviation of 44%. Plus in the unsteady computation case, regions of flow separation at the upper corner wall of the diffuser are observed, as seen from Figure 5.41. This phenomenon was not detected in the steady state case. Therefore the penetration of the wall jet into the diffuser boundary layer is weaker here.

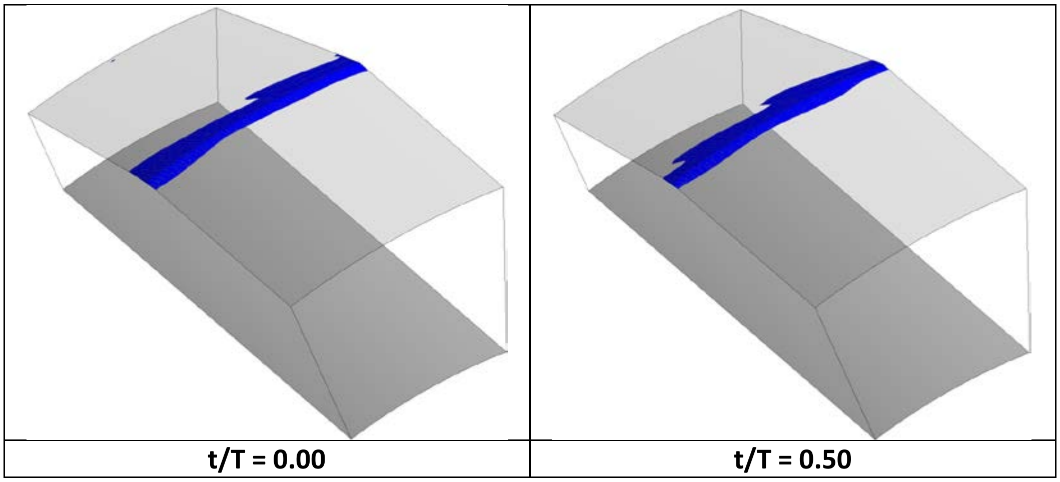

t/T = 0.00 **t/T = 0.50**

Figure 5.41: Computed isosurfaces or reversed flow in the diffuser at two rotor pitch positions

In Figure 5.42 contours of flow swirl angle in the diffuser mid-plane with time are presented. Here one can observe that the OTL flow emerges as a pulsating co-swirl wall jet, contrary as indicated back in the steady state calculations (Figure 5.27) where the jet was counter-swirling (averaged).

Also, as shown with the axial velocity, the swirl strength of the wall jet diffuses faster with the distance than in its steady state counterpart. The jet swirl mixes up quicker with the core flow swirl so that its extent throughout the diffuser is reduced, as compared with the steady state case.

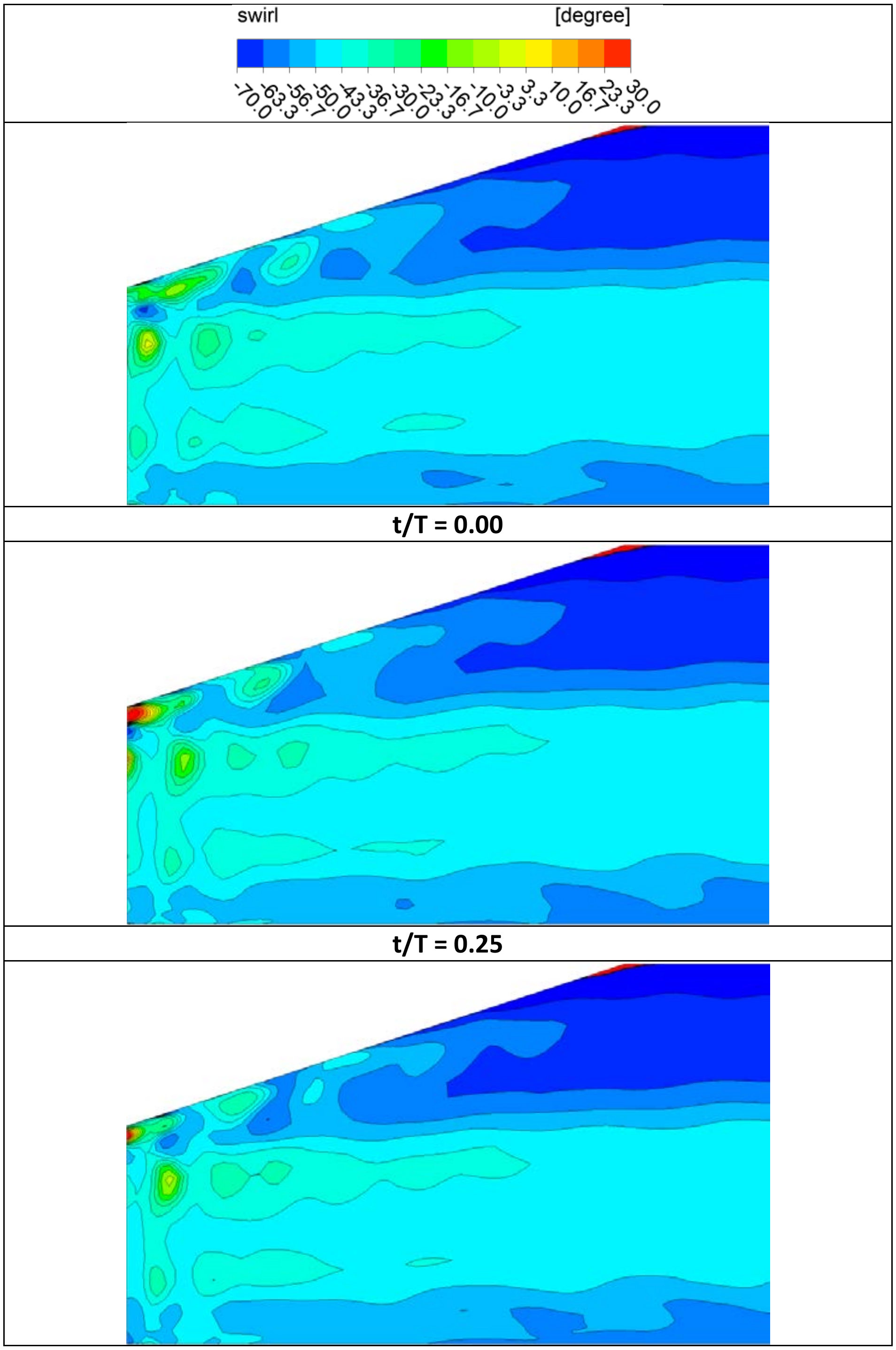

t/T = 0.00

t/T = 0.25

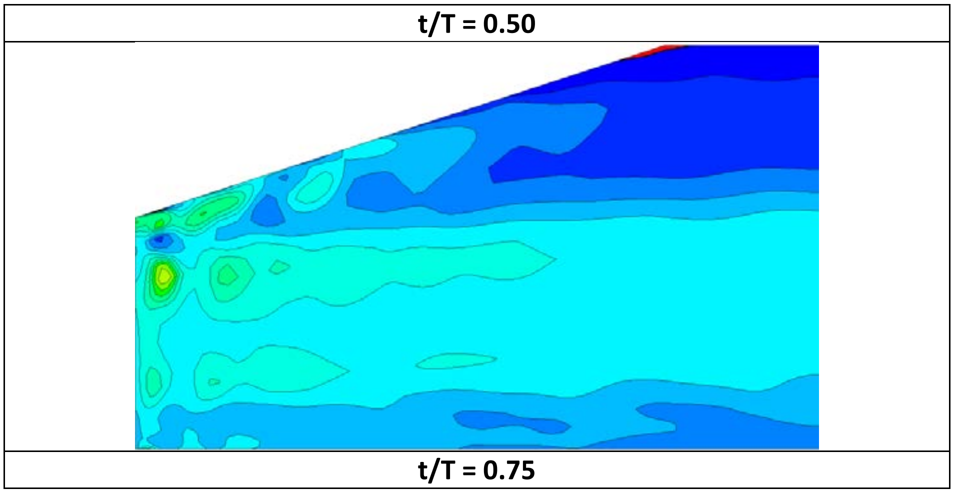

Figure 5.42: Computed contours of swirl in the diffuser mid-plane in function of the rotor position

Finally, the performance of the diffuser varies also in time as indicated from the static pressure recovery and total pressure loss coefficients, of Figure 5.43 and Figure 5.44 respectively. These were taken at intervals of 50 time steps.

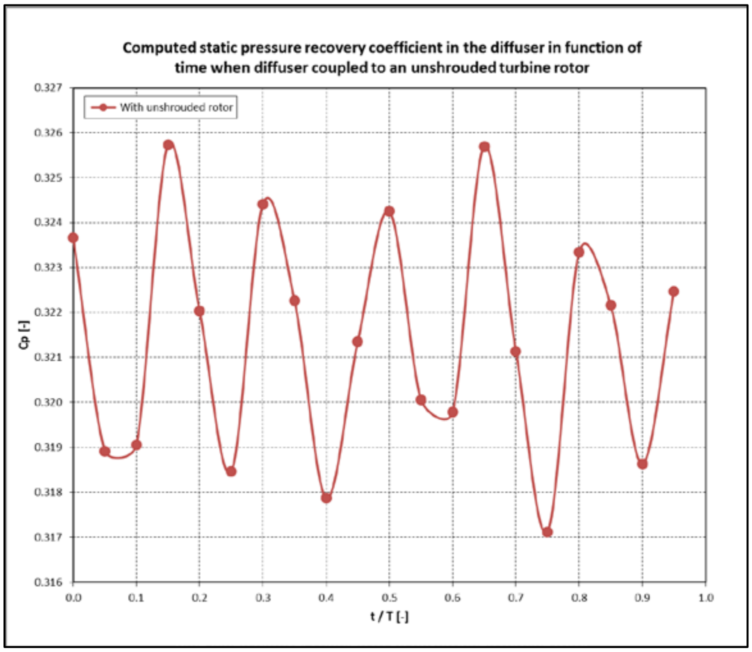

Figure 5.43: Computed Cp in diffuser in function of the rotor position

From Figure 5.43 it is seen that the maximum value of the static pressure coefficient is Cp_{max} = 0.326 and the minimum Cp_{min} = 0.317. This represents a deviation of 2.6 % from its minimum to its maximum. With an averaged value of Cp_{avg} = 0.321, this figure is 11.0 % less than the Cp obtained during the steady state computations since it was of Cp_{steady} = 0.358. Similarly for the total pressure loss coefficient of Figure 5.44, the maximum is at $Cp_{t,max}$ = 0.114 and the minimum at $Cp_{t,min}$ = 0.098, given a deviation of 14.0 % (minimum to maximum) and an average of $Cp_{t,avg}$ = 0.106.

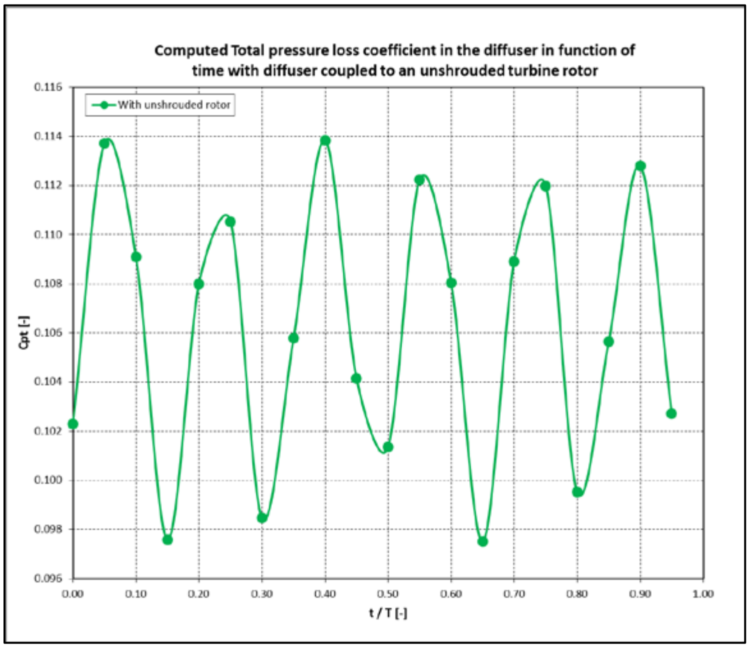

Figure 5.44: Computed Cp_t in diffuser in function of the rotor position

Since the total pressure loss coefficient of the diffuser in the steady state case was of $Cp_{t,steady}$ = 0.044, with the unsteady computations 41.5 % higher losses are obtained. Of course in the steady state calculation no reverse flow was observed.

6 CONCLUSIONS AND RECOMMENDATIONS

6.1 Conclusions

By simulating the flow inside an actual industrial gas turbine stage and then coupling it to the exhaust diffuser a more realistic performance simulation environment for the diffuser is achieved. Studying the shrouded and un-shrouded turbine rotors, the effect of tip clearance on the exhaust diffuser performance is isolated. Indeed the over the tip clearance flow emerges as a wall jet at the upper wall of the diffuser, energizing the flow boundary layer and hence postponing diffuser stall. As demonstrated, the maximum diffuser opening angle possible without the presence of the wall jet, before the diffuser stalls, was 12°. With the presence of the wall jet, diffuser opening angles above 18°

are possible. Consequently the wall jet helps the boundary layer flow in the diffuser to remain attached longer and thus recovers higher static pressure.

By altering the inlet flow swirl to the diffuser with a shrouded and an unshrouded rotor, the effect of co- and counter-swirl is studied. In the first case, it was found that the diffuser recovers more static pressure when the inlet flow is swirl free. As expected, the static pressure recovery coefficient curve showed a perfect symmetry around a swirl of 0°. Therefore the performance of the diffuser is independent of the swirl direction. In the other case studied more pressure was recovered by the diffuser when the wall jet was in co-swirl and the core flow at a slightly counter-swirl direction. Indeed this gives rise to a shear layer with streamwise vorticity that forms between the wall jet and the core flow. This vortex sheet enhances mixing near the wall. This effect was more noticeable as the opening angle of the diffuser increased. Hence the swirl of the wall jet and the core flow affects the performance of the diffuser.

Finally, a full unsteady investigation was conducted using a turbine-diffuser configuration with an unshrouded rotor and a diffuser with an opening angle of 18°. In this case the wall jet axial velocity and swirl intensities pulsate with time, i.e., dominated at the rotor blade passing frequency. The spectral frequency of this pulsation seems to be dependent on the number of rotor and stator blades and on the rotational speed of the rotor. It was found that the wall jet does not penetrate the diffuser boundary layer as much as in the steady state case and flow separation occurs at the end wall corner of the diffuser. The swirl shows a similar trend. Consequently the unsteady-performance of the diffuser is 11.0 % lower than the one obtained in the steady state case and the total pressure loss is 41.5 % higher. Moreover the performance of the diffuser fluctuates in time. Having such high total pressure losses can be attributed to the partial stall of the diffuser, whereas the fluctuation of the pressure can be due to the flow separation as well as the unsteady potential field that is driven at the diffuser inlet at the blade passing frequency.

Looking at these results, it is evident that the mixing plane algorithm might not be the ideal method to use in this type of study, i.e., to isolate a single phenomenon, since the circumferentially non-uniform flow at the entrance of the diffuser has a strong effect on its performance. The other alternative to full unsteady computations is to use the “frozen rotor” method. This method was utilized by Kluss et al. [34] who justified its use as “*a first-order approach to the unsteady flow*”. However the frozen rotor is a method that does not represent the full unsteady behavior of a rotating machine and should be discarded, especially when the study of non-uniform flows, in particular jets, is considered.

6.2 Recommendations for future work

For the future work, it would be helpful to use a low pressure turbine stage in front of the exhaust diffuser, where the outlet swirl is close to 0°. This arrangement is more representative of the actual operation of a stationary gas turbine. Moreover, low pressure turbine stages have thinner blade profiles, which would affect the tip leakage flow features. By having a design exit swirl close to 0°, it is easier to tune the rotor exit flow in the core to counter-swirl or to co-swirl by changing the rotational speed of the rotor, without the risk of stalling the turbine stage (off-design operation).

Furthermore, regardless of the nature of the turbine stage utilized, the use of a flared casing, to match the slope angle of the diffuser would be very interesting to investigate. Here, with a turbine with straight walls, the flow at the tip clearance region has to undergo an initial turn to enter the diffuser. This might not be an optimal geometry for the wall jet to energize the outer diffuser wall boundary layer. In addition, a study of the effect of the axial spacing between the turbine exit and the diffuser inlet on the static pressure recovery of the diffuser might be of interest. As well as the effect of adding diffuser struts.

Because of the discrepancies obtained when using the mixing plane algorithm, future diffuser design processes should be routed towards the use of unsteady computational models in order to improve the understanding of the physical phenomena between the interaction of the turbine stage and the diffuser.

As an alternative to use unsteady computations with the turbine stage-diffuser configuration, one could use the averaged in time flow conditions obtained between the exit rotor row and the diffuser and use them as inlet conditions to compute a stand-alone diffuser. This would certainly speed up the overall computational time. A drawback to this method is that these boundary conditions can only be obtained after a previous unsteady computation. And since these “inter-stage” conditions are turbine-diffuser specific, they hardly would be applicable to other turbine-diffuser configurations such as in the study of the variation of the diffuser opening angle. However, this approach may be successfully used in the investigation of the axial spacing between the rotor exit and the diffuser.

7 REFERENCES

[1] *GT11N2 Gas Turbine*. Commercial flyer, 2009. Alstom (Switzerland) Ltd., Brown-Boveri Strasse 7, CH-5401 Baden, Switzerland.

[2] Hawthorne W.R., “Rotational Flow through Cascades”, Journal of Mechanics and Applied Mathematics, 3, 1955.

[3] Hawthorne W.R., “Secondary Circulation in Fluid Flow”, Proceedings of the Royal Society of London. Series A, Mathematical and Physical Sciences, 206 (1086): 374-387, 1951.

[4] Langston L.S, Nice M.L., and Hooper R.M., “3-Dimensional Flow within a Turbine Cascade Passage”, Journal of Engineering for Power – Transactions of the ASME, 99(1): 21-28, 1977.

[5] Vogt H.F., Zippel M. “Sekundaerstroemungen in Turbinengittern mit geraden und gekruemmten Schaufeln; Visualisierung im ebenen Wasserkanal”, Forschung im Ingenieurwesen - Engineering Research, 62 (9), 247-253, 2001.

[6] Lakshminarayana *B., Fluid Dynamics and Heat Transfer of Turbomachinery*, J.Wiley & Sons, 1996.

[7] Booth T.C, “Rotor Tip Leakage Part I – Basic Methodology”, J. of Engineering for Power, Vol. 104, pp. 154-161, 1983.

[8] Harvey N.W., “Turbine Blade Tip Design and Tip Clearance Treatment”, Von Karman Institute for Fluid Dynamics, Lecture Series 2004-02.

[9] Denton J.D., “Loss Mechanisms in Turbomachines”, ASME J. of Turbomachinery-Transactions of the ASME, Vol. 115, pp.621-656, 1993.

[10] Moore J., Tilton J.S., “Tip Leakage Flow in a Linear Turbine Cascade”, ASME J. of Turbomachinery, Vol. 100, pp. 18-26, 1988.

[11] Bindon J.P., “The Measurement and Formation of Tip Leakage Loss”, ASME J. Turbomachinery, Vol. 111, pp. 257-263, 1987.

[12] Yaras M.I., Sjolander S.A., “Effects of Simulated Rotation on Tip Leakage in a Planar Cascade of Turbine Blades. Part I: Tip Gap Flow”, ASME J. of Turbomachinery, Vol. 114, pp. 660-667, 1992.

[13] Graham J.A.H., “Investigation of a Tip Clearance Cascade in a Water Analogy Rig”, ASME J. of Engineering for Gas Turbines and Power, Vol. 108, pp. 38-46, 1986.

[14] Bindon J.P., Morphis G. “The Development of Axial Turbine Leakage Loss for Two Profiled Tip Geometries Using Linear Cascade Data”, ASME Paper 90-GT-152, 1990.

[15] Porreca L., “Aerothermal Optimization of Partially Shrouded Axial Turbines”, PhD Diss. ETH Zurich, 2007.

[16] Behr T., “Control of Rotor Tip Leakage and Secondary Flow by Casing Air Injection in Unshrouded Axial Turbines”, PhD Diss. ETH Zurich, 2007.

[17] Hodson H.P., “Bladerow interference effects in axial turbomachinery stages”, VKI Lecture Series, Von Karman Institute for Fluid Dynamics, Belgium, 1998

[18] Dean C.D., “On the Necessity of Unsteady Flow in Fluid Machines”, Journal of Basic Engineering – Transactions of the ASME, 81 (1): 24-28, 1959

[19] Parker R., Watson J.F., “Interaction Effects Between Blade Rows in Turbomachines”,

Proceedings of the Institution of Mechanical Engineers, 186 (21), 1972.

[20] Meyer R.N., "The Effect of Wakes on the Transient Pressure and Velocity Distribution in Turbomachines", ASME Journal of Basic Engineering, Vol 80, pp. 1544-1552, 1958.

[21] Kerrebrock J.L., Mikolajczak A.A., "Intra-Stator Transport of Rotor Wakes and Its Effect on Compressor Performance", J. Eng. Power 94(2), pp. 359-368, 1970.

[22] Binder A., Foster W., Mach K. and Rogge H., "Unsteady Flow Interaction Caused by Stator Secondary Vortices in a Turbine Rotor", Journal of Turbomachinery – Transaction of the ASME, 109 (2): pp. 251-257, 1987.

[23] Farokhi S., "Analysis of Rotor Tip Clearance Loss in Axial-Flow Turbines", ASME J. of Propulsion, Vol. 4, No. 5, 1988.

[24] *Turbomachinery Diffuser Design Technology*, D. Japikse, Concepts, ETI, Inc., 1984.

[25] *GT24/GT26 Gas Turbine*. Commercial flyer, 2008. Alstom (Switzerland) Ltd., Brown-Boveri Strasse 7, CH-5401 Baden, Switzerland

[26] Bammert K., Klaeukens H., Hartmann D., "Der Einfluss des radialen Schaufelspalts auf den Wirkungsgrad mehrstufige Turbinen", VDI-Zeitschrift, Vol. 110, No. 10, April 1968, pp. 390-395.

[27] Farokhi S., "Coupled Performance of Axial Exhaust Diffusers and Low-Pressure Turbine", Private Communication, October 2013.

[28] *ANSYS CFX-Solver Theory Guide*, ANSYS, Inc. Release 13.0, 2011.

[29] *ANSYS CFX-Solver Modeling Guide*, ANSYS, Inc. Release 13.0, 2011.

[30] Behr T., Kalfas A.I., Abhari R.S., "Unsteady Flow Physiscs and Performance of a One-and-1/2-Stage Unshrouded High Work Turbine", ASME J. of Turbomachinery - Transactions of the ASME, Vol. 129, pp. 348-359, 2007.

[31] *Fluid Mechanics*, P.K. Kundu, I.M. Cohen, Academic Press, Second Ed., 2002.

[32] Cumpsty N.A., Horlock J.H., "Averaging Non-Uniform Flow for a Purpose", ASME Turbo Expo, Proceedings of GT2005-68081, 2005.

[33] Denton J.D., "Axial Turbine Aerodynamic Design", Lecture notes from the Turbomachinery Course, Whittle Laboratory, Cambridge University Engineering Dept., 2008.

[34] Kluss D., Wiedermann A., Volgmann W., "Impact of Gas Turbine Outflow on Diffuser Performance – A Numerical Study", Power for Land, Sea, and Air, Proceedings of ASME Turbo Expo, GT2004-53043, 2004.